Magnetoresistance and Spin-Orbit interaction in Complex 2DEG Systems: A Study of Shubnikov-de Haas Oscillations

Hamed Gramizadeh

May 22, 2023

Thesis Committee:

Sigurdur Ingi Erlingsson, Supervisor
Professor, Reykjavik University, Iceland

J. Carlos Egues, Advisor
Professor, University of Sao Paulo, Sao Carlos, Brazil

Andrei Manolescu, Professor, Advisor
Professor, Reykjavik University, Iceland

Martin Veis, Professor, Examiner
Associate Professor, Charles University, Faculty of Mathematics and Physics, Czech Republic

Magnetoresistance and Spin-Orbit Interaction in Complex 2DEG Systems: A Study of Shubnikov-de Haas Oscillations

Short title: Magnetoresistance and Spin-Orbit Interactions in Complex 2DEG Systems

SVANSPRENT

To my beloved parents for their presence and support in my life. and to my dearest Masoumeh, for the continuous love and patience.

Contents

List of Figures

x

Magnetoresistance and Spin-Orbit interaction in Complex 2DEG Systems: A Study of Shubnikov-de Haas Oscillations

Hamed Gramizadeh

March 31, 2023

Abstract

Magnetoresistance oscillations, also known as Shubnikov-de Haas (SdH) oscillations, is a well-known phenomena that results from the quantization of electron orbits in the presence of a magnetic field. These oscillations have been extensively studied and are a valuable experimental tool for extracting electronic charge densities and spin-orbit interaction (SOI) couplings, such as Rashba and Dresselhaus couplings. Although 2DEGs with large Rashba, Dresselhaus, and g-factors are available, the current theoretical picture of explaining SdH behavior is not able to account for all those factors. Our findings show that by using a Poisson summation formula, we can analyze magneto-oscillations in 2DEGS systems with Rashba, Dresselhaus, and Zeeman couplings. The Poisson summation formula naturally separates the magnetooscillations into fast and slow components which facilitates the analysis of the spin-orbit contribution. In this Ph.D. thesis, we investigate magnetooscillations in complex 2DEGs using both analytical and numerical methods thus providing a unique and comprehensive approach. Using the analytical approach, we identified a new condition for the vanishing of spin-orbit-related beatings. With numerical method, we are abled to extract both SOI couplings from the SdH oscillations independently of their Zeeman strength and electrical charge density. Additionally, we found that the behavior of SdH oscillations in such systems can be greatly influenced by the angle at which the in-plane magnetic field is tilted. This research contributes to the ongoing process of the development of novel spintronic devices.

Acknowledgments

I extend my sincerest gratitude to my supervisors whose invaluable guidance, encouragement, and support have shaped my academic journey and led to the completion of this doctoral work. Their expertise and insights have been essential in helping me navigate the challenges and obstacles of this research project. I am deeply grateful for the opportunities they have provided me and the confidence they have instilled in me. I would also like to acknowledge Reykjavik University that has supported my studies, providing the resources and infrastructure necessary to conduct this research. I am grateful for their unwavering support and belief in my abilities. Finally, I would like to express my appreciation to the subjects of this research, who have generously given their time and expertise, providing the foundation of this work. Their contributions are deeply valued and greatly appreciated. This work is dedicated to all who have supported me and inspired me to pursue this path, and I hope that it will make a meaningful contribution to the field. This dissertation was supported by

Reykjavik University Ph.D.

Chapter 1

Introduction

1.1 Background

A two-dimensional electron gas (2DEG) is a quantum model of electrons that are confined to move in two dimensions, typically at the interface between two semi-conducting materials. In this state, the electrons are free to move only in the plane parallel to the interface, while their motion perpendicular to the interface is confined by the potential barrier formed by the surrounding materials. 2DEG exhibits a number of unique and interesting electronic properties, such as high mobility and magnetoresistance oscillations [1]. These properties have led to the development of a wide range of electronic and photonic devices, including field-effect transistors, high-electron-mobility transistors [2]. The properties of 2DEG are highly dependent on the materials used to create the interface, as well as the applied electric and magnetic fields [3], [4]. Understanding the behavior of 2DEG is therefore of great interest to researchers in the fields of condensed matter physics, material science, and electronics. A two-dimensional electron gas that forms at the interface between zinc-blende semiconductors or insulators such as InAs/AlGaAs/GaAs heterojunction to produce the confinement in z direction [5]–[7]. The most commonly encountered 2DEG is the layer of electrons found in zinc-blende semiconductor field-effect transistors. It is an important building block in modern electronics, and it has a wide range of applications including field effect transistors, sensors, and quantum computing devices [8], [9]. The 2DEG can also be created by sandwiching a thin layer of semiconductor material between two insulating layers, known as a heterostructure. When an external voltage is applied to the heterostructure, it creates an electric field that can attract the electrons from the semiconductor material toward the insulating layer. The electrons are confined to move in the plane of the semiconductor layer due to the presence of the insulating layers, creating a 2DEG [10]. One of the key properties of the 2DEG system is its energy spectrum, which describes the al-

lowed energies that the electrons can possess. The presence of external fields such as a magnetic field or a gate voltage can alter the energy spectrum which is one of the key properties investigated in this thesis. The 2DEG has a number of interesting physical phenomena that arise due to its confined geometry and the presence of external electric or magnetic fields [11] such as the Shubnikov-de Haas effect that is a phenomenon where the resistance oscillates as a function of magnetic field. The origin of these oscillations is the quantized energy levels of the 2DEG. Other phenomena such as electron interference, where the wave-like nature of electrons that can lead to interference effects, which can be observed in 2DEG systems [12]. The 2DEG system has a wide range of applications in modern electronics. The exhibition of the physical phenomena due to its confined geometry and the presence of external fields, and is an active area of research in the fields of condensed matter physics and material science, solid state physics and etc.

1.2 Spintronics

Spintronics, short for spin-based electronics, is an established field of research that aims to exploit the spin of electrons as a fundamental property for information processing and storage. In traditional electronics, information is processed and stored using the charge of electrons. However, in spintronics, the spin of electrons is used as an additional degree of freedom to carry and manipulate information [13]. Spintronics is an active and interdisciplinary field of research that spans materials science, condensed matter physics, and electrical engineering. In spintronics, researchers investigate the properties of materials that exhibit spin-dependent transport, spin-orbit coupling, and other spin-related phenomena. They develop and optimize devices that use these materials to perform tasks such as magnetic sensing, data storage, and information processing [14], [15]. One of the key advantages of spintronics over traditional electronics is its potential for reduced power consumption and increased processing speed. Spintronics devices can operate at lower voltages and currents than their electronic counterparts, making them ideal for use in energy-efficient applications. Furthermore, the use of spin allows for faster switching speeds and higher storage densities, enabling the development of new technologies such as magnetic random access memory. Spintronics is an exciting and rapidly developing field with the potential to revolutionize electronics and information technology. Ongoing research is expected to lead to the development of new materials, devices, and applications, with the ultimate goal of creating a new generation of spin-based technologies that are faster, more energy-efficient, and more versatile than traditional electronic devices[14]. Some spintronics devices use spin-orbit couplings as a key ingredient which we investigate in this thesis.

1.3   Model Hamiltonian

The model Hamiltonian for 2DEG can be constructed by:

$$H = \frac{1}{2m}\left[(p_x + \frac{eBy}{2})^2 + (p_y - \frac{eBx}{2})^2\right], \qquad (1.1)$$

where m is the effective mass, $p_{x,y}$ are the momentum operators, e is the electric charge and B is the magnetic field. The vector potential A gives the magnetic field B through the equation $B = \triangledown \times A$. Here we use the symmetric gauge $A_x = \frac{-eBy}{2}$ and $A_y = +\frac{eBx}{2}$. Introducing the operator $\pi_{x,y} = p_{x,y} \pm eA_{x,y}$ we can rewrite the Hamiltonian:

$$H = \frac{1}{2m}(\pi_x + i\pi_y)(\pi_x - i\pi_y) + i[\pi_x, \pi_y], \qquad (1.2)$$

from this point, we defined ladder operators a and $a^\dagger$ as fulfill the $[a, a^\dagger] = 1$.

$$a^\dagger = \frac{1}{\sqrt{2e\hbar B}}(\pi_x + i\pi_y) \qquad (1.3)$$

$$a = \frac{1}{\sqrt{2e\hbar B}}(\pi_x - i\pi_y) \qquad (1.4)$$

which leads us to a famous relation of the Hamiltonian expression that describes the so-called Landau levels:

$$H = \hbar\omega_c(a^\dagger a + \frac{1}{2}) \qquad (1.5)$$

where $\omega_c = \frac{eB}{m}$ is the cyclotron frequency of the Landau levels. The symmetrical gauge is preferred over the Landau gauge for this specific purpose due to its convenience for mathematical calculations [13].

1.3.1   Zeeman coupling

Magnetic moments associated with electron spin are either parallel or antiparallel to the magnetic field. The orientation of this momentum changes the energy of the state by $\pm\frac{1}{2}g\mu_B|B|$, where $\mu_B = \frac{eh}{2m_0}$ is the Bohr Magneton. This energy shift is known as the Zeeman splitting. The one-half factor comes from the spin which carries angular momentum $\frac{\hbar}{2}$. Thus, the Zeeman coupling describes the splitting of the energy levels of a system in the presence of an external magnetic field. The Zeeman effect is named

after Dutch physicist Pieter Zeeman [16], who first observed the effect in the emission spectra of excited particles. It can be described by adding $\frac{1}{2}g\mu_B|B|\sigma_z$ where σ_z is the Pauli matrice in the Hamiltonian. The impact of the Zeeman effect on the energy spectrum of a 2DEG system depends on the strength and orientation of the magnetic field, and it has applications in the field of spintronics and quantum information and could affect the transport properties of the 2DEG system. The form of Zeeman added to 2DEG comes as:

$$H = \hbar\omega_c(a^\dagger a + \frac{1}{2}) + \frac{1}{2}g\mu_B B\sigma_z \tag{1.6}$$

The $g-$factor is approximately 2 for a free electron and in the case of (InAs) is $g = -12$ [17], [18]. Even with this enhancement InAs quantum wells typically have major $g-$factors compared to other common materials such as GaAs.

1.4 Spin-orbit interaction (SOI)

The spin-orbit interaction is a fundamental phenomenon in quantum mechanics that arises due to the interaction between the electron's spin and its motion around the atomic nucleus. This interaction leads to energy level splitting, which is responsible for several important effects in solid-state physics such as Rashba and Dresselhaus SOI. We shall deal with the magnetic field first

$$\vec{B} = -\vec{v} \times \vec{\nabla}V. \tag{1.7}$$

Which describes the magnetic field when an electron is moving with velocity v in an electric field $\vec{\nabla}V$ where V is a potential. This leads to the Hamiltonian for the spin-orbit (SO) interaction:

$$H_{so} = \frac{e\hbar}{4M^2c^2}\vec{\sigma}.(\vec{p} \times \nabla V), \tag{1.8}$$

where c is the speed of light and $\vec{p}$ is the momentum.

1.4.1 Pure Rashba effect (SIA)

The Rashba effect refers to the splitting of the energy spectrum of a two-dimensional electron gas (2DEG) system in the presence of an external electric field. The Rashba effect is named after its discoverer, Soviet physicist E.I. Rashba, who first proposed the effect in a theoretical paper in 1960 [19]., which results in a spin splitting of the electron states due to the lack of inversion symmetry in some heterostructure that is known as structural inversion asymmetry (SIA). And has a substantial impact on the electronic band structure. When an external electric field is applied perpendicular

to the 2DEG plane, the spin-orbit coupling causes the energy levels of the 2DEG to split into two branches with different energies [20], [21]. The Rashba effect is important because it allows for the manipulation of the electron spin in the 2DEG system using external electric fields, which has applications in the field of spintronics [22]. The Rashba effect can have significant results on the transport properties of 2DEG systems such as its electrical conductivity and magnetoresistance[23]. The Hamiltonian for the Rashba SOI is defined as

$$H_R = \frac{\alpha}{\hbar}(\sigma_x \pi_y - \sigma_y \pi_x), \tag{1.9}$$

where α is the Rashba coupling constant and π_i, σ_i are the momentum operator and Pauli's matrices, respectively, in $i = x, y$ direction. The Hamiltonian describes a spin dependent coupling proportional to the momentum of the electrons, and it leads to a spin splitting of the energy bands. The aim is to investigate the Rashba Hamiltonian with Zeeman interaction in the total Hamiltonian, which can be written for nonzero magnetic field as:

$$H_R = a^\dagger a + \frac{1}{2} + \frac{\widetilde{\Delta}}{2}\sigma_z + \frac{\alpha}{\sqrt{2\hbar\omega_c}\ell_c}(a^\dagger\sigma_- + a\sigma_+) \tag{1.10}$$

Here we introduced the convention of scaling of all energies in terms of $\hbar\omega_c$. Here we will introduce the N_+ operator:

$$N^+ = a^\dagger a + \frac{\sigma_z}{2}. \tag{1.11}$$

Since H_R commutes with N^+:

$$[H_R, N^+] = [a^\dagger\sigma_- + a\sigma_+, a^\dagger a + \frac{\sigma_z}{2}] = 0, \tag{1.12}$$

where $\sigma_+ = \sigma_x + i\sigma_y$ and $\sigma_- = \sigma_x - i\sigma_y$ are defined as creation and annihilation Pauli operators, H_R and N^+ share a set of common eigenvectors together which can be used to diagonalize both operators simultaneously. This property is often exploited in quantum mechanics to simplify calculations and to identify conserved quantities[24]. So we can go through the eigenvalues and eigenvectors of N_+ in the basis $|n, s\rangle$ since they have common eigenstates and eventually get the spectrum of energies in this approach. These operators are going to share common eigenbasis for $n \in \mathbb{N}$ the N_+ becomes:

$$N_+|n, \uparrow\rangle = (n + \frac{1}{2})|n, \uparrow\rangle \tag{1.13}$$

$$N_+|n + 1, \downarrow\rangle = (n + \frac{1}{2})|n + 1, \downarrow\rangle. \tag{1.14}$$

Hence $|n,\uparrow\rangle$ and $|n+1,\downarrow\rangle$ are degenerate with respect to the operator N_+ as a conclusion, a linear combination of $|n,\uparrow\rangle$ and $|n+1,\downarrow\rangle$ is also an eigenstate of the Hamiltonian in eq. (1.10), this property abled us to rewrite all the Hamiltonian elements in the basis of the $|n,\uparrow\rangle$ and $|n+1,\downarrow\rangle$ states, in addition to the non-degenerate decoupled state $|0,\downarrow\rangle$ which we will describe in the next section.

1.4.2 Pure Dresselhaus effect (BIA)

Due to inherent crystalline properties, the Dresselhaus effect is a spin-orbit coupling phenomenon arising in crystalline material with bulk inversion asymmetry (BIA). In a two-dimensional electron gas (2DEG) system, the Dresselhaus effect can lead to a spin splitting of the energy bands, which can have important implications for spintronics applications [25]–[27]. The Dresselhaus effect can also occur, for example, in zincblende crystal structures where the bulk inversion symmetry is broken by the presence of impurities or defects [28]. The Dresselhaus effect can be mathematically described by a term in the Hamiltonian that couples the electron spin to its momentum like in the Rashba case. The Dresselhaus spin-orbit Hamiltonian can be written as:

$$H_D = \frac{\beta}{\hbar}(\sigma_x \pi_x - \sigma_y \pi_y). \tag{1.15}$$

where β is the Dresselhaus coefficient. π and σ_i are the momentum and Pauli matrices. For $B \neq 0$ using the ladder operators. The spin-dependent term that is proportional to the momentum of the electron, and it leads to a spin splitting of the energy bands. The Dresselhaus Hamiltonian could be written as follows:

$$H_D = \frac{\beta}{\sqrt{2\hbar\omega_c}\ell_c}(a^\dagger\sigma_+ + a\sigma_-). \tag{1.16}$$

The pure Dresselhaus effect can have interesting effects on the transport properties of 2DEG systems. For example, it can lead to magnetoresistivity, Shubnikov-de Haas oscillations where an electric current generates spin splitting of the energy bands. This effect can be helpful in spintronic applications, such as spin-based logic devices [29]. Here we define operator N_-:

$$N^- = a^\dagger a - \frac{\sigma_z}{2}, \tag{1.17}$$

which commutes with H_D:

$$[H_D, N^-] = 0. \tag{1.18}$$

This implies that in our system, an eigenstate of H_D is also an eigenstate of N^-. The states $|n, \uparrow\rangle$ and $|n + 1, \downarrow\rangle$ have eigenvalues $n - \frac{1}{2}$ which makes them degenerate:

$$N_- |n, \uparrow\rangle = (n - \frac{1}{2})|n, \uparrow\rangle \qquad (1.19)$$

$$N_- |n + 1, \downarrow\rangle = (n - \frac{1}{2})|n + 1, \downarrow\rangle. \qquad (1.20)$$

Hence $|n, \uparrow\rangle$ and $n + 1, \downarrow\rangle$ are degenerate with respect to the operator N_- as a conclusion, a linear combination of $|n, \uparrow\rangle$ and $n + 1, \downarrow\rangle$ is also an eigenstate of the Hamiltonian in eq. (1.16), this property allowed us to rewrite all the Hamiltonian elements in the basis of the $|n, \uparrow\rangle$ and $n + 1, \downarrow\rangle$ states in addition to the non-degenerate decoupled state $|0, \downarrow\rangle$ in terms of 2×2 blocks.

1.4.3 Hamiltonian Diagonalization

The Hamiltonian of a system as a mathematical operator that describes the energy of that system. To diagonalize the Hamiltonian, it is needed to find a set of basis states that are eigenstates of the Hamiltonian. The eigenvalues of the Hamiltonian on this basis are the energy levels of the system. Diagonalization also can be achieved through the use of unitary transformations, which preserve the inner product of the states. In some cases, it may not be possible to exactly diagonalize the Hamiltonian. In these cases, approximate methods such as perturbation theory may be used to obtain approximate solutions [30]. Starting with the Rashba Hamiltonian

$$H = a^\dagger a + \frac{1}{2} + \frac{\widetilde{\Delta}}{2}\sigma_z + \frac{\alpha}{\sqrt{2\hbar\omega_c}\ell_c}(a^\dagger\sigma_- + a\sigma_+), \qquad (1.21)$$

where $\bar{\Delta} = \frac{1}{2}g^* m$, we can calculate all the elements in the Hamiltonian and later on we can find the eigenvalues and eigenvectors on the right spot in the Hamiltonian. Using the fact that H and N_+ share a common eigenstates, we can diagonalize H in a 2×2 subspace, $\{|n, \uparrow\rangle, |n + 1, \downarrow\rangle\}$ where $n = 0, 1, 2, 3, ...$:

$$H_{2\times2} = \begin{pmatrix} \langle n, \uparrow |H|n, \uparrow\rangle & \langle n, \uparrow |H|n + 1, \downarrow\rangle \\ \langle n + 1, \downarrow |H|n, \uparrow\rangle & \langle n + 1, \downarrow |H|n + 1, \downarrow\rangle \end{pmatrix}$$

$$\qquad (1.22)$$

$$= \begin{pmatrix} n + \frac{1}{2} - \frac{\widetilde{\Delta}}{2} & 2a_R\sqrt{n} \\ 2a_R\sqrt{n} & n - \frac{1}{2} + \frac{\widetilde{\Delta}}{2} \end{pmatrix} = n\mathbb{1} + \begin{pmatrix} \frac{1}{2}(1 - \widetilde{\Delta}) & 2a_R\sqrt{n} \\ 2a_R\sqrt{n} & -\frac{1}{2}(1 - \widetilde{\Delta}) \end{pmatrix}. \quad (1.23)$$

The corresponding eigenvalues can be read by this 2×2 matrices resulting in eigenvalues:

$$\varepsilon_{n,\uparrow} = n - \sqrt{\frac{1}{4}(1 - \widetilde{\Delta})^2 + 4a_R^2(n + 1)} \tag{1.24}$$

$$\varepsilon_{n+1,\downarrow} = n + \sqrt{\frac{1}{4}(1 - \widetilde{\Delta})^2 + 4a_R^2(n + 1)}. \tag{1.25}$$

These energy levels are plotted in Fig. 1.10. Note that these are two eigenvalues belonging to different Landau levels, i.e. n and $n+1$. The corresponding of eigenenergy $\varepsilon_{n,\downarrow}$ belongs to adjacent 2×2 matrices:

$$\varepsilon_{n,\downarrow} = n - 1\sqrt{\frac{1}{4}(1 - \widetilde{\Delta})^2 + 4a_R^2(n + 1)}. \tag{1.26}$$

Considering the scaled Rashba constant $(a_R = \frac{\alpha}{\sqrt{2}\hbar\omega_c\ell_c})$ in Eqs. (1.24) and (1.25) shows that at higher magnetic fields when $(B \rightarrow \infty)$ makes a_R vanish, which explains why high magnetic field are considered as spin-orbit diminisher factor. In the same way, setting the α to zero $(a_R \rightarrow 0)$ returns us to the initial case in the absence of the Rashba term, resulting in the Zeeman splitting shape parallel along the inverse magnetic field.

In the Rashba case for example, with three Landau levels $n - 1$, n, and $n + 1$, each Landau level has two spin states splitted, i.e., $|n, \uparrow\rangle$ and $|n + 1, \downarrow\rangle$, and each state is coupled with the upper and lower Landau levels according to the Rashba Hamiltonian here, the eigenstate $|n, \downarrow\rangle$ is coupled with the states $|n, \uparrow\rangle$ and $|n + 1, \downarrow\rangle$ so we can write the $|n, \downarrow\rangle$ as a linear combination of these two states with the eigenvalue become:

By determining the eigenstates and eigenvalues of the upper and lower states, it is possible to obtain all the eigenenergies and eigenvectors of the intermediate states.

In a similar way we can diagonalize the Dresselhaus Hamiltonian

$$H = a^\dagger a + \frac{1}{2} + \frac{\widetilde{\Delta}}{2}\sigma_z + \frac{\beta}{\sqrt{2}\hbar\omega_c\ell_c}(a^\dagger\sigma_+ + a\sigma_-), \tag{1.27}$$

using the fact that $[H, N_-] = 0$. The corresponding 2×2 is now $|n, \uparrow\rangle, |n+1, \downarrow\rangle$ result
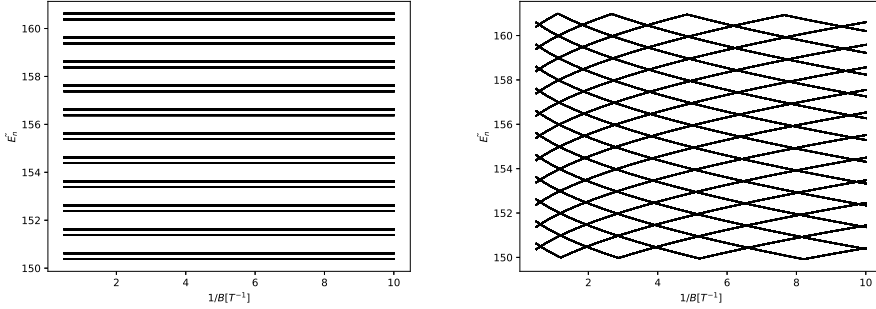
Figure 1.1: Comparison of Energy Spectra in the Presence of Rashba Spin-Orbit Coupling with $a_R = 6$ meV nm (right) and Pure Zeeman Effect with $a_R = 0$ (left)
.

in:

$$H_{2\times2} = \begin{pmatrix} \langle n,\uparrow |H|n,\uparrow \rangle & \langle n,\uparrow |H|n+1,\downarrow \rangle \\ \langle n+1,\downarrow |H|n,\uparrow \rangle & \langle n+1,\downarrow |H|n+1,\downarrow \rangle \end{pmatrix}$$

$$= \begin{pmatrix} n+\frac{1}{2}+\frac{\widetilde{\Delta}}{2} & 2a_D\sqrt{n} \\ 2a_D\sqrt{n} & n-\frac{1}{2}-\frac{\widetilde{\Delta}}{2} \end{pmatrix} = n\mathbb{I} + \begin{pmatrix} \frac{1}{2}(1+\widetilde{\Delta}) & 2a_D\sqrt{n+1} \\ 2a_D\sqrt{n+1} & -\frac{1}{2}(1+\widetilde{\Delta}) \end{pmatrix}. \quad (1.28)$$

Corresponding eigenvalues:

$$\varepsilon_{n,\uparrow} = n - \sqrt{\frac{1}{4}(1+\widetilde{\Delta})^2 + 4a_D^2(n+1)} \quad (1.29)$$

$$\varepsilon_{n+1,\downarrow} = n + \sqrt{\frac{1}{4}(1+\widetilde{\Delta})^2 + 4a_D^2(n+1)}. \quad (1.30)$$

Note the different sign in the Zeeman factor, $1 + \widetilde{\Delta}$ which has an opposite sign compared to the Rashba case in Eq. (1.24). This has important consequences in materials with large g factors as we investigated in this thesis.

1.4.4 Rashba + Dresselhaus effect case

By adding the Dresselhaus and Rashba case for non-zero magnetic fields the Hamiltonian become:

$$H_{RD} \quad = \quad a^\dagger a + \frac{1}{2} + \frac{\widetilde{\Delta}}{2}\sigma_z + \frac{\alpha}{\sqrt{2\hbar\omega_c}\ell_c}(a^\dagger\sigma_- + a\sigma_+) + \frac{\beta}{\sqrt{2\hbar\omega_c}\ell_c}(a^\dagger\sigma_+ + a\sigma_-)$$

$$(1.31)$$

As is shown in Fig [1.2] there are two sets of curves, one with a solid red line rep-
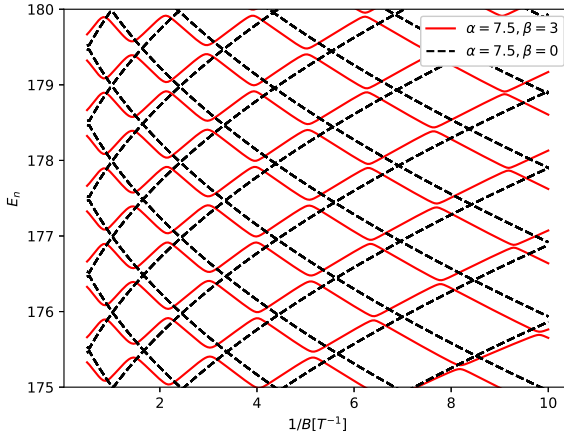
Figure 1.2: Comparison of energy spectra for two cases in LLs range [175:180]. The red solid line represents the spectrum with ($\alpha = 7.5, \beta = 3$), while the black dashed line corresponds to ($\alpha = 7.5, \beta = 0$).

resenting the Rashba case, and the other with a black dashed line representing the combined Rashba and Dresselhaus case. In the Rashba case, the spectrum has a square root shape see Eq. (1.24) with only crossings at intersections. However, in the Rashba-Dresselhaus case, there are still some crossings but in addition, anticrossings also appear , along with a slight shift at intersections. This is a result of the splitting of the Landau levels in the low-range magnetic field caused by adding the Dresselhaus term. It is apparent that the spectrum with Rashba and Dresselhaus is not solely characterized by crossings between energy levels, there exist numerous anticrossings that play a crucial role, see Sec:[1.4.5]

1.4.5 Parity

Here we are going to define the parity operator as:

$$P = e^{i\pi(n+\frac{1}{2}+\frac{1}{2}\sigma_z)}. \tag{1.32}$$

This parity operator commutes with a full Hamiltonian H_{RD} in Eq. (1.31). This has the consequences that the basis states can be separated into subspaces with a given parity eigenvalue: $P = \pm 1$. These subspaces are given by: $\{|0, \uparrow\rangle, |1, \downarrow\rangle, |2, \uparrow\rangle, |3, \downarrow\rangle, ...\}$ for +1 parity and for -1 parity : $\{|0, \downarrow\rangle, |1, \uparrow\rangle, |2, \downarrow\rangle, |3, \uparrow\rangle, ...\}$. Using the parity subspaces we can underestand the crossings and anticrossing in energy spectra. States belonging to the same parity subspace are coupled and will anticrossed. Conversely, states belonging to opposite parity subspaces are not coupled and will thus cross. The parity can affect the energy spectrum of the electrons in such a way that spectrum lines with the same parity open up a gap in the spectrum. Energy levels with the same parity values repel each other while levels with different parity cross each other until the next spectrum line [31], [32]. In Fig. 1.3 energy spectra of a full Hamiltonian model for Landau levels [150-160] in a two-dimensional electron gas system displays three different cases: a) Landau levels with Zeeman splitting, b) the pure Rashba case $\alpha = 7.5$, and c) the combined of Rashba $\alpha = 7.5$ and Dresselhaus terms $\beta = 3$ together. In case of a), the Zeeman splitting does not result in any differences in the spectrum as parallel lines with a separation of $\tilde{\Delta}$ are observed between each Landau level (LLs) for spin-up and spin-down. In case of b), the pure Rashba case shows the square-root shape of the spectrum lines for both spin-up and spin-down along the inverse magnetic field. Although these lines cross each other, the blue and red solid lines indicate that only states with the same parity actually cross, while the other ones meet at the point of intersections. This is because all the family spectrum lines for the spin-up and spin-down in the pure Rashba case are coupled by 2x2 matrices. In case c), the spectrum for Rashba and Dresselhaus nonzero terms results in lines with the same parity being able to see each other and opening up a gap in the spectrum. However, spectrum lines for different parity states still cross at intersections and cannot see each other and cross as such an envelope.

1.5 Density of states in 2DEG system

The density of states in a 2DEG system is a quantity that characterizes the electronic properties of the material and can be calculated using the formula with the 2DEG specific properties. Another important phenomenon in 2DEG systems is the Shubnikov-de Haas (SdH) oscillations, which can be related to the density of states.[7] These are oscillations in the magnetoresistance of the 2DEG system that occur due to the quantization of the electron motion in the presence of a magnetic field [7], [33], [34]. In
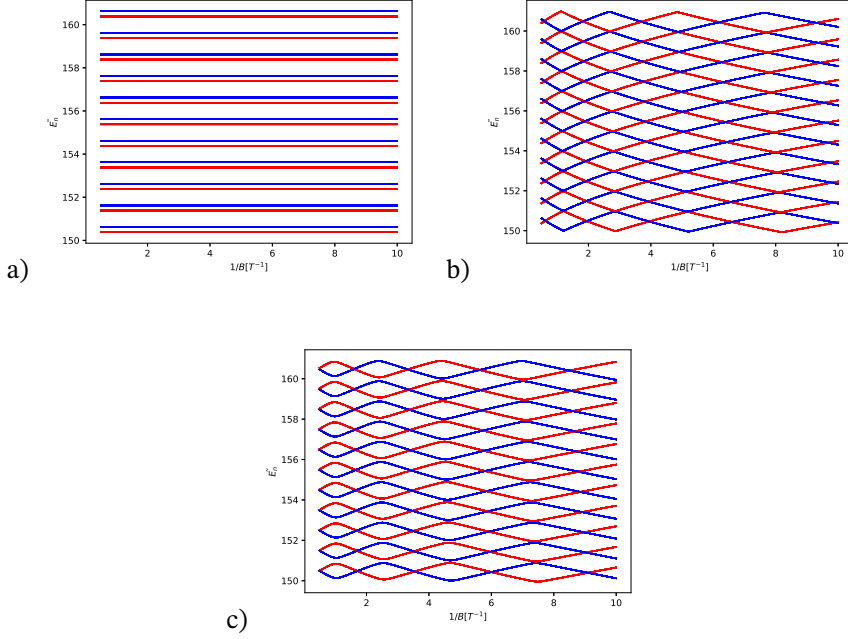
Figure 1.3: Energy spectrum of the Hamiltonian by parity for the Landau levels [150, 160] in three distinct cases of parity separation.(a) Zeeman splitting present with $\alpha, \beta = 0$, (b) pure Rashba coupling with $\alpha = 7.5$ meV nm^{-1}, and (c) Simultaneous presence of Dresselhaus and Rashba terms with $\alpha = 7.5$ meV nm^{-1} and $\beta = 3$ meV nm^{-1}, respectively.

the present model, the density of states in a magnetic field is given by:

$$D_{2D}(E, B) = \frac{|e|B}{h} \sum_{n,\sigma=\pm} \delta(E - \epsilon_{ns}) \tag{1.33}$$

The number of states per spin-degenerate Landau level is $|e|B/h$. For example, for the Landau levels and Zeeman case the energy comes with:

$$\epsilon_{n,\pm} = \hbar\omega_c(n + \frac{1}{2}) + \frac{1}{2}\mu g^* B. \tag{1.34}$$

The Fermi energy level in this case is determined by the highest occupied Landau level. The electron density at low magnetic fields is therefore given by:

$$n_s = \frac{|e|B}{h} \frac{E_F}{\hbar\omega_c} = \frac{m^*}{\pi h^2} E_F. \tag{1.35}$$

Figure 1.4 also illustrates the energy spectrum of a two-dimensional electron gas
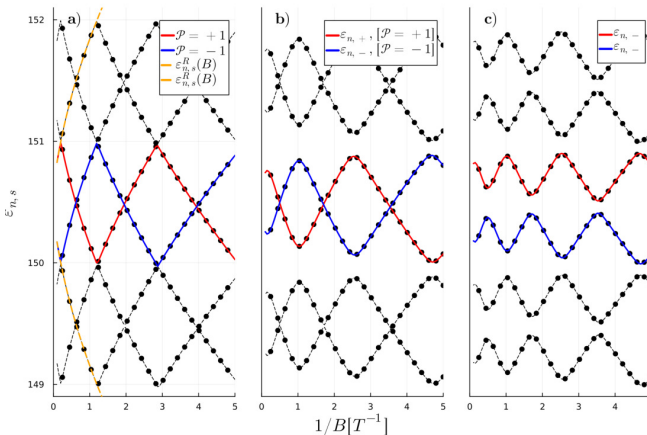
Figure 1.4: This figure shows the energy spectrum in range [149-152] LLs, plotted simultaneously. providing insight into the relationship between numerical and analytical point of view for three cases of a) pure Rashba b)Rashba+ Dresselhaus c)Rashba+Dresselhaus+in-plane magnetic field completely matched up.

(2DEG) system in a specific range of LLs and Rashba and Dresselhaus, plotted simultaneously with the Fermi level. The reason behind the almost linear horizontal dependent shape is due to $E_F/\hbar\omega_c$, as E_F is relatively 100 times larger than $\hbar\omega_c$. The energy spectrum is represented by a series of lines, each corresponding to a different Landau level along the magnetic field. The Fermi energy is represented by a solid line that intersects each spectrum line at a single point. The Landau levels are separated by the cyclotron energy, and their position in energy space is determined by the strength of the magnetic field [7], [35]. It is determined by the temperature and the electron density of the 2DEG system. The Fermi curve is a linear function of the inverse magnetic field, and it intersects each Landau level at a single point. It also allows the investigation of the effect of the magnetic field on the electronic properties of the 2DEG system, such as the density of states and conductivity. As the magnetic field (B) approaches zero, the separation between Landau levels decreases, leading to a continuous distribution of states rather than discrete peaks. This results in a constant two-dimensional density of states. Additionally, the broadening of Landau

levels due to various factors such as disorder or temperature also contributes to the smearing out of the discrete density of states peaks. This means that, in the limit of $B = 0$, the Landau levels and the resulting density of states are no longer distinguishable, resulting in a smooth and constant density of states. To understand the relationship between the density of states and the broadening of electronic states, it is useful to consider a simplified scenario in which inter-Landau-level scattering is neglected and the broadening is solely due to a lifetime effect, modeled by a Lorentzian function. This allows us to clearly illustrate the interdependency between the density of states and the broadening of electronic states. By assuming a Lorentzian density of states, we can see how the shape and width of the electronic states are affected by the lifetime broadening and how this, in turn, affects the overall density of states.

$$\delta(E - \epsilon_{ns}) = \frac{1}{\pi} \frac{\hbar/2\tau_q}{(E - \epsilon_{ns})^2 + (\hbar/2\tau_q)^2} \tag{1.36}$$

The Lorentzian function is preferred over the Gaussian when modeling density of states in solid-state physics. It can better capture electronic states near the Fermi energy due to its sharp peak with a long tail. It is also well suited for modeling broadening of electronic states from factors like disorder or temperature [7], [36].

1.6 F-Funciton

The F-function is a continuous function that represents the quantum number for a spin up and down for each Landau level in a two-dimensional electron gas (2DEG) system. It is defined by the relation:

$$\epsilon_{n,s}(B) = \epsilon_F \leftrightarrow n = F_s(B, \epsilon_F) \tag{1.37}$$

The F-function is used to calculate the density of states (DOS) of the 2DEG system, which is a measure of the number of states available to the system at a given energy. To see how the $F-$function appears in the DOS we look at its definition

$$D(E) \quad = \quad \frac{eB}{h} \sum_{n,s} \delta(E - \hbar\omega_c \epsilon_{ns}) = \frac{eB}{\hbar} \sum_{n,s} \frac{1}{\hbar\omega_c |\frac{\partial \epsilon_n}{\partial n}|} \delta(n - F_s(E, B)), \tag{1.38}$$

where we used standard δ-function relation. The quantity $|\frac{\partial \epsilon_n}{\partial n}|$ is approximately equal to 1 for all relevant spin-orbit parameter values. Using this, we can write Eq. (1.38) as :

$$D(E) = \frac{m}{2\pi\hbar^2} (\sum_{n,s} (n - F_s(E, B))). \tag{1.39}$$

Next, we apply the Poisson summation formula [7] which allows us to write DOS as:

$$D(E) = \frac{m}{2\pi\hbar^2}\left(1 + \sum_{l=1}^{\infty} \cos(2\pi F_+)\cos(2\pi F_-).\right) \tag{1.40}$$

Here we introduced the sum and differences of the F-function:

$$F_+ = \frac{F_+ + F_-}{2} \tag{1.41}$$

$$F_- = \frac{F_+ - F_-}{2}. \tag{1.42}$$

These functions have an important interpretation since they describe the slow and fast oscillations, F_- and F_+ respectively. To clarify these two fast and slow oscillations we consider the case of pure Rashba SOI where the $F-$functions can be calculated exactly [32], [33], [35]:

$$F_\downarrow(\epsilon_F, B) = \epsilon_F + (\frac{\alpha}{\sqrt{2\hbar\omega_c l_c}})^2 \tag{1.43}$$
$$- \sqrt{(\frac{\alpha}{\sqrt{2\hbar\omega_c l_c}})^4 + 2\epsilon_F(\frac{\alpha}{\sqrt{2\hbar\omega_c l_c}})^2 + \frac{1}{4}(1-\bar{\Delta})^2}$$

$$F_\uparrow(\epsilon_F, B) = \epsilon_F - 1 + (\frac{\alpha}{\sqrt{2\hbar\omega_c l_c}})^2 \tag{1.44}$$
$$+ \sqrt{(\frac{\alpha}{\sqrt{2\hbar\omega_c l_c}})^4 + 2\epsilon_F(\frac{\alpha}{\sqrt{2\hbar\omega_c l_c}})^2 + \frac{1}{4}(1-\bar{\Delta})^2}$$

since we are looking at a low range of magnetic field so the Zeeman term and $(\frac{\alpha}{\sqrt{2\hbar\omega_c l_c}})^2$ leads to a negligible value and the above equations are reduced to:

$$F_\uparrow(\epsilon_F, B) \approx \epsilon_F + \alpha\frac{k_F}{\hbar\omega_c} \tag{1.45}$$

$$F_\downarrow(\epsilon_F, B) \approx \epsilon_F - \alpha\frac{k_F}{\hbar\omega_c} \tag{1.46}$$

Where k_F is the radius of the Fermi sphere. Looking at the definition of F_+ and F_- we obtain:

$$F_+ = \frac{E_F}{\hbar\omega_c} = \frac{h}{2e}n_s\frac{1}{B} \tag{1.47}$$

$$F_- = \frac{\alpha k_F}{\hbar\omega_c}. \tag{1.48}$$

The former equation gives simply the standard Shubnikov de Haas oscillations frequency and the latter equation gives the slower SOI related beating frequency. This forms the foundation of the theory we have applied in this thesis. Since the plot is in terms of the inversed magnetic field we need to combine $\omega_c = \frac{eB}{m}$ and substitute the ϵ_F with E_F to have all terms according to $\frac{1}{B}$, then reduced F-functions for Rashba:

$$F_\downarrow(E_F, B) = \frac{E_F}{\frac{he}{m}}\frac{1}{B} + (\frac{\alpha k_F}{(\frac{he}{m})})\frac{1}{B} = n + \Delta n \tag{1.49}$$

$$F_\uparrow(E_F, B) = \frac{E_F}{\frac{he}{m}}\frac{1}{B} - (\frac{\alpha k_F}{(\frac{he}{m})})\frac{1}{B} = n \tag{1.50}$$

In $F_\uparrow - F_\downarrow$ case, the slope magnitude is equal to $(\frac{\alpha k_F}{(\frac{he}{m})})$ in the spectrum of energy two states $|n+\Delta n, \uparrow\rangle$ and $|n, \downarrow\rangle$ intersect with each other in a specific magnetic points B^* as the eigenvalues of energies $\epsilon_{n+\Delta n, \uparrow}$ and $\epsilon_{n, \downarrow}$ have positive and negative square root shape.

$$F_\uparrow - F_\downarrow = 2(\frac{\alpha k_F}{(\frac{he}{m})})\frac{1}{B} \tag{1.51}$$

$$F_\uparrow + F_\downarrow = 2\frac{E_F}{(\frac{he}{m})}\frac{1}{B} \tag{1.52}$$

Here the intersection point in energy spectra and Fermi line at magnetic point B^* is the max value in $\frac{F_\uparrow - F_\downarrow}{2}$ plot which is equal to 0.5 where it starts negative sign change in slope.

$$F_\uparrow(E_F, B) = \frac{m}{he}(E_F + \alpha k_F)(\frac{1}{B} - \frac{1}{B^*}) + \frac{m}{he}(E_F + \alpha k_F)\frac{1}{B^*} \tag{1.53}$$

$$= \frac{m}{he}(E_F + \alpha k_F)(\frac{1}{B} - \frac{1}{B^*}) + n + \Delta n \tag{1.54}$$

$$F_\downarrow(E_F, B) = \frac{m}{he}(E_F - \alpha k_F)(\frac{1}{B} - \frac{1}{B^*}) + n \tag{1.55}$$

With this new looks of $F_\uparrow$ and $F_\downarrow$ in eq. (1.53) and (1.55) it abled us to follow $\frac{F_\uparrow - F_\downarrow}{2}$ along inverse magnetic field at the $\frac{1}{B^*}$ to have a + and - linear slope before and after $\frac{1}{B^*}$.

now if $\frac{1}{B} - \frac{1}{B^*} < 0$ then:

$$\frac{F_\uparrow - F_\downarrow}{2} = \frac{\alpha k_F m}{\hbar e}(\frac{1}{B} - \frac{1}{B^*}) + \frac{\Delta n}{2} \qquad (1.56)$$

So the Slope magnitude is $+\frac{\alpha k_F m}{\hbar e}$ until this assumption $\frac{1}{B} - \frac{1}{B^*} < 0$ is satisfied. and if $\frac{1}{B} - \frac{1}{B^*} > 0$ then:

$$\frac{F_\uparrow - F_\downarrow}{2} = -\frac{\alpha k_F m}{\hbar e}(\frac{1}{B} - \frac{1}{B^*}) \qquad (1.57)$$

Here the slope sign under a higher magnetic field than B^* changed to $\frac{\alpha k_F m}{\hbar e}$ and $-\frac{\alpha k_F m}{\hbar e}$ remains up to the next intersection which is changed up to the next intersection point in the spectrum of energy. with the odd integer Δn it is the max point in the $\Delta F - Function$ equal $\frac{1}{2}$ and by even integers it would have taken zero level. In ΔF-funcitons plot it has been examined our major term $\frac{F_\uparrow - F_\downarrow}{2}$ with the critical intersection point at inverse magnetic field axis by its slope magnitude. This figure illustrates one more point in that when it is plotted in a numerical point of view the $\frac{F_\uparrow - F_\downarrow}{2}$, the two spectrum lines reach the intersection $\frac{1}{B^*}$ point but do not cross each other. This is due to different ways of interpreting as a point of computer view.The difference between F-functions $(F_\uparrow - F_\downarrow)$ typically exhibits a sawtooth pattern because of the spin degeneracy of the Landau levels in a two-dimensional electron gas (2DEG) system. The spin degeneracy of a Landau level refers to the number of spin states that are available at that energy. In a 2DEG system, the spin degeneracy of each Landau level is 2, which means that there are two spin states available at each energy level. The difference gap is related to the spin degeneracy of the Landau levels, and it is used to calculate the density of states (DOS) of the 2DEG system. This $\Delta F/2$ exhibits a sawtooth pattern between 0 and 0.5 because the energy separation between the two spin states increases linearly with the wave vector,inverse magnetic field and Rashba constant. As a result, the density of states will show a series of peaks and valleys, with the peaks corresponding to the maxima of the sawtooth pattern and the valleys corresponding to the minima. This is a consequence of the spin-orbit coupling in the system, which causes the spin states to have a different energy dispersion.

1.6.1 Fast and Slow Oscillation

SdH oscillations are a manifestation of the quantization of the electron's cyclotron orbits in a magnetic field, which results in the periodic variation of the density of states at the Fermi level. The amplitude of the SdH oscillations is proportional to
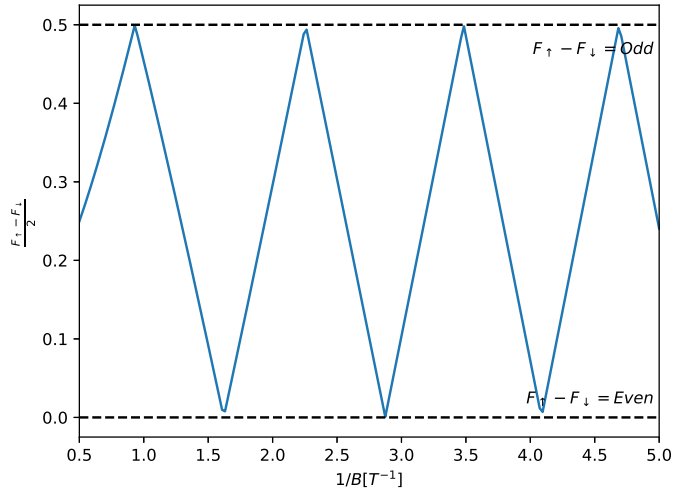
Figure 1.5: Sign changing in terms of $\frac{1}{B^*}$ sawtooth shape as a schematic perspective of $\frac{F_\uparrow - F_\downarrow}{2}$
, the Sawtooth behavior of difference between F-functions as a function of inverse magnetic field strength.

the magnetoresistance, which is the change in the electrical resistance of a material in response to a magnetic field. These oscillations are a valuable tool for studying the electronic properties of materials and have been used to determine the effective mass, Fermi surface topology, and many-body interactions of electrons in a variety of systems, including metals, semimetals, and semiconductors [37]. The oscillatory part of the density of states (DOS) has two types of oscillations: fast and slow. The slow oscillations result from $\cos(2\pi s(\frac{F_\uparrow - F_\downarrow}{2}))$, while the fast oscillations arise from $\cos(2\pi s(\frac{F_\uparrow + F_\downarrow}{2}))$.

1.7 Discrete Fourier (DFT) and Fast Fourier transform (FFT)

1.7.1 discrete Fourier Transform(DFT)

The discrete Fourier transform (DFT) is a mathematical operation that decomposes a sequence of complex numbers into its component frequencies. The DFT is defined as a sum over the sequence of complex numbers, with each element of the sequence
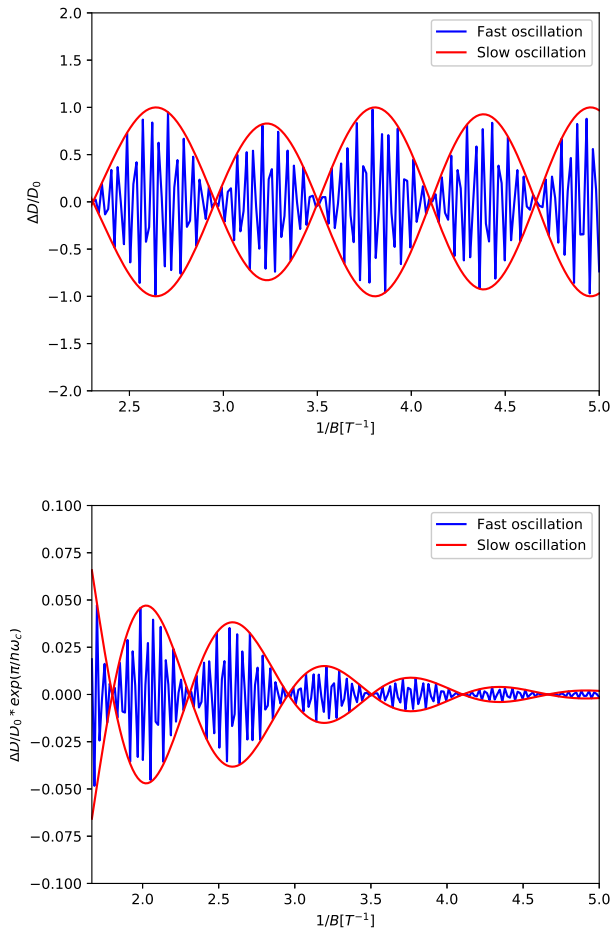
Figure 1.6: Fast oscillations (blue) and slow oscillations (red) are shown as an envelope where the main magnetooscillations depends on this part of the Density of states and the (b) figure is the DOS in terms of inverse magnetic field both in pure Rashba case.α =7.5 meV nm

weighted by a complex exponential function. The DFT has a wide range of applications in fields such as signal processing, image processing, and data analysis. One of the key properties of the DFT is its ability to transform a sequence of time-domain samples into a sequence of frequency-domain samples, known as the spectrum of the sequence. The spectrum of a sequence represents the distribution of energy among

the different frequencies present in the sequence, and it can provide important information about the characteristics of the sequence. The DFT has a number of important properties, including the convolution theorem, which states that the DFT of the convolution of two sequences is equal to the product of the DFTs of the individual sequences. The DFT also has a number of symmetries, such as the conjugate symmetry property, which states that the DFT of a complex conjugate sequence is equal to the complex conjugate of the DFT of the original sequence. The discrete Fourier transform (DFT) is a mathematical operation that decomposes a sequence of complex numbers into its component frequencies. The DFT has a wide range of applications in fields such as signal processing, image processing, and data analysis, and it has important properties such as the convolution theorem and the conjugate symmetry property. The DFT can transform a sequence of time-domain samples [38]–[40].

1.7.2   Fast Fourier Transform (FFT)

The Fast Fourier Transform (FFT) is an algorithm that is used to efficiently compute the discrete Fourier transform (DFT) of a sequence. The discrete Fourier transform is a mathematical operation that decomposes a sequence into its component frequencies, and it has a wide range of applications in fields such as signal processing, image processing, and data analysis. The FFT algorithm was developed by mathematician and physicist Cooley and John Tukey in the 1960s [41], and it has since become an essential tool in many scientific and engineering disciplines. The FFT algorithm is based on the principle of divide and conquer, and it involves breaking down the DFT of a sequence into smaller DFTs that can be computed more efficiently. One of the key advantages of the FFT algorithm is its computational efficiency. The FFT algorithm can compute the DFT of a sequence in O(n log n) time, which is much faster than the $O(n^2)$ time required by the standard algorithm for computing the DFT. This makes the FFT algorithm particularly useful for analyzing large datasets or for real-time processing of signals. the Fast Fourier Transform (FFT) is an algorithm that is used to efficiently compute the discrete Fourier transform (DFT) of a sequence. The FFT algorithm was developed in the 1960s and has become an essential tool in many scientific and engineering disciplines due to its computational efficiency. The FFT algorithm can compute the DFT of a sequence in O(n log n) time, which is much faster than the (n^2) time required by the standard algorithm for computing the DFT. There is a relationship between the density of states (DOS) and the FFT of a signal. The FFT of a signal can be used to compute the power spectrum of the signal, which is a measure of the power of the signal(The power of a signal is the sum of the absolute squares of its time-domain samples divided by the signal length. The function allows you to estimate signal power in one step.) at different frequencies. The power spectrum of a signal is related to the DOS of the system, as the power at a particular frequency is proportional to the number of states available at that energy, the density of states (DOS) is a measure of the number of states available to a system

at a given energy, and it provides information about the electronic properties of the system. The Fast Fourier Transform (FFT) is an algorithm that is used to efficiently compute the discrete Fourier transform (DFT) of a sequence, and it can be used to analyze the frequency content of a signal [33], [42], [43]. There is a relationship between the DOS and the FFT of a signal, as the power spectrum of the signal is related to the DOS of the system. The FFT analysis reveals the frequency components of
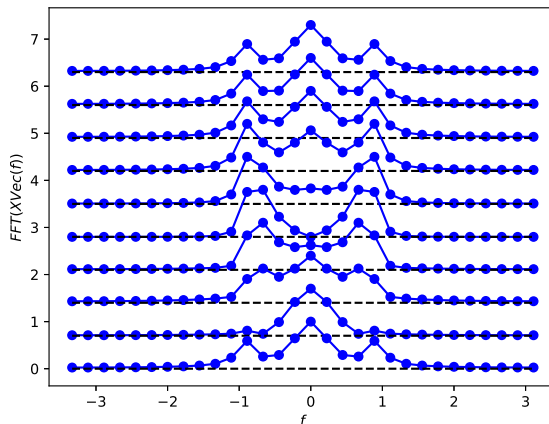
Figure 1.7: This figure shows the Fast Fourier Transform (FFT) of the magnetoresistance signal for a sample of a material with both Rashba and Dresselhaus spin-orbit coupling ($\alpha = 7.5, \beta = 3$ meV nm)in the presence of an in-plane magnetic field with varying angles θ ranging from 5 to 90 degrees.

the magnetoresistance signal and provides insight into the magnetic anisotropy and spin-orbit coupling properties of the material, which are sensitive to the angle of the applied magnetic field [44]. We have plotted two different Fast Fourier Transforms (FFTs) on the same graph at different angles in order to better understand the role of the FFT and electron density at the Fermi level.

1.8 Conclusion

In general, peaks or spikes in a Fast Fourier Transform (FFT) plot indicate the presence of specific frequency components in the original signal. The magnitude of the peak represents the strength of that frequency component, and the position of the peak along the frequency axis corresponds to the frequency of the component. The FFT plot allows us to identify and analyze the different frequency components of a
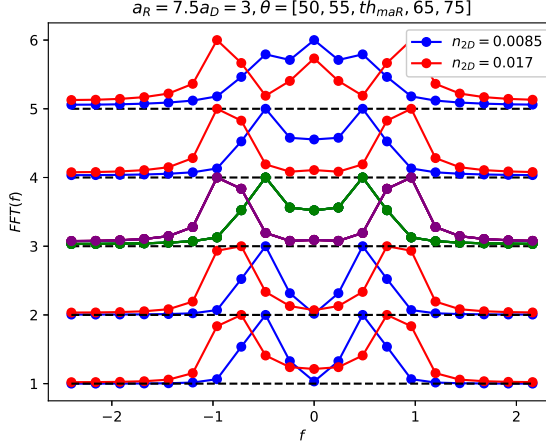
Figure 1.8: This figure shows the Fast Fourier Transform (FFT) with both Rashba and Dresselhaus spin-orbit coupling ($\alpha = 7.5, \beta = 3$ meV nm)in the presence of an in-plane magnetic field with varying angles θ ranging from [50-75] for two $n_{2D} = 0.0085$ in blue and $n_{2D} = 0.017$ in solid red line.

signal and can be useful in a wide range of applications such as signal processing, image analysis and telecommunications. In the case of density of states (DOS) or magnetoresistance signal, peaks or spikes in the FFT plot indicates the presence of specific energy levels or specific frequency components in the signal, respectively [45]. In the case of the density of states, it can be used to understand the electronic properties of a material, like the number of available states at a specific energy level. The FFT can be used to analyze the DOS signal and identify the energy levels that are more likely to be occupied by electrons. This can give us insight into the electronic band structure of the material and its electronic conductivity. On the other hand, for the magnetoresistance signal, a peak or spike in the FFT plot can indicate the presence of a specific frequency component in the signal, which may be related to the magnetic properties of the material. By analyzing the FFT of the magnetoresistance signal, it is possible to extract information about the magnetic properties of the material, such as its magnetic anisotropy or the way in which the magnetic properties depend on the direction of the applied magnetic field [46].

1.8.1 In-plane Magnetic field in pure Rashba case

Here it is assumed two crossing states in the spectrum of Energy with their linear combination of shared basis states and matrix elements in new basis $|\psi_{n,\downarrow}\rangle$ and $|\psi_{m,\uparrow}\rangle$:

$$|\psi_{n,\downarrow}\rangle = (\cos(\frac{\theta_n}{2})|n,\downarrow\rangle + \sin(\frac{\theta_n}{2})|n-1,\uparrow\rangle$$

$$|\psi_{m,\uparrow}\rangle = (-\sin(\frac{\theta_{m+1}}{2})|m+1,\downarrow\rangle + \cos(\frac{\theta_{m+1}}{2})|m,\downarrow\rangle$$

$$(1.58)$$

And here we know that it could have been equal to any number of arbitrary of n $m =, n-1, n+1$, the 2×2 matric elements are implemented in the Hamiltonian as it comes:

$$H_{ns,ms'} = \langle ns|H_R|ms'\rangle + \frac{\widetilde{\Delta}}{2}x_p\sigma_x$$

$$= (n + \frac{1}{2} + \frac{\widetilde{\Delta}}{2})\delta_{nm}\delta_{ss'} + \frac{\widetilde{\Delta}}{2}.x_p\langle n,s|\sigma_x|m,s'\rangle + \frac{\alpha}{\sqrt{2}\hbar\omega_c\ell_c}\langle ns|a^\dagger\sigma_+ + a\sigma_-|ms'\rangle$$

$$(1.59)$$

Here it has just been implemented an extra term come from in-plane intense component of the Zeeman term in Hamiltonian that makes some nonzero elements in the same landau levels spin quantum number without any changes in quantum numbers.

$$B_\perp\sigma_z + B_\parallel\sigma_x \qquad (1.60)$$

$$\frac{\widetilde{\Delta}}{2}.x_p\begin{pmatrix}\langle\psi_{n,\downarrow}|\sigma_x|\psi_{n,\downarrow}\rangle & \langle\psi_{n,\downarrow}|\sigma_x|\psi_{n,\uparrow}\rangle \\ \langle\psi_{n,\uparrow}|\sigma_x|\psi_{n,\downarrow}\rangle & \langle\psi_{n,\uparrow}|\sigma_x|\psi_{n,\uparrow}\rangle\end{pmatrix} \quad (1.61)$$

by definition of new Hamiltonian as:

$$H = H_R + \frac{\widetilde{\Delta}}{2}(x_p\sigma_x) \qquad (1.62)$$

It has been two states that crossed each other even though implementing the in-plane magnetic field it opens up a gap that shows they have couplings [32], [47], [48].

$$\langle\psi_{n\downarrow}|H_R|\psi_{m\uparrow}\rangle = 0 + \frac{\widetilde{\Delta}}{2}x_p\langle\psi_{n,\downarrow}|\sigma_x|\psi_{m,\uparrow}\rangle$$

$$\langle\psi_{n\downarrow}|H_R|\psi_{m\downarrow}\rangle = \varepsilon_{n\downarrow} + \frac{\widetilde{\Delta}}{2}x_p\langle\psi_{n,\downarrow}|\sigma_x|\psi_{m,\downarrow}\rangle$$

$$\langle\psi_{m\uparrow}|H_R|\psi_{m\uparrow}\rangle = \varepsilon_{m\uparrow} + \frac{\widetilde{\Delta}}{2}x_p\langle\psi_{m,\uparrow}|\sigma_x|\psi_{m,\uparrow}\rangle$$

$$\langle\psi_{n\downarrow}|H_R|\psi_{m\uparrow}\rangle = 0 + \frac{\widetilde{\Delta}}{2}x_p\langle\psi_{n,\downarrow}|\sigma_x|\psi_{m,\uparrow}\rangle$$

Upon examination of the Hamiltonian, it is clear that any changes to Landau levels
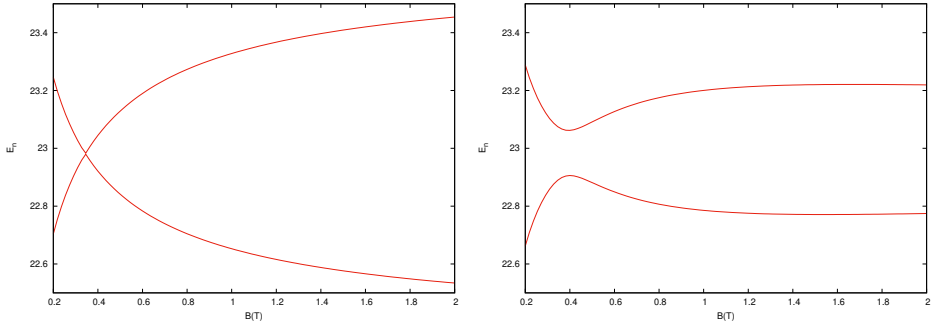
Figure 1.9: In this figure it has been shown the gap coming from implementing the in-plane magnetic field with a definition of a dimensionless parameter x_p=3 (right)and σ_x operator in the presence of Rashba effect with a_R=6 meV nm versus the regular Rashba case without in-plane magnetic field with the same a_R=6 meV nm (left)
.

can be attributed solely to alterations in the nondiagonal elements. When δ is set to zero, a $2|V|$ open gap emerges due to the influence of the in-plane magnetic field. This results in a coupling between two adjacent states, allowing for mutual interaction between them. It is important to note that the magnetic field can be determined for any given values of n and Δn, where Δn represents the crossing or non-crossing nature of adjacent Landau levels in the spectrum. By setting δ to zero, we observe the emergence of a gap in only two specific Landau levels, caused by the in-plane magnetic field. We can use this information to calculate the precise value of B for any number of adjacent Landau levels, such as n, n+1, and n+2, thereby expanding

our understanding of the behavior of the system under varying magnetic fields.

$$V = \frac{\widetilde{\Delta}}{2} x_p \langle \psi_{n\downarrow} | \sigma_x | \psi_{m\uparrow} \rangle \tag{1.63}$$

It is found that the in-plane magnetic field opens a gap in the spectrum of Energies, In our attempts to investigate the effects of low magnetic fields, we have found that increasing the magnetic field leads to the disappearance of one of the crossing branches and the associated spin-orbit interactions. This phenomenon is particularly evident in the Rashba case, where an analytical expression has been derived for low magnetic field regimes using the Hamiltonian parameters obtained through the implementation of the Zeeman and Rashba terms. These findings provide valuable insights into the behavior of spin-orbit interactions under varying magnetic fields, with potential implications for the design and optimization of electronic devices that rely on these interactions [32], [49], [50].
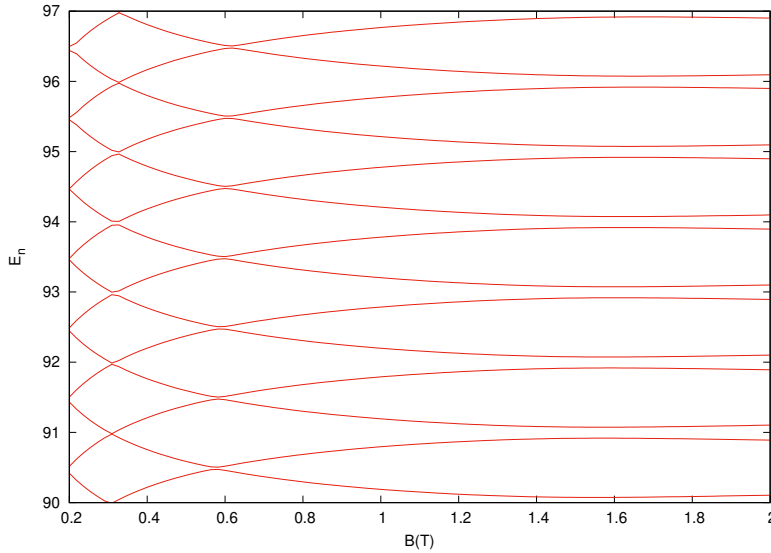
Figure 1.10: In this figure it has been shown with the x_p=3 there is a gap between 2 crossing lines of the landau levels in high Landau levels [90:97] and with the same magnetic(Zeeman) and Rashba parameters.

Chapter 2

Analytical Method

Quantum oscillations in 2D electron gases with spin-orbit and Zeeman interactions

Denis R. Candido,[1] Sigurdur I. Erlingsson,[2] Hamed Gramizadeh,[2] João Vitor
I. Costa,[3] Pirmin J. Weigele,[4] Dominik M. Zumbühl,[4] and J. Carlos Egues[3, 4]

[1]*Department of Physics and Astronomy, University of Iowa, Iowa City, Iowa 52242, USA*
[2]*Department of Engineering, Reykjavik University, Menntavegi 1, IS-102 Reykjavik, Iceland*
[3]*Instituto de Física de São Carlos, Universidade de São Paulo, 13560-970 São Carlos, SP, Brazil*
[4]*Department of Physics, University of Basel, CH-4056, Basel, Switzerland*
(Dated: April 28, 2023)

Shubnikov-de Haas (SdH) oscillations are the fingerprint of the Landau and Zeeman splitting level structure on the resistivity in presence of a moderate magnetic field before full quantization is manifest in the integer quantum Hall effect. These oscillations have served as a paradigmatic experimental probe and tool for extracting key semiconductor parameters such as carrier density, effective mass m^*, Zeeman splitting with g-factor g^*, quantum scattering time and Rashba α and Dresselhaus β spin-orbit (SO) coupling parameters. Analytical descriptions of the SdH oscillations are available for some special cases, but the generic case with all three terms simultaneously present has not been solved analytically so far, seriously hampering the analysis and interpretation of experimental data. Here, we bridge this gap by providing an analytical formulation for the SdH oscillations of 2D electron gases (2DEGs) with simultaneous and arbitrary Rashba, Dresselhaus, and Zeeman interactions. We use a Poisson summation formula for the density of states of the 2DEG, which affords a complete yet simple description of the oscillatory behavior of its magnetoresistivity. Our analytical and numerical calculations allow us to extract the beating frequencies, quantum lifetimes, and also to understand the role of higher harmonics in the SdH oscillations. More importantly, we derive a simple condition for the vanishing of SO induced SdH beatings for all harmonics in 2DEGs: $\alpha/\beta = [(1 - \tilde{\Delta})/(1 + \tilde{\Delta})]^{1/2}$, where $\tilde{\Delta} \propto g^* m^*$ is a material parameter given by the ratio of the Zeeman and Landau level splitting. This condition is notably different from that of the persistent spin helix at $\alpha/\beta = 1$ for materials with large g^* such as InAs or InSb. We also predict beatings in the higher harmonics of the SdH oscillations and elucidate the inequivalence of the SdH response of Rashba-dominated ($\alpha > \beta$) vs Dresselhaus-dominated ($\alpha < \beta$) 2DEGs in semiconductors with substantial g^*. We find excellent agreement with recent available experimental data of Dettwiler *et al.* Phys. Rev. X **7**, 031010 (2017), and Beukman *et al.*, Phys. Rev. B **96**, 241401 (2017). The new formalism builds the foundation for a new generation of quantum transport experiments and spin-orbit materials with unprecedented physical insight and material parameter extraction.

I. INTRODUCTION

The spin-orbit (SO) interaction couples the orbital and spin degrees of freedom, not only forms the basis for a range of spin related effects such as the spin Hall effect[1–4] and the persistent spin helix[5–7], but also underlies the physical mechanisms of new phases of matter, e.g., topological insulators, quantum spin Hall materials [8–10], and Majorana[11–13], Dirac and Weyl fermions[14]. Accordingly, advancing techniques and methods to measure and extract SO couplings from experimental data are crucial for the development of these fields.

Shubnikov-de Haas (SdH) oscillations[16,17] are among the best techniques to probe simultaneously spin- and charge-related quantities associated to electrons in semiconductors, including effective masses, gyromagnetic ratios, quantum scattering times, densities and SO couplings. Most recently, they have been crucial to the study and understanding of new materials, as for example, 2D-materials, transition metal dichalcogenides, van der Waals heterostructures[18–25], and also materials hosting new phases of matter e.g., topological insulators[26], unconventional superconductivity[27] and correlated insulator behavior[28]. It has also been used to establish the presence of nodal-lines[29], Berry's phase[30,31], and differ-

ent topology of Fermi surfaces[32]. SdH oscillations are magneto-oscillations in the resistivity and originate from the sequential crossings of the discrete Landau Levels (LLs) through the Fermi energy. Without SO coupling and in the low-field regime, the period of the SdH oscillations can be related to the density of the electron gas[33]. In the presence of SO interaction, on the other hand, the energy spectrum changes dramatically thus leading to additional frequencies in the magnetoresistivity and hence beatings, Figs. 1(a). This was first theoretically described semiclassically by Das *et. al.*,[34]. In the so-called Onsager's picture, different sub-bands possess different Sommerfeld quantized orbits (playing the role of the LLs), which cross the Fermi energy with different frequencies in B^{-1}. The spin-split bands give rise to two distinct oscillating frequencies in the magnetotransport. The standard experiment relies on Fourier analyzing the measured SdH oscillations. An experimental method introduced in Refs. 35–37 has often been used to estimate the strength of the Rashba coupling via the splitting of the Fourier frequency peaks. However, these methods have been criticized for not accounting for the Zeeman splitting (through the g-factor g^*) nor for the additional Dresselhaus SO coupling[15].
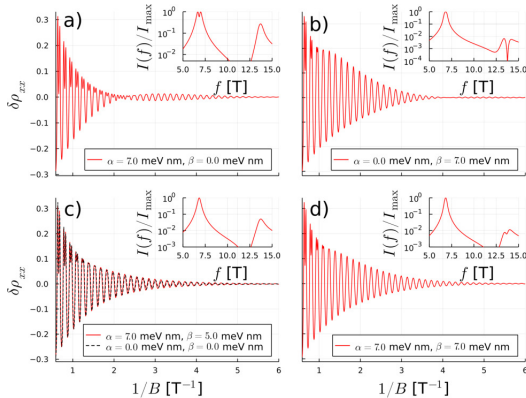
There have been some attempts to analyze the SdH os-

FIG. 1. Magnetoresistivity for a) pure Rashba $\alpha = 7.0\,\mathrm{meV\,nm}$ and b) pure Dresselhaus $\beta = 7.0\,\mathrm{meV\,nm}$ with $m^* = 0.019m_o$ and $n_{2D} = 3.3 \times 10^{11}\,\mathrm{cm}^{-2}$ from Ref. 15. The curves in a) and b) are not the same due to the large g–factor $g^* = -34$. The insets display the normalized FFT including the 2nd harmonic. The presence of beating nodes in $\delta\rho_{xx}$ are clearly visible in a) the fundamental and b) the 2nd harmonic, see Fig. 8. The condition for the *absence* of beatings (single peak for each harmonic) is $\alpha = 7.0\,\mathrm{meV\,nm}$ and $\beta = 5.0\,\mathrm{meV\,nm}$, shown in c), but not $\alpha = \beta = 7.0\,\mathrm{meV\,nm}$, the persistant spin helix case, shown in d), clearly exhibiting a beating (here a splitting of 2nd harmonic peak).

cillations taking into account both α, β *and* g^*. However, these mostly involved qualitative comparison with the energy spectrum of pure Rashba and pure Dresselhaus[38,39]. In Ref. 40, fully numerical calculations of magneto-oscillations were performed but for relatively high magnetic fields and low electron densities, far away from the regime of recent experimental works[41]. Moreover, it was realized that in the absence of the Zeeman interaction, important features are absent. More specifically, without accounting for the spin mixing generated by the magnetic field (via the Zeeman interaction), predictions become imprecise[42], and even fail to describe phenomena such as magnetic inter-subband scattering[43] and magnetic breakdown[44]. In general, full quantum mechanical numerics are generally done in order to check agreement with experiments, which are neither very practical nor elucidate much of the physics happening in those systems[41,45]. Finally, all the previous works have neglected the influence of higher harmonics, recently seen experimentally[46].

Here, we present a detailed investigation of SdH oscillations in the presence of SO couplings of both Rashba α and Dresselhaus β types *and* Zeeman interaction with g-

factor g^*. Our main result is the derivation, for the first time in the literature, of a simple analytical expression for the SdH oscillations in the presence of simultaneous arbitrary couplings α and β in addition to g^*. We note that earlier analytical descriptions of SdH magnetoresistivity oscillations considered particular cases, namely, when either only one of the parameters α, β or g^* was nonzero or any two of these parameters were nonzero, with the exceptions $(\alpha \neq \beta \neq 0,\ g^* = 0)$ and $(\alpha = \beta,\ g^* \neq 0)$.

Interestingly, our analytical formula generalizes previous results[44] for $g^* = 0$ and predicts a new condition for the vanishing of the SdH magneto-oscillation beatings in all harmonics [e.g., Figs. 1(c)] in Rashba-Dresselhaus coupled 2DEGs with substantial Zeeman splittings, namely,

$$\frac{\alpha}{\beta} = \sqrt{\frac{1 - \tilde{\Delta}}{1 + \tilde{\Delta}}}, \tag{1}$$

where $\tilde{\Delta}$ is a material parameter given by the ratio between the Zeeman splitting and the Landau-level spacing. As we discuss later on, Eq. (1) *is not* associated with a conserved quantity in our system; this contrasts with the persistent-spin-helix condition $\alpha = \beta$, which predicts spin conservation along particular axes[5–7]. We stress that this case with $\alpha = \beta$ and generic $g^* \neq 0$ leads to beating in the frequency spectrum of our system, Figs. 1(d), as opposed to our new condition in Eq. 1. As we discuss below, our numerical and analytical approaches show excellent agreement with available data from Refs. 41 and 46.

Our approach combines a semiclassical formulation for the resistivity of 2DEGs with a trace formula for the density of states (DOS) in a quantizing magnetic field. The trace formula expresses the DOS using the usual Poisson summation formula[47]. This formulation brings out the oscillatory part of the DOS, thus allowing us to clearly identify the higher harmonics of the SdH oscillations. It enables us to conveniently separate the frequency scales into "fast" and "slow" oscillations thus allowing for a clearer interpretation of the underlying physical phenomena, e.g., the slow beating SdH oscillations due to the SO coupling.

Our main results for the oscillatory part of magnetoresistivity $\delta\rho_{xx}(1/B)$ and its frequency spectra $I(f)$ [panel insets] are show in Fig. 1. For pure Rashba [$\alpha \neq 0$, $\beta = 0$, Fig. 1a)] and pure Dresselhaus [$\alpha = 0$, $\beta \neq 0$, Fig. 1b)], but non-zero Zeeman term ($g^* \neq 0$), the frequency spectra, as usual, show two main peaks, which correspond to the first two Fourier components of $\delta\rho_{xx}(1/B)$. These two cases, however, exhibit a marked contrast: while the pure Rashba shows a peak splitting at the fundamental frequency, the pure Dresselhaus exhibits a peak splitting in the second harmonic. As we explain in detail in Sec. V D, this contrasting behavior arises from the interplay between the Zeeman and SO interactions, which makes the SdH magneto-responses with *nonzero* g-factors g^* inequivalent for Rashba-dominated ($\alpha > \beta$) vs. Dresselhaus-dominated ($\alpha < \beta$) 2DEGs. For $g^* = 0$, the pure Rashba and pure Dresselhaus cases give identical

results.

Figure 1(c) illustrates our prediction in Eq. (1) thus showing no peak splitting in the frequency spectra – at any harmonic – when this condition is satisfied. To emphasize this condition emulates a situation with no SO coupling (i.e., no beating), we plot in Fig. 1(c) the $\alpha = \beta = 0$ (with $g^* \neq 0$) case [dashed curve in 1(c)], which shows complete overlap with the case satisfying Eq. (1). In contrast and for completeness, Fig. 1d) shows the $\alpha = \beta \neq 0$ case with $g^* \neq 0$, which exhibits peak splitting in the *second* harmonic.

We have applied our analytical description to low-density GaAs-based quantum wells for which there are experimental data[46] showing several harmonics in the SdH magneto-oscillations. Figure 2 shows the excellent agreement obtained, thus illustrating that our semiclassical formulas can satisfactorily capture the higher harmonics of the SdH oscillations. Moreover, we have applied our analytical approach to low-density InSb-based 2DEGs[15,39] where, unlike GaAs-based 2DEGs, a strong SO coupling manifests itself as beatings in the measured SdH oscillations, and find good agreement. We have also implemented a detailed numerical calculation for high-density InAs-based 2DEGs for which an analytical description is not adequate. Here again we find very good agreement with available data[41] and are able to extract SO coupling parameters.

Next (Sec II), we present a description of the Hamiltonian of our system. In Sec. III we discuss how to obtain the "F–function", the central quantity in our formulation, from the Landau-quantized energy spectrum of our system and its connection with the density of states (DOS). The formalism for obtaining the Shubnikov-de Haas oscillations in terms of the Poisson summation formula and the F-function is described in Sec. IV. Finally, in Sec. V we present and analyze different particular cases of SdH oscillations and, more important, derive the new condition in Eq. (1) for the complete absence of beatings (all harmonics) in the SdH oscillations, for 2DEGs with non-zero Rashba, Dresselhaus, and Zeeman couplings. The appendices present relevant details of our theoretical formulation.

II. 2DEG HAMILTONIAN

Our starting point is the Hamiltonian for a 2DEG confined in a quantum well (xy plane) grown along the [001] crystallographic direction, taken as z axis. In the presence of a perpendicular external magnetic field $\mathbf{B} = (0, 0, B)$ and both Rashba[48] and Dresselhaus[49] spin orbit interactions, the Hamiltonian reads

$$\mathcal{H} = \frac{1}{2m^*}\left(\Pi_x^2 + \Pi_y^2\right) + \frac{1}{2}g^*\mu_B B\sigma_z$$
$$+ \frac{\alpha}{\hbar}\left(\Pi_x\sigma_y - \Pi_y\sigma_x\right) + \frac{\beta}{\hbar}\left(\Pi_x\sigma_x - \Pi_y\sigma_y\right), \quad (2)$$

where g^* is the g-factor, m^* is effective mass, $\mathbf{\Pi} = \mathbf{p} - q\mathbf{A}$ is the canonical momentum, q is the electric charge, μ_B is the Bohr magneton, $\hbar$ the reduced Planck's constant and σ_x, σ_y, σ_z denote the usual Pauli matrices. The parameters α and β denote the linear-in-k Rashba and Dresselhaus SO couplings, respectively. The β coupling includes a density dependent correction arising from the cubic Dresselhaus term. As we discuss later on [Sec. VI A], our numerical results will account for the full cubic Dresselhaus term.

Let us introduce the annihilation and creation operators associated to the Landau level $|n\rangle$

$$a = \frac{\ell_c}{\sqrt{2}\hbar}\left(\Pi_x - i\zeta\Pi_y\right), \quad (3)$$

$$a^\dagger = \frac{\ell_c}{\sqrt{2}\hbar}\left(\Pi_x + i\zeta\Pi_y\right), \quad (4)$$

obeying $\left[a, a^\dagger\right] = 1$, $a|n\rangle = \sqrt{n}|n-1\rangle$, $a^\dagger|n\rangle = \sqrt{n+1}|n+1\rangle$, $\zeta = -\text{sign}(qB)$, with the magnetic length and the center of the Landau orbit denoted by $\ell_c = \sqrt{\frac{\hbar}{|qB|}}$ and $y_0 = \frac{ek_x}{|qB|}$, respectively. In this work, we have $q = -e$, where $e > 0$ is the absolute value of the elementary electronic charge, and we choose $B > 0$, yielding $\zeta = 1$. Using Eqs. (3) and (4), our Hamiltonian [Eq. (2)] becomes

$$\mathcal{H} = \hbar\omega_c(a^\dagger a + 1/2) + \frac{\Delta}{2}\sigma_z - \frac{i\alpha}{\sqrt{2}\ell_c}(a^\dagger\sigma_- - a\sigma_+)$$
$$+ \frac{\beta}{\sqrt{2}\ell_c}(a^\dagger\sigma_+ + a\sigma_-), \quad (5)$$

where the cyclotron frequency is $\omega_c = eB/m^*$, $\Delta = g^*\mu_B B$, which inherits its sign from g^*, and $\sigma_\pm = \sigma_x \pm i\sigma_y$, with σ_x and σ_y denoting Pauli matrices. We now perform the canonical transformation $\tilde{\mathcal{H}} = \mathcal{U}\mathcal{H}\mathcal{U}^\dagger$ with $\mathcal{U} = e^{-i\frac{\pi}{4}\left(\frac{\sigma_z}{2} + a^\dagger a\right)}$, which yields

$$\mathcal{U}\sigma_\pm\mathcal{U}^\dagger = \sigma_\pm e^{\mp i\frac{\pi}{4}}, \quad (6)$$
$$\mathcal{U}\sigma_z\mathcal{U}^\dagger = \sigma_z, \quad (7)$$
$$\mathcal{U}a^\dagger\mathcal{U}^\dagger = e^{i\frac{\pi}{4}}a^\dagger, \quad (8)$$

and finally

$$\frac{\tilde{\mathcal{H}}}{\hbar\omega_c} = (a^\dagger a + 1/2) + \frac{\tilde{\Delta}}{2}\sigma_z + \alpha_B(a^\dagger\sigma_- + a\sigma_+)$$
$$+ \beta_B(a^\dagger\sigma_+ + a\sigma_-), \quad (9)$$

where we have introduced the real valued, dimensionless quantities $\alpha_B = \frac{\alpha}{\sqrt{2}\hbar\omega_c\ell_c}$, $\beta_B = \frac{\beta}{\sqrt{2}\hbar\omega_c\ell_c}$ and $\tilde{\Delta} = \frac{\Delta}{\hbar\omega_c} = \frac{g^*m^*}{2m_0}$.

Analytical solutions for the above Hamiltonian [Eq. (9)] can be found for the cases with either pure Rashba or pure Dresselhaus[48,50]. The specific cases of $\alpha = \pm\beta$ turn out to be of great physical interest, where persistent spin helix (PSH)[5,6,46] and persistent Skyrmion lattice (PSL)[7] were predicted. Interestingly, the case

with $\alpha = \pm\beta$ maps to the Rabi model in quantum optics and was recently solved exactly[51]. The exact solution relies on obtaining zeros of a transcendental function. Moreover, previous studies of the Rabi model have important implications for our system. For instance, we have shown that the Rabi parity symmetry[51,52] remains valid in our problem for arbitrary α and β (See Appendix B). This enables us to separate the Hilbert space in two subspaces with different parities, which can be individually analyzed and compared. As for general couplings α and β, similar systems have been studied before in the framework of Landau levels, using either variational (Hartree-Fock) methods[53], second order perturbation[54,55] or obtaining the spectrum in terms of solutions of transcendental equations[56]. A perturbation scheme based on 4th order Schrieffer-Wolff transformation has also been used to find approximate analytical solutions[57]. However, we are unaware of any exact analytical solution for general Rashba, Dresselhaus and Zeeman coupling.

III. F-FUNCTION AND ITS CONNECTION WITH THE ENERGY SPECTRUM AND DOS

For our 2DEG in the presence of perpendicular magnetic field, the low magnetic field regime corresponds to having a very large number of Landau levels below the Fermi energy ε_F (taken as constant and equal to its zero-field value), i.e., many occupied states. The system is thus assumed to be far away from the integer quantum Hall regime where few Landau levels are occupied and the effects of electron-electron interaction become important[33]. Let us denote the eigenenergies of our *dimensionless* Hamiltonian Eq. (9) by $\varepsilon_{n,s}$, where $n \in \mathbb{N}_0$ represents the LL number and $s = \pm$ represents a pseudo-spin associated to the presence of two spin-split bands (due to the Zeemann and SO interactions). With this notation, the density of states (DOS) reads

$$\mathcal{D}(\varepsilon, B) = \frac{\tilde{D}}{A} \sum_{n,s} \delta(\varepsilon - \hbar\omega_c \varepsilon_{n,s}), \qquad (10)$$

where $\tilde{D} = A/2\pi\ell_c^2$ is the LL degeneracy and A the 2DEG area. This LL degeneracy is the same for all 2DEGs studied here in the presence or absence of Zeemann and SO interactions.

As we show in the next section, the magnetotransport properties of the system can be determined by the Landau levels sequentially crossing ε_F. The rate at which these crossings happen will determine a periodic behavior of the magnetotransport properties of the system as the magnetic field is varied. In order to describe this periodicity, we introduce the F-function[33] (see Appendix A for details), which is defined by the relation

$$\varepsilon_{n,s}(B) = \varepsilon \leftrightarrow n = F_s(\varepsilon, B). \qquad (11)$$

The F-function gives the Landau level index n of the

state that has energy ε and pseudo-spin s at magnetic field B.[47,58] It is important to notice that the equation for n [Eq. (11)] can also return non-integer values for n. In such cases the F-function provides a measure of how close a Landau level n is to the energy ε, for a given pseudo-spin s and magnetic field B.

Since one can relate transport phenomena with the density of states, we rewrite the DOS of our system in a way that highlights its oscillatory behavior dependence on both α and β. First we introduce the F_s function into Eq. (10)

$$\mathcal{D}(\varepsilon, B) \approx \frac{m^*}{2\pi\hbar^2} \sum_{n,s} \delta(n - F_s(\varepsilon/\hbar\omega_c, B)), \qquad (12)$$

which neglects terms $\mathcal{O}[(\alpha m^*\ell_c)^2/\hbar] + \mathcal{O}[(\beta m^*\ell_c)^2/\hbar]$. This holds for typical values of α, β, m^* and small magnetic fields $B \lesssim 1$T. Using the Poisson summation formula $\sum_{n=0}^{\infty} \delta(n - F_s) = 1 + 2\sum_{l=1}^{\infty} \cos(2\pi l F_s)$ and defining the relevant quantities

$$\mathcal{F}_{\pm} = \frac{1}{2}(F_+ \pm F_-), \qquad (13)$$

we obtain

$$\frac{\mathcal{D}(\varepsilon, B) - 2\mathcal{D}_0}{2\mathcal{D}_0} \approx 2\sum_{l=1}^{\infty} \cos(2\pi l\mathcal{F}_+)\cos(2\pi l\mathcal{F}_-), \quad (14)$$

where $\mathcal{D}_0 = \frac{m^*}{2\pi\hbar^2}$ is the (constant) density of states per spin for the 2DEG at zero magnetic field (see Appendix A for details). As we are going to see later, $\mathcal{F}_+$ contains the fast oscillations with respect to $1/B$, which is is proportional to the electron density n_{2D}. On the other hand, $\mathcal{F}_-$ contains the slow oscillations that are determined by the spin-orbit coupling terms, α and β. Moreover, the fast oscillations arising from the terms with $l > 1$ correspond to the higher harmonics, and have be seen in experiments[46].

IV. SDH OSCILLATIONS IN THE MAGNETORESISITIVITY

As already mentioned, the oscillations in the magnetoresistivity as a function of the magnetic field are called SdH oscillations[33]. They appear as a consequence of the sequential depopulation of the LLs when the magnetic field is increased. For low magnetic fields where multiple LL are occupied, i.e., far from the integer quantum Hall regime[33], a semi-classical description of the magneto-oscillations can be used.

In experiments, the measurement of the SdH oscillations is accessed via the longitudinal differential resistivity. In general, the resistivity tensor is defined as the

inverse matrix of the conductivity tensor,

$$\boldsymbol{\rho} = \begin{pmatrix} \sigma_{xx} & \sigma_{xy} \\ \sigma_{xy} & \sigma_{xx} \end{pmatrix}^{-1}. \tag{15}$$

The relevant magnetoresistivity component for us is

$$\rho_{xx} = \frac{\sigma_{xx}}{\sigma_{xx}^2 + \sigma_{xy}^2}, \tag{16}$$

where

$$\sigma_{xx(xy)}(B,T) = \int d\varepsilon \left(-\frac{df_0(\varepsilon)}{d\varepsilon}\right) \sigma_{xx(xy)}(B,\varepsilon,T=0), \tag{17}$$

where $f_0(\varepsilon)$ is the Fermi-Dirac distribution. Using a semi-classical approach, we account for the magnetic field dependence of the conductivity via the electron scattering time $\tau(\varepsilon, B)$, which is proportional to the DOS $\mathcal{D}(\varepsilon, B)$ via Fermi's golden rule. Accordingly, up to linear order on the deviation of the DOS, we obtain

$$\tau(\varepsilon, B) \approx \tau_0(\varepsilon) \left[1 - \frac{\mathcal{D}(\varepsilon,B) - \mathcal{D}_0(\varepsilon)}{\mathcal{D}_0(\varepsilon)}\right], \tag{18}$$

with $\mathcal{D}_0(\varepsilon) = \mathcal{D}(\varepsilon, B=0)$ and $\tau_0(\varepsilon) = \tau(\varepsilon, B=0)$. Using the Drude semi-classical equations for the frequency-independent current[33], the normalized longitudinal resistivity reads

$$\delta\rho_{xx}(B) = \frac{\rho_{xx}(B) - \rho_{xx}(B=0)}{\rho_{xx}(B=0)} \tag{19}$$

$$= \int d\varepsilon \left(-\frac{df_0(\varepsilon)}{d\varepsilon}\right) \frac{\mathcal{D}(\varepsilon,B) - \mathcal{D}_0(\varepsilon)}{\mathcal{D}_0(\varepsilon)}. \tag{20}$$

For the DOS in the presence of Landau level broadening due to scattering processes, the relation in Eq. (10) is replaced by

$$\mathcal{D}(\varepsilon, B) = \frac{\tilde{D}}{A} \sum_{n,s} L_\Gamma(\varepsilon - \hbar\omega_c \varepsilon_{n,s}), \tag{21}$$

where $L_\Gamma(x)$ describes the broadening function, e.g., Lorentzian or Gaussian, and Γ is parameter defining the broadening of the levels (see Appendix A for details). After applying the Poisson summation formula, we obtain a result that resembles Eq. (14), apart from the appearance of the the the cosine Fourier transform of $L_\Gamma(x)$, denoted with $\tilde{L}_\Gamma(x)$,

$$\frac{\mathcal{D}(\varepsilon,B) - \mathcal{D}_0(\varepsilon)}{\mathcal{D}_0(\varepsilon)} \approx 2\sum_{l=1}^{\infty} \tilde{L}_\Gamma\left(l\frac{\Gamma}{\hbar\omega_c}\right)\cos(2\pi l \mathcal{F}_-)\cos(2\pi l \mathcal{F}_+). \tag{22}$$

The so-called Dingle factor $\tilde{L}_\Gamma(x)$[33] sets the limit of validity of the semi-classical approximation, i.e., that the oscillatory part of the resistivity should be much smaller than the constant term. It also gives the regime where it is valid to consider only the lowest harmonic.

Higher harmonics have been observed in magnetoresistivity measurements[46] in GaAs-based 2DEGs. The $\mathcal{F}_-$ function can be related to the envelope of the SdH oscillations. The general form of the temperature-dependent normalized resistivitity reads

$$\delta\rho_{xx}(B,T) = 2\sum_{l=1}^{\infty} \int d\varepsilon \tilde{L}_\Gamma\left(l\frac{\Gamma}{\hbar\omega_c}\right)\left(-\frac{df_0(\varepsilon,T)}{d\varepsilon}\right) \tag{23}$$

$$\times \cos(2\pi l \mathcal{F}_-)\cos(2\pi l \mathcal{F}_+).$$

Even though we only consider the zero-temperature limit in the present work, for completeness, below we present the temperature-dependence of $\delta\rho_{xx}(B,T)$ valid in the relevant parameter range considered in this work and for all the systems studied here. As show in Appendix G, we find

$$\delta\rho_{xx}(B,T) \approx 2\sum_{l=1}^{\infty} \tilde{L}_\Gamma\left(l\frac{\Gamma}{\hbar\omega_c}\right)\mathcal{A}_l(T)$$

$$\times \cos(2\pi l \mathcal{F}_-)\cos(2\pi l \mathcal{F}_+)|_{\varepsilon=\varepsilon_F}, \tag{24}$$

where the temperature-dependent coefficient

$$\mathcal{A}_l(T) = \frac{2\pi^2 l k_B T/\hbar\omega_c}{\sinh\left(2\pi^2 l k_B T/\hbar\omega_c\right)} \tag{25}$$

accounts for the temperature dependence of the SdH oscillations. In the limit of vanishing α and β this reduces to the result in Ref. 59, and in the case of *both* vanishing β and broadening ($\Gamma = 0$) gives the result in Ref. 50 [Eq. (9.28)]. Here we assume that ε is close to the zero magnetic field Fermi energy $\varepsilon_F = \hbar^2 k_F^2/2m$.

A widely used method to extract spin-orbit couplings and electronic densities is to analyze the oscillations by calculating the quantity

$$I(f) = \left|\int_{B_2^{-1}}^{B_1^{-1}} d\left(\frac{1}{B}\right) \frac{\rho_{xx}(B) - \rho_{xx}(B_1)}{\rho_{xx}(B_1)} e^{i2\pi f/B}\right|^2, \tag{26}$$

which defines the power spectrum of the normalized magneto-resistivity with a trivial background value $\rho_{xx}(B = B_1)$ removed. Note that B_1 should be small enough such that the semiclassical regime of a constant $\rho_{xx}(B \to 0)$ is reached.

In Fig. 2 the power spectrum is shown for data from Fig. S11a in Ref. 46, where magnetoresistivity SdH oscillations were measured in a GaAs 2DEG over a magnetic field interval $[0.20, 1.5]$ T. The power spectrum shows a SdH peak at $f \approx 10.5$ T (the fundamental frequency), and higher harmonics are clearly visible at 21.0 T and 31.5 T, corresponding to the first and second harmonic, respectively. The experimental data was fitted with Eq. (30) with one fit parameter: τ_q. The resulting fit matches very well the harmonics of the SdH signal. To acccount for the small background shift in the experimental data as seen in the inset a more elaborate modeling of the data
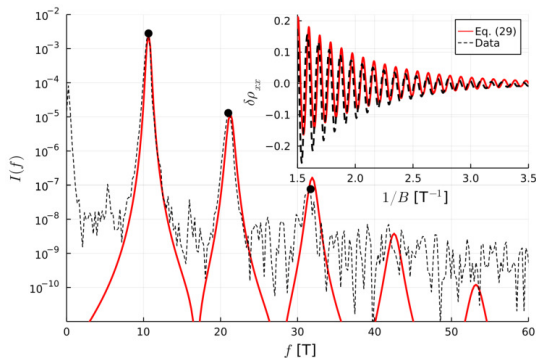
FIG. 2. The power spectrum $I(f)$ for $\delta\rho_{xx}$ measurements on a GaAs 2DEG in Ref. 46 obtained using Eq. (26). The calculated results used Eq. (30) with one fitting parameter: τ_q. The inset shows the magneto-resistivity data and the corresponding calculated $\delta\rho_{xx}$.

FIG. 3. Landau levels $n = 4$, 5 [Eq. (27)] as a function of $1/B$ for a 2DEG with only Zeeman interaction and no SO couplings ($\alpha = \beta = 0$). The dotted line shows $\varepsilon_F/\hbar\omega_c$. Here, we use $m^* = 0.019m_o$, $g^* = -34$ and $n_{2D} = 3.3 \times 10^{-3}\,\mathrm{nm}^{-2}$ for InSb-based wells[15,39].

would be required. The fitting was done using six harmonics, and resulted in $\tau_q = 0.8\,\mathrm{ps}$, using standard GaAs parameters $m = 0.067m_0$ and $g^* = -0.44$. Note that we have used Eq.(30), which does not include SO coupling, for our fitting procedure here. This is justifiable because GaAs-based 2DEGs have relatively small SO couplings, not accessible via SdH measurements. Weak antilocalization measurements can access the SO parameter in these systems[41]. However, GaAs-based 2DEGs have relatively high mobilities thus making it possible to see many harmonics.

V. RESULTS AND DISCUSSIONS

In this section we present the energy spectrum, F–function and magnetoresistivity SdH oscillations for different parameter regimes of our Hamiltonian, Eq. (9). Additionally, we discuss in detail the interpretation of the SdH oscillations within the trace formula description (e.g., contribution of higher harmonics) and show how to extract relevant spin-orbit couplings from it. The results are presented in order of simplicity, i.e., from the simplest to the more complex case.

A. Landau levels with only Zeeman interaction

In the presence of Zeeman and no Rashba and Dresselhaus SO couplings, i.e., $\alpha = \beta = 0$, the eigenenergies of our Hamiltonian [Eq. (9)] are given by

$$\frac{\varepsilon_{n,s}}{\hbar\omega_c} = n + \frac{1}{2} + \frac{\tilde{\Delta}}{2}s. \qquad (27)$$

with $n \in \mathbb{N}_0$ and $s = 1$ ($s = -1$) representing the pure spin state $|\uparrow\rangle$ ($|\downarrow\rangle$). In Fig. 3 we plot the four energy levels corresponding to $n = 4,5$ and $s = \pm1$, along with $\varepsilon_F/\hbar\omega_c$, using the following InSb QW parameters from Refs. 15 and 39: $m^* = 0.019m_o$, $g^* = -34$ and electron density $n_{2D} = 3.3 \times 10^{-3}\,\mathrm{nm}^{-2}$. For these parameters, the ordering of the energies obeys $\varepsilon_{n+1,-1} > \varepsilon_{n+1,1} > \varepsilon_{n,-1} > \varepsilon_{n,1}$. Figure 3 shows how successive levels cross the Fermi energy as a function of the magnetic field. This, in turn, will reflect on the oscillations of the resistivity once for $\varepsilon_F \approx \varepsilon_{n,s}$, an increase on the conductivity will happen due to the resonance condition between the corresponding LL and the Fermi energy.

From the energy expressions above [Eq. (27)], we can obtain the F–functions through Eq. (11), namely,

$$F_s(\varepsilon) = \frac{\varepsilon}{\hbar\omega_c} - \frac{\tilde{\Delta}}{2}s - \frac{1}{2}, \text{ with } \frac{dF_s(\varepsilon)}{d\varepsilon} = \frac{1}{\hbar\omega_c}, \qquad (28)$$

yielding the fast and slow components [Eq. (13)]

$$\mathcal{F}_+(\varepsilon,B) = \frac{\varepsilon}{\hbar\omega_c} - \frac{1}{2}, \qquad \mathcal{F}_-(\varepsilon,B) = -\frac{\tilde{\Delta}}{2}. \qquad (29)$$

At $\varepsilon = \varepsilon_F$ these can be expressed (to a very good approximation) as $\mathcal{F}_+ = \frac{hn_{2D}}{2e}\frac{1}{B} - \frac{1}{2}$ and $\mathcal{F}_- = -\frac{g}{4}\frac{m^*}{m_0}$, where we assume that $n_{2D} = \frac{k_F^2}{2\pi}$ is the 2DEG electron density at $B = 0$.

The corresponding resistivity can now be determined through Eq. (22) and reads

$$\delta\rho_{xx}(B) = 2 \sum_{l=1}^{\infty} e^{-l\pi \frac{\hbar/\tau_q}{\hbar\omega_c}} \frac{2\pi^2 l k_B T/\hbar\omega_c}{\sinh\left(2\pi^2 l k_B T/\hbar\omega_c\right)} \cos\left[2\pi l \left(\frac{f^{\mathrm{SdH}}}{B} - \frac{1}{2}\right)\right] \cos\left(\pi l g^* \frac{m^*}{m_0}\right), \tag{30}$$

where $f^{\mathrm{SdH}} = \frac{h n_{2D}}{2e}$ and we have assumed a Lorentzian form for the L_Γ broadening. For small magnetic fields, both effective mass and g-factor nominal values do not depend on the magnetic field[60]. As a result, the $1/B$-dependence of the resistivity in a 2DEG with only Zeeman coupling, displays oscillations with frequencies multiple of f^{SdH}, and absence of beating. This can be seen from Fig. 4, where we plot $\delta\rho_{xx}(B)$ vs $1/B$ for the harmonics $l = 1, 2, 3$ and clearly see oscillations with the respective frequencies $f^{\mathrm{SdH}}, 2f^{\mathrm{SdH}}$, and $3f^{\mathrm{SdH}}$. The solid (dotted) curves correspond to $g^* = -34$ and $m^* = 0.019m_o$ ($g^* = 0$ and $m^* = 0.019m_o$)[15,39]. Note that the higher harmonics have smaller resistivity amplitudes. This occurs due to the Dingle factor $\propto e^{-l/B}$, which suppresses the higher harmonic components.

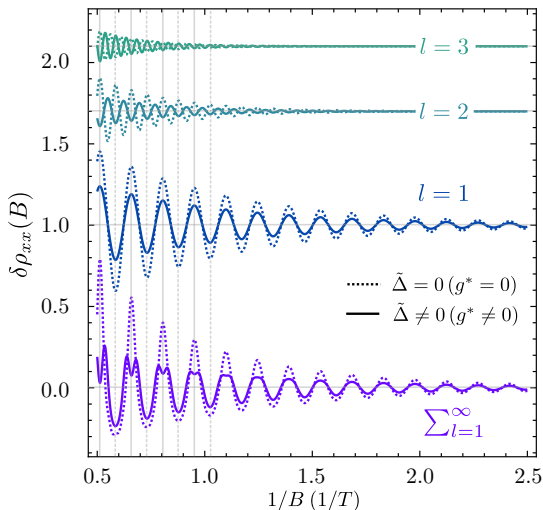FIG. 4. Magnetoresistivity deviation $\delta\rho_{xx}(B)$ as a function of $1/B$ for a 2DEG with only Zeeman coupling and no SO couplings. The lowest curve corresponds to $\delta\rho_{xx}(B)$ and the curves labelled by l are the individual frequency components in Eq. (30). The solid (dashed) line corresponds to $g^* = -34$ ($g^* = 0$), $m^* = 0.019m_o$ and $n_{2D} = 3.3 \times 10^{-3}\,\mathrm{nm}^{-2}$. These parameters are for InSb-based wells [15,39].

We should stress that the effects of the Zeeman coupling within the plot of $\delta\rho_{xx}(B)$ are not immediately obvious. For instance, it can be seen that for $g^* = 0$ and $g^* \neq 0$, the corresponding $\delta\rho_{xx}^{l=1}(B)$ (blue curves depicting the first harmonic) only differ from themselves by the amplitude of the oscillation. For $\tilde{\Delta} = -0.323$, $\cos(2\pi\tilde{\Delta}/2)$ is smaller than one, thus yielding a reduction of the total amplitude for $g^* \neq 0$ as compared to

$g = 0$. As a consequence, the presence of Zeeman is not readily evident from the oscillations of $\delta\rho_{xx}^{l=1}(B)$. Conversely, the Zeeman is only manifested within the resistivity when one considers many harmonics, as we discuss below.

The definition of DOS in Eq. (21) gives broadened Landau levels separated by $\hbar\omega_c$, which are in turn spin split by the Zeeman term $\tilde{\Delta}$ [See Eq. (27) and Fig. 3]. This spin splitting can only be seen in the resistivity [Eq. (30)] when the contributions from the first *and* second harmonics, $\cos(2\pi f^{\mathrm{SdH}}/B - \pi)\cos(2\pi\tilde{\Delta}/2)$ and $\cos(4\pi f^{\mathrm{SdH}}/B - 2\pi)\cos(4\pi\tilde{\Delta}/2)$, respectively, have opposite signs. For the parameters of Fig. 3 $\tilde{\Delta} = -0.323$ the Zeeman term significantly affects the maximum of the resistivity. This can be seen in Fig. 4, where the resistivities associated to harmonics $l = 1$ and $l = 2$ (blue and cyan solid curves, respectively), interfere in a destructive way, producing the double-peak feature in the total resistivity (purple solid lines), characteristic of the incipient spin splitting in such data. We emphasize, however, that this feature can be absent depending on the broadening of the energy levels (due to the overlap of the spin-split levels). This is the reason why the double-peak feature is not seen on the other maximum peaks.

Although the g^*-factor term does not depend explicitly on magnetic field, it can manifest itself in the magneto-oscillations. More specifically, Zeeman-only effects can have a pronounced effect on the magneto-oscillations, controlling the amplitude and sign of how subsequent harmonics are added, either constructively or destructively, before being damped by the quantum life time. Furthermore, it is important to say that the Zeeman can give rise to interesting features and affect drastically the understanding of the magneto-oscillations. For instance, if one could engineer a material[61] such that $\tilde{\Delta} = \frac{g^*}{2}\frac{m^*}{m_0} = 0.5 + m$ with $m \in \mathbb{Z}$, then the main weight of the resistivity would be due to the second harmonic with SdH frequently $2f^{\mathrm{SdH}}$ as $\cos(l\pi\tilde{\Delta}) = 0$ for $l = 1$.

B. Landau Levels with Zeeman and Rashba interactions

We now analyze the case where we have the presence of both Zeeman and Rashba terms, i.e., $\tilde{\Delta} \neq 0$, $\alpha \neq 0$ and no Dresselhaus coupling $\beta = 0$ in Eq. (9). In the spin basis $\{|\uparrow\rangle, |\downarrow\rangle\}$, the corresponding Hamiltonian assumes the following matrix form

$$\frac{\tilde{\mathcal{H}}}{\hbar\omega_c} = \begin{pmatrix} a^\dagger a + \frac{1}{2} + \frac{\tilde{\Delta}}{2} & 2\alpha_B a \\ 2\alpha_B a^\dagger & a^\dagger a + \frac{1}{2} - \frac{\tilde{\Delta}}{2} \end{pmatrix}. \tag{31}$$

TABLE I. Definitions of the Zeeman and SO-related quantities used is this work.

Zeeman (g^*)	$\omega_c = \frac{eB}{m^*}$	$\ell_c = \sqrt{\frac{\hbar}{eB}}$	$\Delta = g^* \mu_B B$	$\tilde{\Delta} = \frac{\Delta}{\hbar\omega_c} = \frac{g^* m^*}{2m_0}$
Rashba (α)	$\varepsilon_R = \frac{\alpha^2 m^*}{2\hbar^2} = \frac{\hbar^2 k_R^2}{2m^*}$	$\alpha_B = \frac{\alpha}{\sqrt{2}\hbar\omega_c\ell_c}$	$\frac{\varepsilon_R}{\hbar\omega_c} = \alpha_B^2$	
Dresselhaus (β)	$\varepsilon_D = \frac{\beta^2 m^*}{2\hbar^2} = \frac{\hbar^2 k_D^2}{2m^*}$	$\beta_B = \frac{\beta}{\sqrt{2}\hbar\omega_c\ell_c}$	$\frac{\varepsilon_D}{\hbar\omega_c} = \beta_B^2$	
SO parameters	$\gamma = \alpha_B + \beta_B$	$\delta = \alpha_B - \beta_B$	$\Omega = \frac{2\varepsilon_R/\hbar\omega_c}{1-\tilde{\Delta}} + \frac{2\varepsilon_D/\hbar\omega_c}{1+\tilde{\Delta}}$	$\Lambda = \frac{2\varepsilon_R/\hbar\omega_c}{1-\tilde{\Delta}} - \frac{2\varepsilon_D/\hbar\omega_c}{1+\tilde{\Delta}}$

Interestingly, the operator $\mathcal{N}_+ = a^\dagger a + \sigma_z/2$ commutes with the Hamiltonian above, i.e., $[\tilde{\mathcal{H}}, \mathcal{N}_+] = 0$, and hence $\tilde{\mathcal{H}}$ and $\mathcal{N}_+$ share the same eigenstates. Hence we have $\mathcal{N}_+ |n,\uparrow\rangle = (n+1/2)|n,\uparrow\rangle$ and $\mathcal{N}_+ |n+1,\downarrow\rangle = (n+1/2)|n+1,\downarrow\rangle$, i.e., for $n \in \mathbb{N}$, $|n,\uparrow\rangle$ and $|n+1,\downarrow\rangle$ are degenerate with respect to the operator $\mathcal{N}_+$, except for $|0,\downarrow\rangle$ with corresponding energy $\frac{\varepsilon_{0,\downarrow}}{\hbar\omega_c} = \frac{1}{2}(1-\tilde{\Delta})$. As a consequence, a linear combination of $|n,\uparrow\rangle$ and $|n+1,\downarrow\rangle$ is also an eigenstate of our Hamiltonian Eq. (31). This motivates us to rewrite the total Hamiltonian as a direct sum of 2×2 block Hamiltonians in the basis $\{|n,\uparrow\rangle, |n+1,\downarrow\rangle\}$($\tilde{\mathcal{H}}_{|n,\uparrow\rangle;|n+1,\downarrow\rangle}$), in addition to the non-degenerate decoupled Hamiltonian ($\tilde{\mathcal{H}}_{|0,\downarrow\rangle}$), namely

$$\tilde{\mathcal{H}} = \tilde{\mathcal{H}}_{|0,\downarrow\rangle} \oplus \bigoplus_{n=0}^{\infty} \tilde{\mathcal{H}}_{|n,\uparrow\rangle;|n+1,\downarrow\rangle}, \qquad (32)$$

with $\tilde{\mathcal{H}}_{|0,\downarrow\rangle} = \varepsilon_{0,\downarrow}$ and

$$\tilde{\mathcal{H}}_{|n,\uparrow\rangle;|n+1,\downarrow\rangle} = \hbar\omega_c \begin{pmatrix} n + \frac{1}{2} + \frac{\tilde{\Delta}}{2} & 2\alpha_B\sqrt{n+1} \\ 2\alpha_B\sqrt{n+1} & n + 1 + \frac{1}{2} - \frac{\tilde{\Delta}}{2} \end{pmatrix}. \qquad (33)$$

The diagonalization of the Hamiltonian Eq. (33) yields energies

$$\frac{\varepsilon_{n,s}}{\hbar\omega_c} = \left(n + \frac{1}{2} + \frac{s}{2}\right) \qquad (34)$$
$$- \frac{s}{2}\frac{1-\tilde{\Delta}}{|1-\tilde{\Delta}|}\sqrt{\left(1-\tilde{\Delta}\right)^2 + 16\alpha_B^2\left(n + \frac{1}{2} + \frac{s}{2}\right)},$$

with $s = \pm$ and $n \in \mathbb{N}_0$, which already incorporates the energy of the decoupled state $|0,\downarrow\rangle$, $\varepsilon_{0,-} \equiv \varepsilon_{0,\downarrow}$ ($\varepsilon_{0,+} \equiv \varepsilon_{0,\downarrow}$) if $1 - \tilde{\Delta} > 0$ ($1 - \tilde{\Delta} < 0$). These LLs are plotted in Fig. 5 as a function of $1/B$ for parameters $\alpha = 10\,\text{meV nm}$, $m^* = 0.019 m_o$ and $g^* = -34$ [15,39]. Due to the spin-orbit coupling, the energy levels $\frac{\varepsilon_{l,s}}{\hbar\omega_c}$ are no longer equidistant, and their separation changes as function of $1/B$. On this scale, the energy dispersion appears linear in $1/B$. In fact, for $\tilde{\Delta} < 0$ ($\tilde{\Delta} > 0$) the spin-splitting is enhanced (suppresses) relative to the case with $\alpha = 0$ (See Fig. 3). This can be seen through the expansion of the term $(1-\tilde{\Delta})^2$ within the square root of Eq. (34), yielding $-2\tilde{\Delta}$, which enhances the Zeeman splitting in the presence of Rashba SO coupling.[39]

Accordingly, for this case we obtain

$$\mathcal{F}_+(\varepsilon, B) = \frac{\varepsilon}{\hbar\omega_c} - \frac{1}{2} + 2\alpha_B^2, \qquad (35)$$

$$\mathcal{F}_-(\varepsilon, B) = -\frac{1}{2} + \frac{1}{2}\frac{1-\tilde{\Delta}}{|1-\tilde{\Delta}|}\sqrt{(1-\tilde{\Delta})^2 + 16\alpha_B^2\left(\alpha_B^2 + \frac{\varepsilon}{\hbar\omega_c}\right)} \qquad (36)$$

Differently from the results in the previous section, here both $\mathcal{F}_\pm$ functions depend on the magnetic field. As a consequence, we will have more complex oscillations in

$\rho_{xx}(B)$ as compared to the case without Rashba coupling [Fig. 4].

In Fig. 6, we plot the total differential magnetoresistivity $\delta\rho_{xx}(B)$, and the independent contributions from harmonics $l = 1,2$ and $l = 3$. Here we use $\alpha = 10\,\text{meV nm}$, $m^* = 0.019 m_o$, $g^* = -34$ and $n_{2D} = 3.3 \times 10^{-3}\,\text{nm}^{-2}$ [15,39]. Similarly to the case with $\alpha = 0$ (dashed line in Fig. 6), here we also see oscillations for the $l = 1,2,3$ harmonics with respective frequencies $f^{\text{SdH}}, 2f^{\text{SdH}}$ and $3f^{\text{SdH}}$. However, for $l = 1$ we observe beating, which can be expected as both $\mathcal{F}_-(\varepsilon, B)$ and $\mathcal{F}_+(\varepsilon, B)$ frequencies now depend on $1/B$. More specifi-
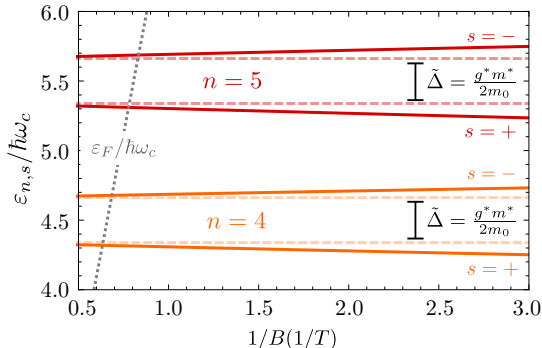
FIG. 5. Landau levels $n = 4, 5$ [Eq. (34)] as a function of $1/B$ for a 2DEG with non-zero Zeeman and Rashba interactions but no Dresselhaus coupling ($\beta = 0$). The dotted line denotes $\varepsilon_F/\hbar\omega_c$. The parameters here are $\alpha = 10\,\mathrm{meV\,nm}$, $m^* = 0.019 m_o$, $g^* = -34$ and $n_{2D} = 3.3 \times 10^{-3}\,\mathrm{nm}^{-2}$ for InSb-based wells[15,39]. The dashed lines show the corresponding levels for $\alpha = 0$.

cally, this beating appears here because in the magnetic range considered we have $2\pi l \mathcal{F}_-(B) = \frac{\pi}{2}$, which leads to a node in $\delta\rho_{xx}$ as $\delta\rho_{xx} \propto \cos\left[2\pi l \mathcal{F}_-(B)\right]$. Note that this only occurs for $l = 1$, since for higher harmonics this condition is not satisfied. Due to the larger amplitude of the harmonic $l = 1$, this beating is also seen in the total magneto-resistivity.

C. Landau Levels with Zeeman and Dresselhaus interaction

In the case of Zeeman with pure Dresselhaus, i.e., $\tilde{\Delta} \neq 0$, $\alpha = 0$ and $\beta \neq 0$, the Hamiltonian Eq. (9) in the spin basis is given by

$$\frac{\tilde{\mathcal{H}}}{\hbar\omega_c} = \begin{pmatrix} a^\dagger a + \frac{1}{2} - \frac{\tilde{\Delta}}{2} & 2\beta_B a^\dagger \\ 2\beta_B a & a^\dagger a + \frac{1}{2} + \frac{\tilde{\Delta}}{2} \end{pmatrix}. \quad (37)$$

Differently from the case of pure Rashba, here the operator $\mathcal{N}_- = a^\dagger a - \sigma_z/2$ commutes with the Hamiltonian above. For this case we have $\mathcal{N}_- |n,\downarrow\rangle = (n+1/2)|n,\downarrow\rangle$ and $\mathcal{N}_- |n+1,\uparrow\rangle = (n+1/2)|n+1,\uparrow\rangle$, i.e., for $n \in \mathbb{N}$, $|n,\downarrow\rangle$ and $|n+1,\uparrow\rangle$ are degenerate with respect to the operator $\mathcal{N}_-$, except for the state $|0,\uparrow\rangle$ with corresponding energy $\frac{\varepsilon_{0,\uparrow}}{\hbar\omega_c} = \frac{1}{2}(1+\tilde{\Delta})$. As a consequence, a linear combination of $|n,\downarrow\rangle$ and $|n+1,\uparrow\rangle$ is also an eigenstate of our Hamiltonian. Therefore, differently from the previous case here the Hamiltonian reads,

$$\tilde{\mathcal{H}} = \tilde{\mathcal{H}}_{|0,\uparrow\rangle} \oplus \bigoplus_{n=0}^{\infty} \tilde{\mathcal{H}}_{|n,\downarrow\rangle;|n+1,\uparrow\rangle}, \quad (38)$$

with $\tilde{\mathcal{H}}_{|0,\uparrow\rangle} = \varepsilon_{0,\uparrow}$ and

FIG. 6. Magnetoresistivity deviation $\delta\rho_{xx}(B)$ as a function of $1/B$ for a 2DEG with Zeeman and Rashba interactions and no Dresselhaus coupling ($\beta = 0$). The lowest curve corresponds to $\delta\rho_{xx}(B)$ and the curves labelled by l are the individual frequency components (i.e., harmonics) in Eq. (30). The solid lines are obtained with $g^* = -34$, $\alpha = 10\,\mathrm{meV\,nm}$, $m^* = 0.019 m_o$ and $n_{2D} = 3.3 \times 10^{-2}\,\mathrm{15,39}$; the dotted lines show the corresponding $\alpha = 0$ case.

$$\tilde{\mathcal{H}}_{|n,\downarrow\rangle;|n+1,\uparrow\rangle} = \hbar\omega_c \begin{pmatrix} n + \frac{1}{2} - \frac{\tilde{\Delta}}{2} & 2\beta_B\sqrt{n+1} \\ 2\beta_B\sqrt{n+1} & n + 1 + \frac{1}{2} + \frac{\tilde{\Delta}}{2} \end{pmatrix}. \quad (39)$$

The diagonalization of the Hamiltonian Eq. (39) yields energies

$$\frac{\varepsilon_{n,s}}{\hbar\omega_c} = \left(n + \frac{1}{2} - \frac{s}{2}\right) \quad (40)$$
$$+ \frac{s}{2}\frac{1+\tilde{\Delta}}{|1+\tilde{\Delta}|}\sqrt{\left(1+\tilde{\Delta}\right)^2 + 16\beta_B^2\left(n + \frac{1}{2} - \frac{s}{2}\right)},$$

with $s = \pm$ and $n \in \mathbb{N}_0$, which already incorporates the energy of the decoupled state $|0,\uparrow\rangle$, $\varepsilon_{0,+} \equiv \varepsilon_{0,\uparrow}$ ($\varepsilon_{0,-} \equiv \varepsilon_{0,\uparrow}$) if $1+\tilde{\Delta} > 0$ ($1+\tilde{\Delta} < 0$). Here, it is important to notice the opposite sign of s with respect to Eq. (33). This happens because the pure Dresselhaus Hamiltonian Eq. (39) has opposite basis ordering of the spin states as compared to the pure Rashba Hamiltonian Eq. (33). Accordingly, the $\mathcal{F}_\pm$ functions change slightly and read

$$\mathcal{F}_+(\varepsilon, B) = \frac{\varepsilon}{\hbar\omega_c} - \frac{1}{2} + 2\beta_B^2, \quad (41)$$

$$\mathcal{F}_-(\varepsilon, B) = \frac{1}{2} - \frac{1}{2}\frac{1+\tilde{\Delta}}{|1+\tilde{\Delta}|}\sqrt{\left(1+\tilde{\Delta}\right)^2 + 16\beta_B^2\left(\beta_B^2 + \frac{\varepsilon}{\hbar\omega_c}\right)}. \quad (42)$$

FIG. 7. Landau levels $n = 4, 5$ [Eq. (40)] as a function of $1/B$ for a 2DEG with Zeeman and Dresselhaus interations but no Rashba coupling ($\alpha = 0$). The dotted line denotes $\varepsilon_F/\hbar\omega_c$. The parameters here are $\beta = 10\,\mathrm{meV\,nm}$, $m^* = 0.019m_o$, $g^* = -34$ and $n_{2D} = 3.3 \times 10^{-3}\,\mathrm{nm}^{-2}$[15,39] dashed lines show the corresponding levels for $\beta = 0$.

Due to the: i) similarity of the Dresselhaus expression Eqs. (40), (41) and (42) to the ones arising from the pure Rashba case, Eqs. (34), (35) and (36); ii) cosine dependence of the $\mathcal{F}_\pm$ functions within the resistivity Eq. (22); all the results and equations in the last section also holds here by making $\alpha_B \rightarrow \beta_B$, $\tilde{\Delta} \rightarrow -\tilde{\Delta}$ and $s \rightarrow -s$. This can also be seen on the level of the Hamiltonian in Eq. (2) where applying the unitary transformation $W = e^{i\frac{\pi}{2}\sigma_x}e^{i\frac{\pi}{4}\sigma_z}$ results in

$$W\frac{\tilde{\mathcal{H}}}{\hbar\omega_c}W^\dagger = (a^\dagger a + 1/2) + \frac{(-\tilde{\Delta})}{2}\sigma_z + \beta_B(a^\dagger\sigma_- + a\sigma_+),$$
$$+ \alpha_B(a^\dagger\sigma_+ + a\sigma_-), \qquad (43)$$

which is the expected result. This mapping from $(\alpha, \tilde{\Delta})$ to $(\beta, -\tilde{\Delta})$ has visible consequences on the energy levels. In Fig. 7 we plot the corresponding LLs [Eq. (40)] as a function of $1/B$ for parameters $\beta = 10\,\mathrm{meV\,nm}$, $m^* = 0.019m_o$ and $g^* = -34$[15,39]. Due to the spin-orbit coupling, the energy levels $\frac{\varepsilon_{l,s}}{\hbar\omega_c}$ are no longer equidistant, and their separation changes as function of $1/B$. However, differently from the pure Rashba case, now the Dresselhaus competes with the Zeeman coupling, even leading to LL-dependent crossings. This can be seen through the expansion of $(1 + \tilde{\Delta})^2$ within the square root [Eq. (40)], which will give rise to $2\tilde{\Delta} < 0$, thus suppressing the spin splitting in the presence of Dresselhaus SO coupling.

In Fig. 8 we plot the total differential magnetoresistivity $\delta\rho_{xx}(B)$, and the individual contributions from the harmonics $l = 1, 2$ and $l = 3$. We use $\beta = 10\,\mathrm{meV\,nm}$, $m^* = 0.019m_o$, $g^* = -34$ and $n_{2D} = 3.3 \times 10^{-3}\,\mathrm{nm}^{-2}$[15,39]. First, similarly to the previous cases, here we can also clearly see oscillations with frequencies $f^{\mathrm{SdH}}, 2f^{\mathrm{SdH}}, 3f^{\mathrm{SdH}}$. Differently from the pre-

vious case with $\alpha = 10\,\mathrm{meV\,nm}$ and $\beta = 0$, now we see no beating for the $l = 1$ harmonic but find beating for $l = 2$. This happens as $2\pi l\mathcal{F}_-(B) = \frac{\pi}{2}$ – the condition to observe beating – is only satisfied for $l = 2$. Even though the beating appears within the second harmonic, it is not manifested in the total differential magnetoresistivity $\delta\rho_{xx}(B)$ for our choice of parameters. This is due to the smaller oscillation amplitude of $l = 2$ with respect to $l = 1$.

D. Beatings in the SdH oscillations with nonzero Zeeman and in the presence of either Rashba or Dresselhaus: a unified description

In this section we will discuss more thoroughly the conditions for the appearance of beatings. The two functions $\mathcal{F}_+$ and $\mathcal{F}_-$, Eq. (13), determine the fast and slow component, respectively, of the SdH oscillations. To highlight this point and its connection to the power spectrum in Eq. (26), we start by rewriting Eqs. (35)- (36), and Eqs.
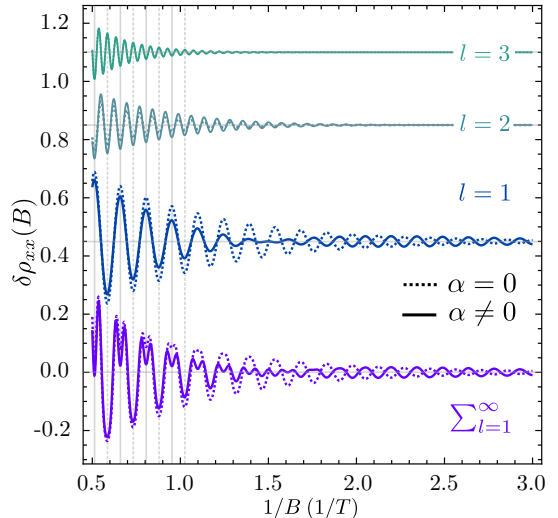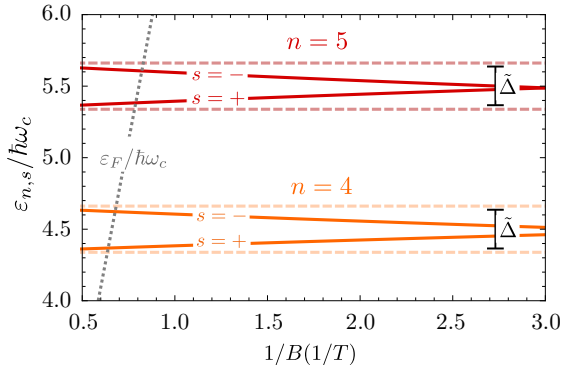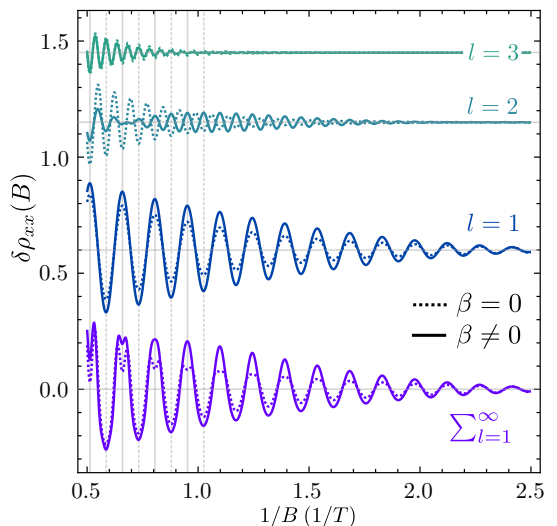

FIG. 8. Magnetoresistivity deviation $\delta\rho_{xx}(B)$ as a function of $1/B$ for a 2DEG with Zeeman and Dresselhaus interactions and no Rashba coupling ($\alpha = 0$). The lowest curve corresponds to $\delta\rho_{xx}(B)$ and the curves labelled by l are the individual frequency components in Eq. (30). The solid lines are calculated for $g^* = -34$, $\beta = 10\,\mathrm{meV\,nm}$, $m^* = 0.019m_o$ and $n_{2D} = 3.3 \times 10^{-3}\,\mathrm{nm}^{-2}$[15,39]; the dotted line shows the corresponding $\beta = 0$ case.

(42)- (42) in a unified way

$$\mathcal{F}_+(\varepsilon, B) = f_{R(D)}^{\text{SdH}} \frac{1}{B} - \frac{1}{2}, \tag{44}$$

$$\mathcal{F}_-(\varepsilon, B) = \mp\frac{1}{2} \pm \frac{1}{2} \frac{1 \mp \tilde{\Delta}}{|1 \mp \tilde{\Delta}|} \sqrt{(1 \mp \tilde{\Delta})^2 + 4\left(f_{R(D)} \frac{1}{B}\right)^2}, \tag{45}$$

where we have introduced the magneto-oscillation frequencies

$$f_{R(D)}^{\text{SdH}} = \frac{h}{2e}\left(n_{2D} + \frac{k_{R(D)}^2}{\pi}\right), \tag{46}$$

$$f_{R(D)} = \frac{h}{2e}\sqrt{\frac{2k_{R(D)}^2}{\pi}}\sqrt{n_{2D} + \frac{k_{R(D)}^2}{2\pi}}, \tag{47}$$

where the R (D) index refers to either pure Rasbha (Dresselhaus) case, with $k_R = \frac{m\alpha}{\hbar^2}$ ($k_D = \frac{m\beta}{\hbar^2}$). Here, the upper (lower) sign refers to the Rashba (Dresselhaus) case. In the case where $n_{2D} \gg k_{R(D)}^2/2\pi$, and
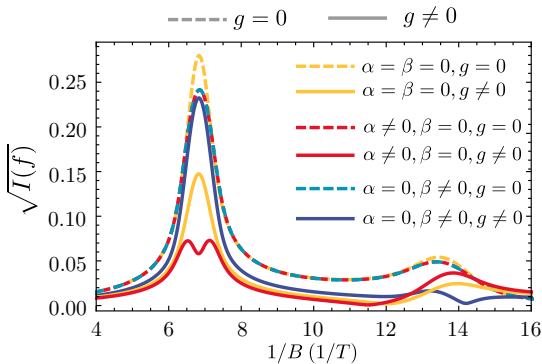
FIG. 9. Frequency response $\sqrt{I(f)}$ for $\alpha = 10.0\,\text{meV\,nm}$ and $\beta = 0.0$ [red curve], and $\alpha = 0.0$ and $\beta = 10.0\,\text{meV\,nm}$ [blue curve]. Other parameters are $m^* = 0.019m_o$, $g^* = -34$ and $n_{2D} = 3.3 \times 10^{-3}\,\text{nm}^{-2}$[15,39]. The solid black shows corresponds to no spin-orbit coupling ($\alpha = \beta = 0$) and black dashed corresponds to $\alpha = \beta = g = 0$.

$f_{R(D)}/B \gg 1$, the beating frequency takes the standard form $f_{R(D)} = \frac{h}{2e}\sqrt{2k_{R(D)}^2 n_{2D}/\pi}$, in which case $\tilde{\Delta}$ becomes irrelevant for the magnitude of the beating frequency[36].

The frequency $f_{R(D)}^{\text{SdH}}$ [Eq. (46)] is the main SdH frequency of the magneto-resistance oscillations, usually extracted from experiments to infer the 2D electronic density n_{2D}. On the other hand, the frequency $f_{R(D)}$ [Eq. (47)] is the one allowing for possible beatings in the magneto-oscillation. As previously discussed in the last two sections, the presence of beating happens when

$2\pi l \mathcal{F}_-(B) = \frac{\pi}{2}$ is satisfied, which depends on the value of both $f_{R(D)}$ and $\tilde{\Delta}$.

The presence or absence of beatings can also be visualized through the power spectrum defined by Eq. (26). From interference of waves, we know that the presence of beatings correspond to sum of cosines waves with slightly different frequencies. Accordingly, the power spectrum for this case would show two peaks located at slightly different frequencies. In Fig. 9 we plot $\sqrt{I(f)}$ for $m^* = 0.019m_o$ and $n_{2D} = 3.3 \times 10^{-3}\,\text{nm}^{-2}$, using different spin-orbit parameters and g-factor values. For all different sets of parameters, we always have the presence of two main peaks located at both $1/B \approx 6.8\,\text{T}^{-1}$ and $1/B \approx 13.6\,\text{T}^{-1}$. These correspond to the main SdH frequencies for the first and second harmonics, $f_{R(D)}^{\text{SdH}}$ and $2f_{R(D)}^{\text{SdH}}$, respectively. In the absence of both Rashba, Dresselhaus and g-factor (dashed yellow curve), we observe no beating in the $\delta\rho_{xx}$ (Fig. 4).

On the other hand, for the case of pure Rashba $\alpha = 10\,\text{meV\,nm}$ with $g = -34$ (solid red curve), the presence of the beating in Fig. 6 is made clear by the splitting of the peak of the power spectrum around $f = f_R^{\text{SdH}}$ in Fig. 9. Interestingly, for $\alpha = 10\,\text{meV\,nm}$ with $g = 0$ (dashed red curve), the splitting of the peak is not seen anymore, thus highlighting the important role of the Zeeman on the visualization of beatings. For the pure Dresselhaus case with $\beta = 10\,\text{meV\,nm}$ and $g = -34$ (solid blue line), we do not see a peak splitting at the $f = f_D^{\text{SdH}}$ but rather at $f = 2f_D^{\text{SdH}}$, which is consistent with the presence of the beating seen on the second harmonic in Fig. 8. Similarly to the pure Rashba case, for $\beta = 10\,\text{meV\,nm}$ with $g = 0$ (dashed blue line), the splitting of the peak is not seen anymore, corroborating again the role of the Zeeman term on the presence of beatings.

The apparent "asymmetry" in having peak-splitting for Rashba spin-orbit coupling but not for Dresselhaus (even when they have same SO strength) can be understood from the behavior of the $l\mathcal{F}_-$-function vs $1/B$, shown in Fig. 10. As already discussed previously in Secs. V B and V C, the condition for beating happens when $\cos(2l\pi\mathcal{F}_-) = 0$ or equivalently, $l\mathcal{F}_- = \pm 1/4$ ($\pm 1/4$ plotted as gray lines). In the case of Rashba (green lines) one has $(1 - \tilde{\Delta}) > 1$, and the condition for a beating node, $\cos(2l\pi\mathcal{F}_-) = 0$, is reached in the interval of $1/B$ for $l = 1$ (solid purple) (gray circles). In the Dresselhaus case, $(1 + \tilde{\Delta}) < 1$, such that $l\mathcal{F}_-$ for $l = 1$ only crosses $-1/4$ for large values of $1/B$, where the amplitude of the SdH has already been suppressed. Conversely, $l\mathcal{F}_-$ crosses $1/4$ for $l = 2$ at smaller values of $1/B$, thus guaranteeing the presence of a beating within the magnetic field range, as shown in Fig. 8.
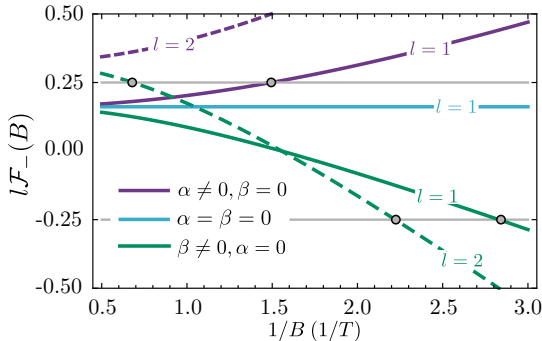
FIG. 10. Plot of $l\mathcal{F}_-(B)$ vs $1/B$ for $l = 1$ and $l = 2$ using $\alpha = 10\,\text{meVnm}$ with $\beta = 0$ (purple lines), $\alpha = \beta = 0$ (cyan lines), and $\beta = 10\,\text{meVnm}$ with $\alpha = 0$ (green lines). The solid gray lines indicate $\pm 1/4$ and the gray circles indicate where beating nodes occur. For all curves, we use $m^* = 0.019 m_o$, $g^* = -34$ and $n_{2D} = 3.3 \times 10^{-3}\,\text{nm}^{-2}$, parameters for InSb-based 2DEGs[15,39].

E. Landau Levels with simultaneous Zeeman, Rashba and Dresselhaus interactions: Analytical results

As mentioned earlier, to the best of our knowledge, there are no general *exact* analytical results for the energies and SdH oscillations corresponding to the case with simultaneous and arbitrary Zeeman, Rashba and Dresselhaus couplings. Therefore, in this section we will outline how to derive an effective *approximate* solution that can be used to shed light on magnetotransport results for materials, e.g. GaAs or InAs, in which all the three couplings are present. For convenience, we define the sum and difference of the spin-orbit couplings

$$\gamma = \alpha_B + \beta_B, \qquad (48)$$
$$\delta = \alpha_B - \beta_B, \qquad (49)$$

[see definitions of α_B and β_B following Eq. (9)] which allows us to rewrite Eq. (9) as

$$\frac{\tilde{\mathcal{H}}}{\hbar\omega_c} = a^\dagger a + \frac{1}{2} + \frac{\tilde{\Delta}}{2}\sigma_z + \frac{\gamma+\delta}{2}\left(a^\dagger \sigma_- + a\sigma_+\right)$$
$$+ \frac{\gamma-\delta}{2}\left(a^\dagger \sigma_+ + a\sigma_-\right). \qquad (50)$$

Note that both the pure Rashba and pure Dresselhaus cases are recovered from the equation above for $\gamma = \delta$ and $\gamma = -\delta$, respectively. Next, we define the Hamiltonian for $\gamma = \delta$ and $\gamma = -\delta$

$$\frac{\tilde{\mathcal{H}}_\pm}{\hbar\omega_c} = a^\dagger a + \frac{1}{2} + \frac{\tilde{\Delta}}{2}\sigma_z \pm \delta(a^\dagger \sigma_\mp + a\sigma_\pm), \qquad (51)$$

which describes the pure Rashba (+) and pure Dresselhaus (−) cases in the presence of the Zeeman coupling. As we already discussed in the previous sec-

tions, by defining the operator $\mathcal{N}_\pm = a^\dagger a \pm \frac{1}{2}\sigma_z$, we obtain $[\tilde{\mathcal{H}}_\pm, \mathcal{N}_\pm] = 0$, so the eigenstates of $\tilde{\mathcal{H}}_\pm$ are also eigenstates of $\mathcal{N}_\pm$. The eigenstates of $\mathcal{N}_+$ ($\mathcal{N}_-$) are then constructed from the pair $\{|n,\uparrow\rangle, |n+1,\downarrow\rangle\}$ ($\{|n,\downarrow\rangle, |n+1,\uparrow\rangle\}$). The above statement is true except for the decoupled eigenstates $|0,\uparrow\rangle$ ($|0,\downarrow\rangle$) with corresponding eigenenergy $\hbar\omega_c(1-\tilde{\Delta})/2$ [$\hbar\omega_c(1+\tilde{\Delta})/2$]. The diagonalization of each two state subspace results in

$$\frac{\varepsilon_{n,s}}{\hbar\omega_c} = \left(n + \frac{1}{2} + \frac{\delta}{|\delta|}\frac{s}{2}\right) - \frac{\delta}{|\delta|}\frac{s}{2}\left(1 - \frac{\delta}{|\delta|}\tilde{\Delta}\right)$$
$$\times \sqrt{1 + \frac{16\delta^2}{(1 - \frac{\delta}{|\delta|}\tilde{\Delta})^2}\left(n + \frac{1}{2} + \frac{\delta}{|\delta|}\frac{s}{2}\right)}, \qquad (52)$$

with $s = + (-)$ and $n \in \mathbb{N}_0$. Note that this form is valid for both pure Rashba ($\delta = \gamma > 0$) and Dresselhaus ($\delta = -\gamma < 0$), Eqs. (34) and (40), respectively, thus also including the corresponding decoupled state with the lowest eigenvalues of $\mathcal{N}_\pm$. Note that to recover the pure Zeeman case with no Rashba and Dresselhaus, we should take $\delta \to 0$ with $\delta/|\delta| \to 1$.

When both Rashba and Dresselhaus are present, we can use second order perturbation theory with respect to $\delta, \gamma \ll 1$ (See Appendix E), to obtain the approximate eigenvalues of the Hamiltonian in Eq. (50), namely

$$\frac{\varepsilon_{n,s}}{\hbar\omega_c} = n + 1/2 + s\frac{\tilde{\Delta}}{2} - 2s\Lambda(l + 1/2) - \Omega \qquad (53)$$

where the quantities Λ and Ω are defined as

$$\Lambda = \frac{(\gamma^2 + \delta^2)\tilde{\Delta} + 2\gamma\delta}{(1 - \tilde{\Delta}^2)} = \frac{2\frac{\varepsilon_R}{\hbar\omega_c}}{(1 - \tilde{\Delta})} - \frac{2\frac{\varepsilon_D}{\hbar\omega_c}}{(1 + \tilde{\Delta})}, \quad (54)$$

$$\Omega = \frac{(\gamma^2 + \delta^2) + 2\gamma\delta\tilde{\Delta}}{(1 - \tilde{\Delta}^2)} = \frac{2\frac{\varepsilon_R}{\hbar\omega_c}}{(1 - \tilde{\Delta})} + \frac{2\frac{\varepsilon_D}{\hbar\omega_c}}{(1 + \tilde{\Delta})}, \quad (55)$$

where we have introduced $\varepsilon_R/\hbar\omega_c = \alpha_B^2$ and $\varepsilon_D/\hbar\omega_c = \beta_B^2$.

Our goal now is to rewrite Eq. (53) in a form that recovers the already obtained exact results for pure Rashba and pure Dresselhaus cases. First, we write $\Lambda = \frac{\Lambda}{|\Lambda|}|\Lambda|$ since Λ changes sign depending on the relative strengths of α and β, similarly to the sign of δ that enters into Eq. (52). By adding and subtracting a term $\frac{s}{2}\frac{\Lambda}{|\Lambda|}$ in Eq. (53) and after some straightforward algebra we obtain

$$\frac{\varepsilon_{n,s}}{\hbar\omega_c} = \left(n + \frac{1}{2} + \frac{\Lambda}{|\Lambda|}\frac{s}{2}\right) - \frac{\Lambda}{|\Lambda|}\frac{s}{2}\left(1 - \frac{\Lambda}{|\Lambda|}\tilde{\Delta}\right)$$
$$\times \left\{1 + \frac{4}{1 - \frac{\Lambda}{|\Lambda|}\tilde{\Delta}}\left[|\Lambda|\left(n + \frac{1}{2}\right) + \Omega\frac{\Lambda}{|\Lambda|}\frac{s}{2}\right]\right\}. \qquad (56)$$

In the case of pure Rashba we have $\Lambda = \Omega = \frac{\delta^2}{1-\Delta} > 0$ while for pure Dresselhaus $\Lambda = -\Omega = -\frac{\delta^2}{1+\Delta} < 0$; these

neatly reduce to the exact results when using second order Taylor expansion of Eq. (52). Note that Eq. (56) also reproduces the exact result for when $\alpha = \beta$ and $g^* = 0$

[62], represented here by $\Lambda \to 0$ with $\Lambda/|\Lambda| \to 1$, $\tilde{\Delta} = 0$, and $\Omega = 2\varepsilon_{D/R}/\hbar\omega_c$. The mathematical expression of Eqs. (34) and (40) motivate us to rewrite Eq. (56) as

$$\frac{\varepsilon_{n,s}}{\hbar\omega_c} = \left(n + \frac{1}{2} + \frac{\Lambda}{|\Lambda|}\frac{s}{2}\right) - \frac{\Lambda}{|\Lambda|}\frac{s}{2}\frac{1 - \frac{\Lambda}{|\Lambda|}\tilde{\Delta}}{|1 - \frac{\Lambda}{|\Lambda|}\tilde{\Delta}|} \times \sqrt{\left(1 - \frac{\Lambda}{|\Lambda|}\tilde{\Delta}\right)^2 + 8\left(1 - \frac{\Lambda}{|\Lambda|}\tilde{\Delta}\right)\left[|\Lambda|\left(n + \frac{1}{2}\right) + \Omega\frac{\Lambda}{|\Lambda|}\frac{s}{2}\right]}, \quad (57)$$

where we have used $1 + \frac{x}{2} \approx \sqrt{1 + x}$[63]. It is important to note that although $|\Lambda| \ll 1$, Λ enters the square root multiplied by n, the Landau level index. This means that for high enough n, the product $|\Lambda|n$ is not necessarily a small quantity. Accordingly, although the equation above becomes exact for either pure Rashba or Dresselhaus case, for $\alpha, \beta \neq 0$ Eq. (57) is only valid when $|\Lambda|n \lesssim 1$, besides $\alpha_B, \beta_B, \delta, \gamma \ll 1$ already assumed in Appendix E to obtain Eq. (53).

We reiterate that Eq. (57) satisfies the exact results for (i) the Zeeman-only case [Eq. (27)], (ii) the pure Rashba plus nonzero g^* [Eq. (34)] and (iii) the pure Dresselhaus

plus nonzero g^* [Eq. (40)]. The case $\alpha = \beta$ with $g^* = 0$, for which there is also an exact solution[62], is satisfied to leading order using $\sqrt{1 + x} \approx 1 + x/2$ for with $x = 8\Omega(s/2)/(1 - \tilde{\Delta}) \ll 1$. That is, as mentioned in the previous paragraph, the approximate solution given by Eq. (56) reproduces the exact solution for $\alpha = \beta$ with $g^* = 0$[62].

As in the case of pure Zeeman, Rashba or Dresselhaus, we can now calculate the F-function from Eq. (57). The corresponding results are presented in Appendix F, and by neglecting SO contributions higher or equal than second order in the spin-orbit parameters Λ and Ω (or fourth order in γ and δ), we obtain

$$\mathcal{F}_+ = \frac{\varepsilon}{\hbar\omega_c} - \frac{1}{2} + \Omega - \Lambda\tilde{\Delta}, \quad (58)$$

$$\mathcal{F}_- = -\frac{1}{2}\frac{\Lambda}{|\Lambda|} + \frac{1}{2}\frac{\Lambda}{|\Lambda|}\frac{1 - \frac{\Lambda}{|\Lambda|}\tilde{\Delta}}{|1 - \frac{\Lambda}{|\Lambda|}\tilde{\Delta}|}\sqrt{\left(1 - \frac{\Lambda}{|\Lambda|}\tilde{\Delta}\right)^2 + 8|\Lambda|\left(1 - \frac{\Lambda}{|\Lambda|}\tilde{\Delta}\right)\left[\frac{\varepsilon}{\hbar\omega_c} + \frac{1}{2}|\Lambda|\left(1 - \frac{\Lambda}{|\Lambda|}\tilde{\Delta}\right)\right]}. \quad (59)$$

It is easy to see that these equations recover all the previous results: pure Zeeman [Eq. (29)], Zeeman with pure Rashba [Eqs. (35) and (36)], and Zeeman with pure Dresselhaus [Eqs. (41) and (42)]. Additionally, in the case of $\Lambda \approx 0$, $\mathcal{F}_- \approx -\tilde{\Delta}/2$, which reduces to the pure Zeeman case. Accordingly, here $\mathcal{F}_-$ becomes independent of B (for $B \lesssim 1$ T), and therefore, we expect the absence of beatings in the magneto-resistivity, previously seen for

both pure Rashba and pure Dresselhaus cases.

F. Generalized SdH magneto-resistivity for arbitrary α, β and g^* : new prediction for the absence of beatings.

Using the Eqs. (58) and (59) in Eq. (24), we can derive the magnetoresistivity $\delta\rho_{xx}(B)$ for the case with arbitrary Rashba and Dresselhaus couplings and simultaneous nonzero Zeeman field,

$$\delta\rho_{xx}(B) = 2\sum_{l=1}^{\infty} e^{-l\pi\frac{\hbar/\tau_q}{\hbar\omega_c}}\frac{2\pi^2 l k_B T/\hbar\omega_c}{\sinh(2\pi^2 l k_B T/\hbar\omega_c)}$$

$$\times \cos\left[2\pi l\left(\frac{\varepsilon_F}{\hbar\omega_c} + \frac{2\varepsilon_R}{\hbar\omega_c} + \frac{2\varepsilon_D}{\hbar\omega_c}\right)\right]\cos\left\{\pi l\sqrt{\left(1 - \frac{\Lambda}{|\Lambda|}\tilde{\Delta}\right)^2 + 16\lambda_B^2\left(\lambda_B^2 + \frac{\varepsilon_F}{\hbar\omega_c}\right)}\right\}, \quad (60)$$

with $\lambda_B^2 = \frac{|\Lambda|}{2}\left(1 - \frac{\Lambda}{|\Lambda|}\tilde{\Delta}\right)$. From Eq. (60), we can derive the condition for the absence of beatings for any l by finding the condition for the second cosine being independent of $1/B$; this implies $|\Lambda| = 0$, which leads to

$$\frac{\alpha}{\beta} = \sqrt{\frac{1 - \tilde{\Delta}}{1 + \tilde{\Delta}}}, \qquad (61)$$

thus yielding Eq. (1) presented in the introduction. For $\tilde{\Delta} \ll 1$, the above condition is reduced to $\alpha \approx \beta$, corresponding to the situation where the total SO k-dependent effective field becomes unidirectional[5–7].

Note that the above condition does not correspond to any fundamental symmetry, since there is no new conserved quantity in our Hamiltonian with both non-zero Zeeman ($g^* \neq 0$) and Rashba-Dresselhaus couplings. We reiterate that Eq. (61) is entirely distinct from the persistent-spin-helix condition $\alpha = \beta$. As shown in Fig. 1(d), the case $\alpha = \beta$ and $g^* \neq 0$ does not show peak splitting in the first harmonic but ehxibits beating (or peak splitting) in the second harmonic. Only when $g^* = 0$ (no Zeeman) and $\alpha = \beta$ there are peak splittings absent altogether[44,62].

G. Beatings for both α and β non-zero

In the previous sections, we studied the effect of the Zeeman interaction on the frequency splitting of the power spectrum peaks, which represents the beatings in the SdH oscillations. Here we study the interplay of *both* the Dresselhaus and Rashba interactions on the beatings of the SdH oscillations.

Similarly to what we did leading up to Eq. (47), we can obtain the effective beating frequency from the $\mathcal{F}_{--}$ function in Eq. (59) which results in

$$f_{R+D} = \frac{h}{2e}\sqrt{\left|\frac{2k_{R+D}^2}{\pi}\left(n_{2D} + \frac{k_{R+D}^2}{2\pi}\right)\right|}, \qquad (62)$$

where the effective SO momentum is

$$k_{R+D} = \frac{m^*}{\hbar^2}\sqrt{\left(1 - \frac{\Lambda}{|\Lambda|}\tilde{\Delta}\right)\left(\frac{\alpha^2}{1 - \tilde{\Delta}} - \frac{\beta^2}{1 + \tilde{\Delta}}\right)}. \qquad (63)$$

We start with the pure Rashba case plus Zeeman, $\alpha = 7.0$ meV nm and $g^* = -34$. The corresponding power spectrum yields the bottom curve in Fig. 11, similar to the one plotted in Fig. 9. This curve shows two main peaks representing the first two harmonics, and the presence of a split main peak. We assume a Lorentzian broadening $\hbar\tau_q^{-1} = 1.75$ meV. When the Dresselhaus coupling β increases, we see the splitting of the main peak reduces until it vanishes for $\beta = 5.0$ meV nm (the frequency splitting from Eq. (62) is indicated by the gray circles). The absence of beating is indeed expected as predicted by the
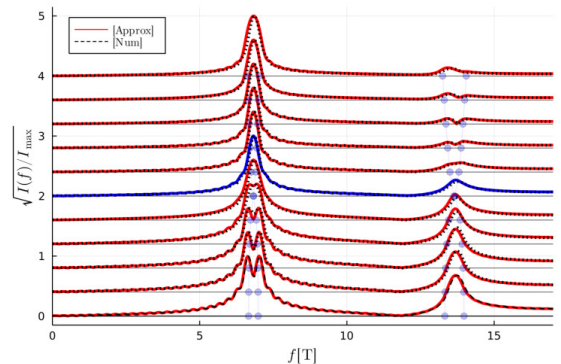
FIG. 11. Normalized power spectrum $\sqrt{I(f)}$ for a *fixed* $\alpha = 7.0$ meV nm, and for $\beta = 0.0$ to 10 meV nm, from bottom to top. [red curves], along with *full* numerical results [black dashed]. The curve corresponding to $k_{RD} = 0$ with $\beta = 5.0$ meV nm, is shown [blue curve]. The gray circles indicate the frequency splitting in Eq. (62). Other parameters are $m^* = 0.019m_o$, $g^* = -34$, $n_{2D} = 3.3 \times 10^{-3}$ nm^{-2}, and $\hbar\tau_q^{-1} = 1.75$ meV, for InSb-based 2DEGs[15,39]
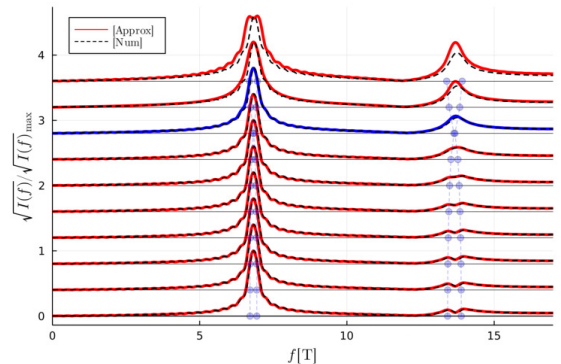
FIG. 12. Normalized power spectrum $\sqrt{I(f)}$ for a fixed $\beta = 5.0$ meV nm, and for $\alpha = 0.0$ to 9.0 meV nm, from bottom to top. [red curves] along with *full* numerical results [black dashed]. The curve corresponding to $k_{RD} = 0$ with $\alpha = 7.0$ meV nm [blue curve]. The gray circles indicate the frequency splitting in Eq. (62). Other parameters are $m^* = 0.019m_o$, $g^* = -34$, $n_{2D} = 3.3 \times 10^{-3}$ nm^{-2}, and $\hbar\tau_q^{-1} = 1.75$ meV, for InSb-based 2DEGs[15,39]

condition $\beta = \alpha\sqrt{\frac{1+\tilde{\Delta}}{1-\tilde{\Delta}}} = 5.0$ meV in Eq. (61). For larger β, we see that the splitting of the main peak remains neglible. However, in the second harmonic a clear splitting opens up. The condition for having no peak splitting at any harmonics is indeed the condition in Eq. (61), where the effects of the SO couplings basically disappear [there are still small SO terms ε_R, ε_D in Eq. (60)]. The power spectrum using full numerical calculations are also

shown [black dashed], and for this parameter regime the analytical and numerical results agree well.

A similar analysis can be done for the case of pure Dresselhaus with Zeeman, $\beta = 5.0$ meV nm and $g^* = -34$, see Fig. 12. Here the splitting is not observed in the main peak, but rather in the second harmonic. As α is increased from 0.0 to 9.0 meV nm, the splitting in the second harmonic decreases, and vanishes at $\alpha = 7.0$ meV nm, which again corresponds to the condition in Eq. (61). Despite the good accuracy of the approximate analytical solution for $\alpha \lesssim 8.0$ meV nm, it starts to deviate from the exact one (*full* numerics) for higher values of β. This happens because for these values, the combined effect Rashba and Dresselhaus is more pronounced, producing an anti-crossing between different energy levels (see blue curves Fig. 14, discussed further below). While the approximate energies obtained here are always monotonic with respect to $1/B$, around the anti-crossing the numerical ones are not. Accordingly, our F-function calculation will not be able to fully describe the SdH oscillations and frequencies around the anti-crossing regions, specifically the approximate solution misses a central peak that starts developing, which will be discussed in the next section. In terms of the F-function, the occurance of level anticrossings corresponds to $|\mathcal{F}_-| \approx 1/2$. Since the power spectrum is obtained by integrating $\delta\rho_{xx}$ over a range of $1/B$, there is no simple condition determining the validity of the approximate solution. However, looking at the λ_B term in Eq. (59) the condition

$$8\pi n_{2D} \left(\frac{k_R^2}{1-\tilde{\Delta}} - \frac{k_D^2}{1+\tilde{\Delta}} \right) l_c^4 \lesssim 1, \qquad (64)$$

yields a useful estimate for the $1/B$ values where the Dingle factor has not suppressed $\delta\rho_{xx}$. Equation (64) generalizes a similar condition derived in Ref. 57. It is also interesting to note that the analytical result is more accurate for higher harmonics, as the Dingle-factor helps diminishing the amplitude of the anti-crossing at higher-fields (see Fig. 14).

VI. LANDAU LEVELS WITH ZEEMAN, RASHBA AND DRESSELHAUS INTERACTIONS: NUMERICAL RESULTS

In the previous section, we have derived an approximate analytical result for the magnetoresistance oscillations in the presence of both Rashba, Dresselhaus *and* Zeeman interactions. The assumptions and approximations underlying the derivation involved the relatively small SO coupling and the low number of occupied Landau levels. These are satisfied in the low electron density InSb-based 2DEGs of Refs. 39 and 64. For higher electron density systems (but still with just a singly-occupied subband at $B = 0$), such as the InAs/GaSb wells in Ref. 41, a numerical approach is needed. Below we outline the numerical procedure. The numerical approach also allows us to account for the full form of cubic Dresselhaus term, see Sec. VI A.

For the case of either pure Rashba or Dresselhaus with Zeeman, the absence of anti-crossing in the LL spectrum allow us to obtain *exact* analytical results for the problem. As we explain below, this does *not* hold in the presence of both Rashba and Dresselhaus with the Hamiltonian (in the spin basis) Eq. (9)

$$\frac{\tilde{\mathcal{H}}}{\hbar\omega_c} = \begin{pmatrix} a^\dagger a + \frac{1}{2} + \frac{\tilde{\Delta}}{2} & 2\alpha_B a + 2\beta_B a^\dagger \\ 2\alpha_B a^\dagger + 2\beta_B a & a^\dagger a + \frac{1}{2} - \frac{\tilde{\Delta}}{2} \end{pmatrix}. \qquad (65)$$

Therefore, here we calculate the magnetotransport numerically via the diagonalization of the Hamiltonian above. The F-function method used for the analytical cases can be extended to allow for numerical methods for calculating the energy spectrum, see App. D.

As opposed to both the pure Rashba and pure Dresselhaus cases, $\mathcal{N}_\pm$ do not commute with the Hamiltonian above, and therefore, the diagonal basis cannot be described by any linear combination of the previous degenerate eigenstates of $\mathcal{N}_\pm$. However, there is still a unitary operator, $\mathcal{P} = \exp\left\{i\pi\left(\mathcal{N}_\pm - \frac{1}{2}\right)\right\}$ that commutes with this Hamiltonian, called the *parity* operator [51,52], which is discussed in detail in App. B. The corresponding unitary transformation gives $\mathcal{P}a\mathcal{P}^\dagger = -a$, $\mathcal{P}a^\dagger\mathcal{P}^\dagger = -a^\dagger$ and $\mathcal{P}\sigma_\pm\mathcal{P}^\dagger = -\sigma_\pm$, which clearly makes the Hamiltonian Eq. (9) invariant due to presence of only $a^\dagger a$, $a^\dagger\sigma_\pm$ and $a\sigma_\pm$ terms. The eigenvalues of $\mathcal{P}$, ± 1, help analyze the energy spectrum behavior.

To understand the influence on the spectrum of both Rashba and Dresselhaus contributions, we first recall that in the absence of the latter, the Rashba term is responsible for coupling $|n, \uparrow\rangle$ to $|n+1, \downarrow\rangle$, for $n \in \mathbb{N}_0$, thus yielding decoupled 2×2 block diagonal Rashba Hamiltonians (shown by the red boxes in the Hamiltonian below). When we account for the Dresselhaus contribution, we obtain a coupling between states $|n, \downarrow\rangle$ and $|n+1, \uparrow\rangle$ for $n \in \mathbb{N}_0$, which belongs to different Rashba blocks. More specifically, the Dresselhaus term produces a coupling between blocks $\{|n, \uparrow\rangle, |n+1, \downarrow\rangle\}$ and $\{|n+\Delta n, \uparrow\rangle, |n+1+\Delta n, \downarrow\rangle\}$ with $\Delta n = 2$, which is indicated by the blue box in the Hamiltonian below (See App. B). As a consequence, we have two decoupled orthogonal basis set given by $\{|0^+\rangle\} = \{|n, \uparrow\rangle, |n+1, \downarrow\rangle, \ldots\}$ and $\{|0^-\rangle\} = \{|n, \downarrow\rangle, |n+1, \uparrow\rangle, \ldots\}$ with $n \in \mathbb{N}_0$. Interestingly, these decoupled basis have different eigenvalues with respect to the parity operator, i.e., $\mathcal{P}|0^\pm\rangle = \pm 1|0^\pm\rangle$ and therefore, represent different parity subspace.

In terms of the spectrum, in the presence of only Rashba SO coupling, we observe multiple crossing between the Rashba eigenstates $\{|n, -\rangle, |n, +\rangle\}$ for different $n \in \mathbb{N}_0$, with energy given by Eq. (34), obtained through the diagonalization of the Rashba blocks (red boxes within the Hamiltonian matrix in Fig. 13). This is shown by the red solid lines in Fig. 14(a) for $\alpha = 7.5$ meV nm.

FIG. 13. Graphical illustration of the parity subspaces in the *matrix* representation of the Hamiltonian Eq. (65). Here we see the Rashba interaction couples $|n-1,\uparrow\rangle$ to $|n,\downarrow\rangle$ (red boxes), while the Dresselhaus interaction couples $|n,\downarrow\rangle$ to $|n+1,\uparrow\rangle$ (blue boxes).

In the presence of Dresselhaus SO coupling, the states $|n,-\rangle$ and $|n+\Delta n,+\rangle$ with $\Delta n \in \mathbb{N}_{odd}$ belong to the same parity subspace and adding a Dresselhaus contribution will yield anti-crossing, which open up gaps in the spectrum (blue curves). Conversely, the decoupling between the different parity sets, i.e., $|n,-\rangle$ and $|n+\Delta n,+\rangle$ with $\Delta n \in \mathbb{N}_{even}$, implies multiple crossing between their corresponding energy states. These features are shown by the blue curve in Figs. 14(a) and (c), where we have used $\beta = 3.0\,\text{meV nm}$. Other parameters are $m^* = 0.04$, $g^* = -12$ and $n_{2D} = 17.6 \times 10^{-3}\,\text{nm}^{-2}$. These parameters are for InAs/GaSb-based (double) quantum wells[41] in the electron regime. This regime, as emphasized in Ref. 41, corresponds to the configuration in which the GaSb well is depleted and the system is effectively a single InAs-based asymmetric quantum well with electrons only. Furthermore, we also observe that the effect of the Dresselhaus term is to simply shift the crossing point to a different magnetic field and energy (the crossing-point energy remains constant to lowest order in β but does in general shift for higher values of β).

The contrasting behavior of crossings vs. anti-crossings has direct consequences on the F-function, which will be analyzed in the next paragraphs. First we consider the crossing between states $|n,-\rangle$ and $|n+\Delta n,+\rangle$, with *even* Δn (corresponding to states belonging to different parity subspaces). The F-function are

$$\varepsilon_{n,-}(B) = \frac{\varepsilon}{\hbar\omega_c} \leftrightarrow n = F_-\left(\frac{\varepsilon}{\hbar\omega_c}, B; \alpha, \beta\right), \quad (66)$$

and

$$\varepsilon_{n+\Delta n,+}(B) = \frac{\varepsilon}{\hbar\omega_c} \leftrightarrow n+\Delta n = F_+\left(\frac{\varepsilon}{\hbar\omega_c}, B; \alpha, \beta\right) \quad (67)$$

where we have explicitly added their dependence on α and β. This results in an F-function difference [see Eq. 13] at the crossing $\varepsilon = \varepsilon_c$ and $B = B_c$

$$\mathcal{F}_-\left(\frac{\varepsilon_c}{\hbar\omega_c}, B_c; \alpha, \beta\right) = \frac{\Delta n}{2} \in \mathbb{Z}. \quad (68)$$

Note that since the SdH oscillation is dependent on $\mathcal{F}_\pm$ in the form of $\cos(2\pi\mathcal{F}_\pm)$, we can re-define $\mathcal{F}_-$ to lie within an unit interval, e.g., $\mathcal{F}_- \in [-1/2, 1/2]$. Accordingly, integer values of $\mathcal{F}_-$ are equivalent to $\mathcal{F}_- = 0$ and therefore, the vanishing of $\mathcal{F}_-$ provides the field values where the crossing happens. The curves for $\mathcal{F}_-$ are plotted in Fig. 14(b) for the same parameters as in Fig. 14(a). It presents a sawtooth pattern because values of $|\mathcal{F}_-| > 1/2$ are shifted back to the $[-1/2, 1/2]$ interval. The role of the Dresselhaus coupling for these crossings is evident in Fig. 14(b), where the zeros of $\mathcal{F}_-$ remain zeros for any value of β, but are simply shifted to new values of magnetic field, open circle moves to open rectangle Fig. 14(b).

Next, we look at the crossing between states belonging to the same parity subspace, i.e., $|n,-\rangle$ and $|n+\Delta n,+\rangle$ for odd Δn. We recall that this crossing only exists for the pure Rashba case, shown in both Figs. 14(a) and (c). Here the relations in Eqs. (66) and (67) still hold, the only difference being the value of Δn, which results in

$$\mathcal{F}_-\left(\frac{\varepsilon_c}{\hbar\omega_c}, B_c; \alpha, \beta = 0\right) = \frac{\Delta n}{2} \in \mathbb{Z} + \frac{1}{2}. \quad (69)$$

Adding a non-zero Dresselhaus contribution will couple these states and lead to an anti-crossing, shown in Figs. 14(a) and (c). The anti-crossing result in non half-integer values of $\mathcal{F}_\pm$ in Eqs. (66) and (67) and will lead to a rounding of the sawtooth pattern as seen in Fig. (14)(b) (blue curves).

The conditions in Eqs. (68) and (69) lead to values of $\cos(2\pi\mathcal{F}_-) = 1$ [filled circle and rectangle in Fig. 14b)] and $\cos(2\pi\mathcal{F}_-) = -1$ [open cirlce circle in 14b)], respectively, in the case of either pure Rashba or pure Dresselhaus. However, when both Rashba and Dresselhaus are

present only the former condition $\cos(2\pi\mathcal{F}_-) = 1$ holds (crossing of states with opposite parity) but the latter condition changes such that $\cos(2\pi\mathcal{F}_-) > -1$ due to anticrossings of states with same parity eigenvalue [open rectangle in Fig. 14b]. This, in turn, affects the shape of the magneto-oscillations leading to an asymmetry in the maximum and minimum values of $\cos(2\pi\mathcal{F}_-)$.
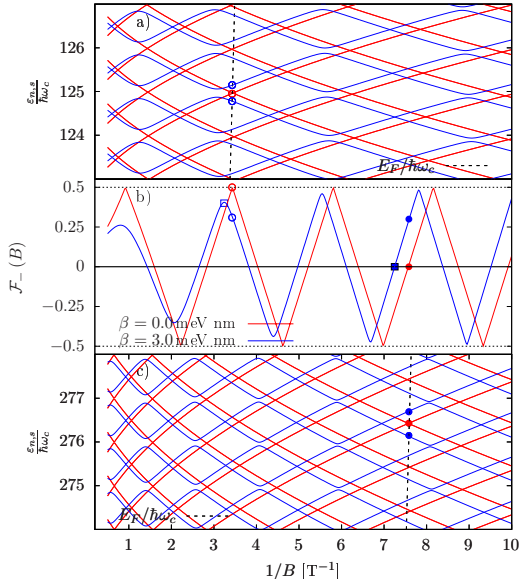

FIG. 14. The energy spectrum for two sets of $(\alpha, \beta) = (7.5, 0.0)$ meV nm [red] and $(\alpha, \beta) = (7.5, 3.0)$ meV nm [blue], along with $\varepsilon_F/\hbar\omega_c$ (black dashed), a) around $n = 125$ and c) $n = 255$. b) $\mathcal{F}_c$ for the same pair of parameters. Note sawtooth form for pure Rashba [red], and for $(\alpha, \beta) = (7.5, 3.0)$ meV nm [blue] a rounding, and translation, of the cusps due to level anticrossing [solid circles]. Other parameters are $m^* = 0.04$, $g^* = -12$ and $n_{2D} = 17.6 \times 10^{-3}$ nm^{-2}, for InAs-based quantum wells[41].

In Fig. 15 this asymmetry is visible in the magneto-osillations. Here we assume Gaussian broadening with $B_q = 0.50$ T which forms an envelope (black dashed curve). The lowest curve is the pure Rashba $(\alpha, \beta) = (7.5, 0.0)$ meV nm and there *all* maximas intersect the envelope [black circles]. The curve for $(\alpha, \beta) = (7.5, 3.0)$ meV nm shows that only *some* maxima intersect the envelope, the other maximas correspond to $\cos(2\pi\mathcal{F}_-) > -1$ do not (black circle). This is a direct consequence of the anti-crossing in the spectrum in Fig. 14. The curves for $(\alpha, \beta) = (5.5, 3.0)$ meV nm and $(4.5, 3.0)$ meV nm show how the anti-crossing becomes larger, eventually leading to an absence of beatings. This can also be seen in the frequency spectrum shown in Fig. 16, for the $f \approx f^{\text{SdH}}$ peak. The lowest curve (blue) corresponds to $(\alpha, \beta) = (7.5, 3.0)$ meV nm where the spectrum shows well separated peaks. How-
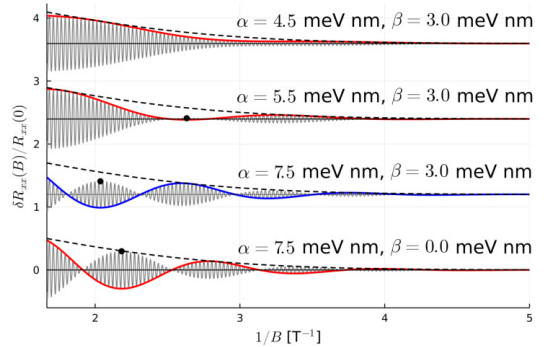
FIG. 15. Magnetooscillations for four different parameter values, including pure Rashba, then different combinations of (α, β). The anti-crossings in the spectrum complicates the beating behavior, which eventually vanishes for around $(\alpha, \beta) = (4.5, 3.0)$ meV nm. Other parameters are $m^* = 0.04$, $g^* = -12$ and $n_{2D} = 17.6 \times 10^{-3}$ nm^{-2}.

ever, as the strength of the Rashba coupling is decreased all the way down to $\alpha = 0.5$ meV nm for a fixed value of $\beta = 3.0$ meV nm a central peak develops and for α between 4.5 and 1.5 meV nm, the two split peaks are barely visible.
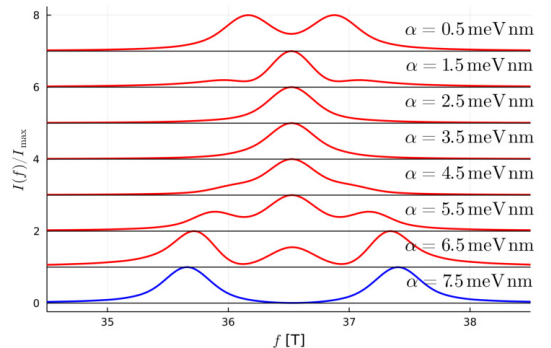
FIG. 16. Power spectrum for af *fixed* $\beta = 3.0$ meV nm for $\alpha = 7.5$ down to 0.5 meV nm. Other parameters are $m^* = 0.04$, $g^* = -12$ and $n_{2D} = 17.6 \times 10^{-3}$ nm^{-2}, from Ref. 41.

A. Extracting α and β from SdH data

The magneto-oscillations can be thought of as a fingerprint of the sample parameters, including Fermi energy ε_F, effective mass m^*, g^*, and α and β. To better capture the influence of the spin-orbit couplings for higher electron density, the *full* form of the Dresselhaus interaction will be used. For non-zero magnetic fields, this

corresponds to having Dresselhaus SO term in Eq. (9) replaced with

$$\left[\frac{1}{\sqrt{2}\hbar\omega_c\ell_c} \left(\beta_1 - \gamma\frac{a^\dagger a}{2\ell_c^2} \right) a^\dagger\sigma_+ + \frac{\gamma}{2\ell_c^2} a^3\sigma_- \right] + \text{h.c.} \quad (70)$$

where $\beta_1 = \gamma\langle k_z^2\rangle$, γ is material-dependent parameter describing the SO interaction due to bulk inversion asymmetry, and $\langle k_z^2\rangle$ is the expectation value of the z-component of the square of momentum operator (divided by $\hbar$), see App. C for details of $full$ Dresselhaus coupling. Note that β in Eq. (2) is assumed to include the first harmonic of the cubic Dresselhaus[7,49], which makes it linearly dependent on the electron density. For instance, if the potential confining the 2DEG is assumed to be an infinite well of width d_{QW} then $\langle k_z^2\rangle = \pi^2/d_{\mathrm{QW}}^2$. To model the magnetoresistance data we start from Eq. (22), which features (i) a sum over higher harmonics, (ii) rapid oscillations coming from $\mathcal{F}_+$, and (iii) damping due to Landau level broadening $\tilde{L}_\Gamma$. The analysis introduced in the previous section was based on the study of the properties of $\cos(2\pi\mathcal{F}_-)$, which forms an envelope on top of the rapid oscillations. Note that in the case having both Rashba and Dresselhaus coupling the rapid oscillations are still dominated by the normal SdH oscillations, i.e.

$$\mathcal{F}_+(B) = -\frac{1}{2} + \frac{\varepsilon_F}{\hbar\omega_c}\left(1 + \mathcal{O}\left(\frac{\varepsilon_R}{\varepsilon_F}, \frac{\varepsilon_D}{\varepsilon_F} \right) \right)$$
$$\approx -\frac{1}{2} + \frac{f^{\mathrm{SdH}}}{B}, \quad (71)$$

so the SO coupling does not affect the rapid oscillations. The resulting lowest harmonic form of the magnetoresistivity is

$$\delta\rho_{xx}(B) = -2\tilde{L}_\Gamma(B)\cos(2\pi l\mathcal{F}_-(B))\cos\left(2\pi\frac{f_{\mathrm{SdH}}}{B} \right), \quad (72)$$

which can be fitted to available data.

Figures 17-19 show the experimental data from Ref. 41 for InAs/GaSb quantum wells in the electron regime) along with our theoretical fits [Eq. (72)]. We focus on the experimental curves 1, 5 and 10, of Fig. S4 of Ref. 41 that we label as C1, C5 and C10 in Fig. 17-19. The data was fitted to $\delta\rho_{xx}(B)$ in Eq. (72), where $\mathcal{F}_-$ was calculated numerically. For the fitting we consider both the Dresselhaus coupling in Eq. (9) [black dashed lines], and also with the $full$ Dresselhaus term in Eq. (70) [solid red lines]. The black dots are reference points extracted from the data, which are used in the fitting of $\tilde{L}_\Gamma(B)\cos(2\pi\mathcal{F}_-)$. The best fittings were produced by assuming Gaussian broadening, namely.

$$\tilde{L}_\Gamma(B) = \exp\left(-2\pi^2\frac{\Gamma^2}{(\hbar\omega_c)^2} \right) = \exp\left(-\frac{B_q^2}{B^2} \right), \quad (73)$$

where $B_q = \sqrt{2}\pi\frac{m^*\Gamma}{\hbar e}$ and Γ is a constant Landau level broadening.
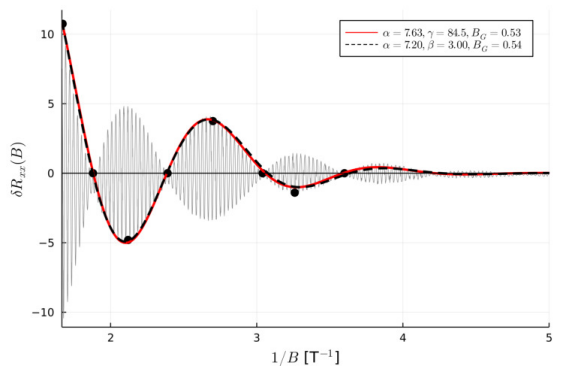
FIG. 17. The black dots are reference points for curve C1, solid black line. The black dashed curve is the linear Dresselhaus result and solid red curve $full$ Dresselhaus result. Parameter values from fitting are shown in the inset. Other parameters[41] are $m^* = 0.019$, $g = -12$ and $n_{2\mathrm{D}} = 0.0176\,\mathrm{nm}^{-2}$.

FIG. 18. Similar to Fig. (17), but for curve C5, solid black line. The black dashed curve represents the linear Dresselhaus result, while the solid red curve, the $full$ cubic Dresselhaus term. Extracted fitting parameters are shown in the inset. Other parameters[41] are $m^* = 0.019$, $g = -12$ and $n_{2\mathrm{D}} = 0.0176\,\mathrm{nm}^{-2}$.

For curve C1 in Fig. 17 the fitting with linear Dresselhaus yields values $\alpha = 7.2\,\mathrm{meV\,nm}$ and $\beta = 3.0\,\mathrm{meV\,nm}$. On the other hand, for fitting to the $full$ model we obtain $\alpha = 7.6\,\mathrm{meV\,nm}$, and $\gamma = 85\,\mathrm{meV\,nm^3}$. We see that both fits produce equally good curves fitting the experimental data points, with comparable values for the extracted Rashba SO coupling. This indicates that when the Rashba coupling dominates the cubic Dresselhaus term (a^3-term in Eq. (70)), fitting the data with the addition of the cubic term does not strongly affect the result. The results for curve C5 in Fig. 18 behave similarly, i.e. we find fitted values of the Rashba coefficient, $\alpha = 6.7\,\mathrm{meV\,nm}$ for the linear Dresselhaus with

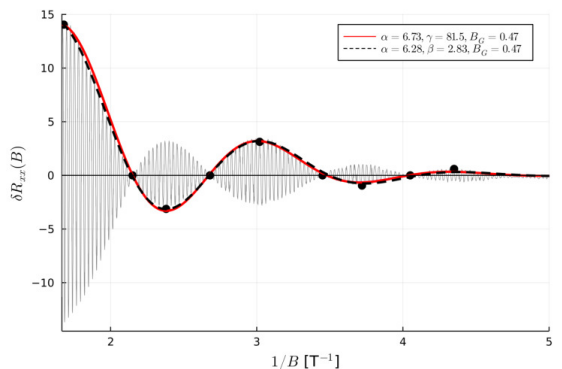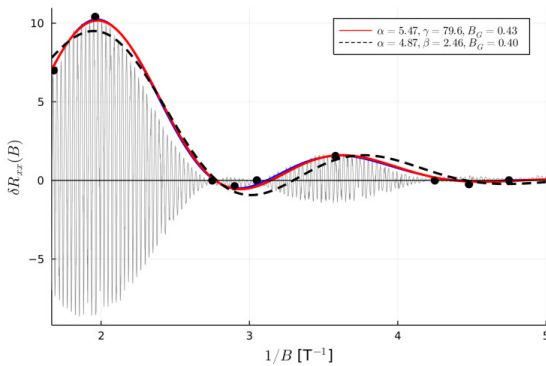FIG. 19. Similar to Fig. (17), but for curve C10, solid black line. The black dashed curve represents the linear Dresselhaus result, which fails to fit the data. However, the *full* cubic Dresselhaus term (solid red curve) results in a good fit. Extracted fitting parameters are shown in the inset. Other parameters[41] are $m^* = 0.019$, $g = -12$ and $n_{2D} = 0.0176\,\mathrm{nm}^{-2}$.

$\beta = 2.8\,\mathrm{meV\,nm}$, and $\alpha = 6.3\,\mathrm{meV\,nm}$ for the *full* cubic Dresselhaus, with $\gamma = 82\,\mathrm{meV\,nm}^3$.

However, the story is different for the curve C10 shown in Fig. 19. Here the value of Rashba and Dresselhaus coupling are closer, and then the details of the linear vs. cubic Dresselhaus become relevant. Indeed, the linear Dresselhaus model fitting yields $\alpha = 5.5\,\mathrm{meV\,nm}$ and $\beta = 2.5\,\mathrm{meV\,nm}$ while the cubic fit gives $\alpha = 4.9\,\mathrm{meV\,nm}$. More importantly the error in the linear fit is quite high, and the fit [black dashed curve] fails to describe the data points. However, the cubic model gives a good fit , with $\gamma = 80\,\mathrm{meV\,nm}^3$. This clearly shows the importance of the cubic contributions in samples with high density, where the Rashba and Dresselhaus contributions are of comparable magnitudes.

The fit results in Fig. 17-19 were done for $\langle k_z^2 \rangle = \pi^2/d_{QW}^2$ where $d_{QW} = 12.5\,\mathrm{nm}$[41]. To fully model the sample a self-consistent Poisson-Schrödinger calculation is required[7,46,65], which is beyond the scope of this work. We can however use different values of $\langle k_z^2 \rangle$, which *indirectly* emulate self-consistent potential details, i.e. increasing the value of $\langle k_z^2 \rangle$ suggests a stronger confinement in the InAs quantum well, and decreased value of $\langle k_z^2 \rangle$ would correspond to wavefunctions being less localized in the InAs quantum well.

In Fig. 20 the values of α, β_1, and β are shown as a function of $\langle k_z^2 \rangle$ from $0.75 \frac{\pi^2}{d_{QW}^2}$ to $1.25 \frac{\pi^2}{d_{QW}^2}$. The data from the three curves are indicated by different forms: C1: circle, C5: triangle, and C10: square. For each value of $\langle k_z^2 \rangle$, specific values of α β_1, and β are obtained from the fit. The fit results for α and β for each curve remain relatively insensitive to $\langle k_z^2 \rangle$-variations. Note that as $\langle k_z^2 \rangle$ varies β_1 changes quite rapidly via the fitted value of γ. This is to be expected since lower values $\langle k_z^2 \rangle$, correspond

to the electron leaking out the InAs quantum well γ into the GaSb, which has a higher bulk value of γ. For higher values of $\langle k_z^2 \rangle$ the system becomes more strongly confined in the InAs quantum well and the value of γ should tend to the value corresponding to bulk InAs.

The fact that the values of α and β change only slightly as function of $\langle k_z^2 \rangle$, as can be seen in Fig. 20, has important consequences on the fitting proceedure. For this reason a fitting with γ and $\langle k_z^2 \rangle$ *both* being independent fitting parameters can not be performed, since if $\beta_1 = \gamma \langle k_z^2 \rangle$ is the dominant contribution to the Dresselhaus couplings then there are multiple (infinite) solutions to the equation $\gamma \langle k_z^2 \rangle = $ const. and fitting the data with γ and $\langle k_z^2 \rangle$ independent will not converge[41].
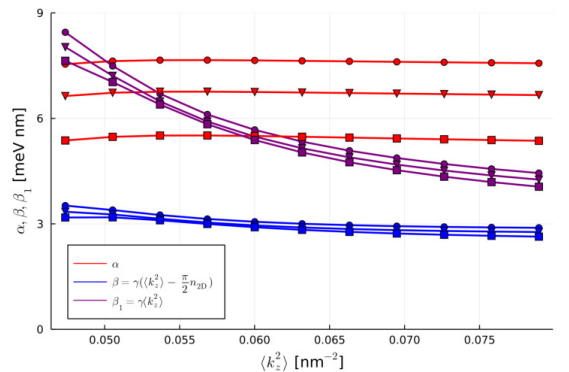
FIG. 20. The spin-orbit parameters that result from the fitting as a function of $\langle k_z^2 \rangle$. Other parameters are $m^* = 0.019$, $g = -12$ and $n_{2D} = 0.0176\,\mathrm{nm}^{-2}$. The three different symbols represent different curves: curve 1: circle, 5: triangle, and 10: square.

VII. SUMMARY

We investigated the SdH magneto-oscillations in the resistivity ρ_{xx} of 2DEGs in the presence of spin-orbit (Rashba-Dresselhaus) and Zeeman couplings. We used a semiclassical approach for the resistivity combined with a Poisson summation formula for the Landau-quantized DOS. Our approach allows for an intuitive separation of the slow and fast quantum oscillations in terms of "F-functions", central quantities in our description, essentially being the inverse functions of the spin-resolved Landau-level structure of the system. We study a variety of exact cases such as the pure Zeemann, pure Dresselhaus, and pure Rashba cases – all of which provide analytical expressions for the magnetoresistivity.

More importantly, from our unified and general formulation we also derive, for the first time, an analytical solution for the case with arbitrary Rashba and Dresselhaus couplings and simultaneous non-zero Zeeman coupling ($g^* \neq 0$).Interestingly, this allows us to derive a unique

new condition for the vanishing of the SO-induced beatings in the SdH signals: $\alpha/\beta = [(1 - \tilde{\Delta})/(1 + \tilde{\Delta})]^{1/2}$, where $\tilde{\Delta} = g^*m^*/2m_0$ (i.e., ratio (Zeeman energy)$/\hbar\omega_c$). This new condition does not correspond to any conserved quantity in our Hamiltonian, unlike the persistent-spin-helix condition $\alpha = \beta$ which is associated with the conservation of spin along some particular axes. We emphasize that our new condition precludes beatings in all harmonics of the quantum oscillations.

We have applied our analytical formulation to describe low-density data for SdH oscillations showing many harmonics in GaAs-based 2DEGs (see SM in Ref. 46) and found an excellent agreement, Fig. 2. We have also applied our theory to low-density InSb-based 2DEGs[15,39]. In addition, we have also developed a detailed numerical calculation for high-density InAs-based 2DEGs, in which an analytical description is not satisfactory. We find excellent agreement with available data for high-density InAs-based 2DEGs[41,46]. We have also pointed out an inequivalence between the Rashba-dominated + Zeeman vs the Dresselhaus-dominate + Zeeman cases, with only the former showing beatings. This follows from a distinct interplay between the SO and Zeeman terms in these two regimes. We hope our detailed study and unified general formulation will stimulate furhter experimental investigations aiming at verifying our theoretical predictions.

Appendix A: Density of states and F-Functions

Here we follow closely the discussion (and notation) in Sec. 3.2.2 of the book *Semiclassical Physics* by Brack and Bhaduri[47].

For simplicity, we first consider the case with a discrete spectrum $\varepsilon_n = f(n)$, $n = 0, 1, 2, ...$ in which each level has a degeneracy $d_n = \tilde{D}(n)$, with $\tilde{D}(n)$ being an arbitrary function of n. Later on we will account for a (pseudo) spin index. As an example, we note that for the usual 2DEG Landau levels (LLs) (in the absence of both Zeeman or SO interaction), $\varepsilon_n = \hbar\omega_c(n + 1/2)$ and $d_n = AeB/h = \tilde{D}(n)$ (A: area of the 2DEG, $e > 0$); in this case, $d_n = \tilde{D}(n)$ denotes the LL degeneracy and is independent of n. This same Landau degeneracy holds in the presence of Zeeman and SO interactions. For later convenience, we define $D(n) = \tilde{D}(n)/A$ to be the level degeneracy per unit area [e.g., for LLs $D(n) = n_{LL}(B) = eB/h$]. As in Ref. 47, let $f(n)$ be an arbitrary monotonic function with a differentiable inverse $f^{-1}(x) = F(x)$, the relevant "F-function" in our discussion. In this case, because $f^{-1}(f(x)) = x = f(f^{-1}(x))$ it follows that $n = F(\varepsilon_n)$. Next we define the DOS of our system and relate it the to the F-function, which ultimately allows us to calculate the oscillatory part of the DOS relevant for our semiclassical transport calculation.

1.   Density of states without LL broadening

Quite generally we can define the DOS of our system as,

$$g(\varepsilon) = \frac{1}{A}\sum_{n=0}^{\infty}\tilde{D}(n)\delta(\varepsilon - \varepsilon_n). \tag{A1}$$

Note that the above DOS is defined per area and energy. In Ref.[47] the DOS is defined just per energy. Motivated by the property $\delta[y(x)] = \frac{1}{|y'(x_0)|}\delta(x - x_0)$ where x_0 denotes a root of $y(x)$, i.e., $y(x_0) = 0$ and $y'(x) = dy(x)/dx$, we define $h(\varepsilon) = n - F(\varepsilon)$, which obeys $h(\varepsilon_n) = 0$ as $n = F(\varepsilon_n)$ by construction. We can then write

$$\delta[h(\varepsilon)] = \delta(n - F(\varepsilon)) = \frac{1}{|F'(\varepsilon_n)|}\delta(\varepsilon - \varepsilon_n) = \frac{1}{|F'(\varepsilon)|}\delta(\varepsilon - \varepsilon_n), \tag{A2}$$

or

$$\delta(\varepsilon - \varepsilon_n) = |F'(\varepsilon)|\delta(n - F(\varepsilon)). \tag{A3}$$

Substituting (A3) into (A1), we find

$$g(\varepsilon) = D(\varepsilon)|F'(\varepsilon)|\sum_{n=0}^{\infty}\delta(n - F(\varepsilon)), \tag{A4}$$

where $D(\varepsilon) \equiv D(F(\varepsilon))$. Noting that

$$\sum_{n=0}^{\infty} \delta(\varepsilon - n) = \sum_{l=-\infty}^{\infty} e^{2\pi i l \varepsilon}, \qquad (\varepsilon > 0) \qquad \text{(A5)}$$

we can straightforwardly cast (A4) in the form

$$g(\varepsilon) = D(\varepsilon)|F'(\varepsilon)| \sum_{l=-\infty}^{\infty} e^{2\pi i l F(\varepsilon)}. \qquad \text{(A6)}$$

Now we introduce the (pseudo) spin index $s = \pm 1$ by adding a subscript s to all quantities [except $D(\varepsilon)$ for it is not (pseudo) spin dependent]. This s index accounts for the spin-dependent Zeeman and SO interactions in our 2DEG. With this new index, the DOS in Eq. (A5), viewed as per spin now, becomes

$$g_s(\varepsilon) = D(\varepsilon)|F'_s(\varepsilon)| \sum_{l=-\infty}^{\infty} e^{2\pi i l F_s(\varepsilon)}, \qquad \text{(A7)}$$

or

$$g_s(\varepsilon) = D(\varepsilon)|F'_s(\varepsilon)| \left\{ 1 + 2\sum_{l=1}^{\infty} \cos[2\pi l F_s(\varepsilon)] \right\}. \qquad (\varepsilon > 0) \qquad \text{(A8)}$$

By summing over s, we obtain the total DOS,

$$g(\varepsilon) = D(\varepsilon) \sum_s |F'_s(\varepsilon)| \left\{ 1 + 2\sum_{l=1}^{\infty} \cos[2\pi l F_s(\varepsilon)] \right\}. \qquad \text{(A9)}$$

For the systems investigated in our work, $F'_s(\varepsilon) \simeq 1/\hbar\omega_c$. This is actually exact for the Zeeman-only case, see Eq. (28), main text, but only approximate in the presence of SO interaction [see Eq. (A38)]. In this case and $D(\varepsilon)|F'_s(\varepsilon)| = \frac{m^*}{2\pi\hbar^2}$, we find

$$g(\varepsilon) \simeq \frac{m^*}{\pi\hbar^2} \left\{ 1 + \sum_{l=1}^{\infty} \left(\cos[2\pi l F_+(\varepsilon)] + \cos[2\pi l F_-(\varepsilon)] \right) \right\}. \qquad \text{(A10)}$$

Using the identity,

$$\cos a + \cos b = 2\cos[(a+b)/2]\cos[(a-b)/2], \qquad \text{(A11)}$$

we can rewrite Eq. (A10) as

$$g(\varepsilon) \simeq \frac{m^*}{\pi\hbar^2} \left\{ 1 + \sum_{l=1}^{\infty} 2\cos[2\pi l \mathcal{F}_+(\varepsilon)]\cos[2\pi l \mathcal{F}_-(\varepsilon)] \right\}, \qquad \text{(A12)}$$

where

$$\mathcal{F}_{\pm}(\varepsilon) = \frac{1}{2}[F_+(\varepsilon) \pm F_-(\varepsilon)]. \qquad \text{(A13)}$$

To regain the DOS notation in the main text, we now make $g(\varepsilon) \rightarrow \mathcal{D}(\varepsilon, B)$ and use $\mathcal{D}_0 = \frac{m^*}{2\pi\hbar^2}$. Hence,

Eq. (A12) becomes

$$\mathcal{D}(\varepsilon, B) \simeq 2\mathcal{D}_0 \left\{ 1 + 2\sum_{l=1}^{\infty} \cos[2\pi l \mathcal{F}_+(\varepsilon)]\cos[2\pi l \mathcal{F}_-(\varepsilon)] \right\}, \qquad \text{(A14)}$$

or

$$\frac{\mathcal{D}(\varepsilon, B) - 2\mathcal{D}_0}{2\mathcal{D}_0} \simeq 2\sum_{l=1}^{\infty} \cos[2\pi l \mathcal{F}_+(\varepsilon)]\cos[2\pi l \mathcal{F}_-(\varepsilon)], \qquad \text{(A15)}$$

which is Eq. (14) in the main text.

2. Density of states including Landau level broadening

We can account for LL broadening in the DOS calculation by considering Lorentzian or Gaussian functions as particular representations of the ideal δ functions describing the discrete levels. We consider a simple phenomenological description which assumes that all LLs have the same spin-independent broadening Γ.

a. Lorentzian DOS case

Here we take the delta function representing the DOS of a single LL as,

$$\delta(\varepsilon - \varepsilon_n) = \lim_{\Gamma \to 0} \frac{1}{\pi} \frac{\Gamma/2}{(\varepsilon - \varepsilon_n)^2 + (\Gamma/2)^2} = \lim_{\Gamma \to 0} L_\Gamma(\varepsilon - \varepsilon_n), \qquad \text{(A16)}$$

where

$$L_\Gamma(\varepsilon) = \frac{1}{\pi} \frac{\Gamma/2}{\varepsilon^2 + (\Gamma/2)^2}, \qquad \text{(A17)}$$

with

$$\int_{-\infty}^{\infty} L_\Gamma(\varepsilon) d\varepsilon = 1. \qquad \text{(A18)}$$

Note that

$$\int_{-\infty}^{\infty} L_\Gamma(\varepsilon) e^{-2\pi i l \varepsilon} d\varepsilon = e^{-\Gamma\pi|l|} = \tilde{L}_\Gamma(k), \qquad \text{(A19)}$$

where $\tilde{L}_\Gamma(k)$ is the Fourier transform (FT) of $L_\Gamma(\varepsilon)$ and $l \in \mathbb{Z}$. Using the shifting property of FTs, it follows that the FT of $L_\Gamma(\varepsilon - x)$ is $e^{-2\pi i k x}\tilde{L}_\Gamma(k)$. Generalizing Eq. (A1) for Lorentzian-broadened levels we have (we will add a subindex s later on)

$$g(\varepsilon) = \lim_{\Gamma \to 0} \sum_{n=0}^{\infty} D(n) L_\Gamma(\varepsilon - \varepsilon_n), \qquad \text{(A20)}$$

which we can rewrite as,

$$g(\varepsilon) = \lim_{\Gamma \to 0} \sum_{n=0}^{\infty} \int_{-\infty}^{\infty} D(n) L_\Gamma(\varepsilon - x) \delta(x - \varepsilon_n) dx. \quad (A21)$$

Considering that $D(n)$ is independent of n and using Eq. (A5) with the replacement $\varepsilon \to F(\varepsilon)$, we obtain

$$g(\varepsilon) = \lim_{\Gamma \to 0} \int_{-\infty}^{\infty} D(F(x))|F'(x)| \sum_{l=-\infty}^{\infty} e^{2\pi i l F(x)} L_\Gamma(\varepsilon - x) dx. \quad (A22)$$

Since $L_\Gamma(\varepsilon - x) = L_\Gamma(x - \varepsilon)$ is peaked at $x = \varepsilon$, it is convenient to expand $F(x)$ around this point. Then $g(\varepsilon)$ becomes

$$g(\varepsilon) = \lim_{\Gamma \to 0} \int_{-\infty}^{\infty} D[F(\varepsilon) + |F'(\varepsilon)|(x - \varepsilon)][|F'(\varepsilon)| +$$

$$|F''(\varepsilon)|(x - \varepsilon)] \sum_{l=-\infty}^{\infty} e^{2\pi i l [F(\varepsilon) + |F'(\varepsilon)|(x - \varepsilon)]} L_\Gamma(\varepsilon - x) dx. \quad (A23)$$

Neglecting the contribution $|F''(\varepsilon)|(x - \varepsilon)$ [as a matter of fact, this contribution vanishes identically in the limit $L_\Gamma(x - \varepsilon) \to \delta(x - \varepsilon)$, because $\int_{-\infty}^{\infty} f(x)\delta(x - x_0)dx = f(x_0)$], we have

$$g(\varepsilon) = D(\varepsilon) \lim_{\Gamma \to 0} |F'(\varepsilon)| \sum_{l=-\infty}^{\infty} e^{2\pi i l F(\varepsilon)} \times$$

$$\int_{-\infty}^{\infty} e^{2\pi i l |F'(\varepsilon)|(x - \varepsilon)} L_\Gamma(x - \varepsilon) d(x - \varepsilon). \quad (A24)$$

Using Eq. (A19), we can write

$$g(\varepsilon) = D(\varepsilon) \lim_{\Gamma \to 0} |F'(\varepsilon)| \sum_{l=-\infty}^{\infty} e^{2\pi i l F(\varepsilon)} \tilde{L}_\Gamma(l|F'(\varepsilon)|). \quad (A25)$$

or

$$g(\varepsilon) = D(\varepsilon) \lim_{\Gamma \to 0} |F'(\varepsilon)| \sum_{l=-\infty}^{\infty} e^{2\pi i l F(\varepsilon)} e^{-\Gamma \pi |l F'(\varepsilon)|}, \quad (A26)$$

where have used,

$$\tilde{L}_\Gamma(l|F'(\varepsilon)|) = e^{-\Gamma \pi |l F'(\varepsilon)|} \quad (A27)$$

As before [Eq. (A7)], we can rewrite Eq. (A26) by adding a subindex s to obtain the LL-broadened DOS per spin

$$g_s(\varepsilon) = D(\varepsilon)|F'_s(\varepsilon)| \left\{ 1 + 2 \sum_{l=1}^{\infty} \cos[2\pi l F_s(\varepsilon)] e^{-\Gamma \pi l |F'_s(\varepsilon)|} \right\}. \quad (A28)$$

In the above we have dropped the $\lim_{\Gamma \to 0}$, since a real system has a finite Γ. Interestingly, the broadened DOS in Eq. (A28) can be obtained directly from the case with-

out broadening [Eq. (A8)] by simply multiplying the oscillating components (harmonics) in the latter by the exponential ("Dingle") factor $e^{-\Gamma \pi l |F'_s(\varepsilon)|}$.

Here again, for the systems of interest here $F'_s(\varepsilon) \simeq 1/\hbar\omega_c$ and the exponential factor in Eq. (A28) becomes

$$e^{-\Gamma \pi l |F'_s(\varepsilon)|} = e^{-\pi l \Gamma / \hbar\omega_c}, \quad (A29)$$

where $\Gamma \equiv \hbar/\tau_q$, τ_q is the quantum lifetime of the LL. Summing over the (pseudo) spin index s Eq. (A28) becomes

$$g(\varepsilon) = \frac{m^*}{\pi\hbar^2} \left\{ 1 + 2 \sum_{l=1}^{\infty} \cos[2\pi l \mathcal{F}_+(\varepsilon)] \cos[2\pi l \mathcal{F}_-(\varepsilon)] e^{-\frac{\pi l \Gamma}{\hbar\omega_c}} \right\}. \quad (A30)$$

In the notation of the main text we have

$$\frac{\mathcal{D}(\varepsilon, B) - 2\mathcal{D}_0}{2\mathcal{D}_0} \simeq 2 \sum_{l=1}^{\infty} \cos[2\pi l \mathcal{F}_+(\varepsilon)] \cos[2\pi l \mathcal{F}_-(\varepsilon)] e^{-\frac{\pi l \Gamma}{\hbar\omega_c}}, \quad (A31)$$

which is the Eq. (22) of the main text, but written for the Lorentzian broadening case.

b. Gaussian DOS case

The Gaussian-broadened case can be treated similarly by considering the delta function representation

$$\delta(\varepsilon - \varepsilon_n) = \lim_{\Gamma \to 0} \frac{1}{\sqrt{2\pi}\Gamma} e^{-\frac{(\varepsilon - \varepsilon_n)^2}{2\Gamma^2}}. \quad (A32)$$

From this we can evaluate the integral in Eq. (A19) which results in the Gaussian version of Eq. (A27):

$$\tilde{L}_\Gamma(l|F'(\epsilon)|) = e^{-2\pi^2 (l|F'(\epsilon)|)^2 \Gamma^2}. \quad (A33)$$

This reduces to Eq. (73) for $l = 1$ (fundamental frequency) and $|F'(\epsilon)| = 1/\hbar\omega_c$.

c. Calculating the F-function and its derivative $F'(\varepsilon)$

Here we illustrate the calculation of $F_s(\varepsilon)$ and its derivative with respect to ε, $F'(\varepsilon)$, in the presence of SO interaction. For simplicity, we consider the pure Rashba case (no Zeeman). To determine the F-functions we need to invert $\varepsilon_{n,s} = \varepsilon$, where

$$\frac{\varepsilon_{n,s}}{\hbar\omega_c} = \left(n + \frac{1}{2} + \frac{s}{2} \right) \quad (A34)$$

$$- \frac{s}{2} \frac{1 - \tilde{\Delta}}{|1 - \tilde{\Delta}|} \sqrt{\left(1 - \tilde{\Delta}\right)^2 + 16\alpha_B^2 \left(n + \frac{1}{2} + \frac{s}{2}\right)},$$

is the pure Rashba energy, Eq. (33) in the main text. Squaring $\varepsilon - \tilde{n}\hbar\omega_c$, with $\tilde{n} = n + (1+s)/2$, we find

$$[\varepsilon - \tilde{n}\hbar\omega_c]^2 = \frac{1}{4}(\hbar\omega_c - \Delta)^2 + 4\varepsilon_R\hbar\omega_c\tilde{n}$$

$$\varepsilon^2 - 2\varepsilon\hbar\omega_c\tilde{n} + \tilde{n}^2\hbar^2\omega_c^2 = \frac{1}{4}(\hbar\omega_c - \Delta)^2 + 4\varepsilon_R\hbar\omega_c\tilde{n}$$

$$\tilde{n}^2\hbar^2\omega_c^2 - (2\varepsilon\hbar\omega_c + 4\varepsilon_R\hbar\omega_c)\tilde{n} - \frac{1}{4}(\hbar\omega_c - \Delta)^2 + \varepsilon^2 = 0$$

$$\tilde{n}^2 - \left(\frac{2\varepsilon}{\hbar\omega_c} + \frac{4\varepsilon_R}{\hbar\omega_c}\right)\tilde{n} - \left(\frac{1}{2} - \frac{\Delta}{2\hbar\omega_c}\right)^2 + \left(\frac{\varepsilon}{\hbar\omega_c}\right)^2 = 0 \quad (A35)$$

We can easily solve (A35) for $\tilde{n}_s(\varepsilon) \Rightarrow n_s(\varepsilon) = -(1+s)/2 + \tilde{n}_s(\varepsilon) = f_s^{-1} = F_s(\varepsilon)$

$$F_s(\varepsilon) = -\frac{1+s}{2} + \frac{\varepsilon}{\hbar\omega_c} + \frac{2\varepsilon_R}{\hbar\omega_c} \quad\quad (A36)$$
$$+ s\sqrt{\left(\frac{\varepsilon}{\hbar\omega_c} + \frac{2\varepsilon_R}{\hbar\omega_c}\right)^2 + \left(\frac{1}{2} - \frac{\Delta}{2\hbar\omega_c}\right)^2 - \left(\frac{\varepsilon}{\hbar\omega_c}\right)^2}.$$

We obtain $F'_\pm(\varepsilon)$ by differentiating (A37),

$$F'_s(\varepsilon) = \frac{1}{\hbar\omega_c} + s\frac{1}{2}\frac{2\left(\frac{\varepsilon}{\hbar\omega_c} + \frac{2\varepsilon_R}{\hbar\omega_c}\right)\frac{1}{\hbar\omega_c} - \frac{2\varepsilon}{\hbar^2\omega_c^2}}{\sqrt{\left(\frac{\varepsilon}{\hbar\omega_c} + \frac{2\varepsilon_R}{\hbar\omega_c}\right)^2 + \left(\frac{1}{2} - \frac{\Delta}{2\hbar\omega_c}\right)^2 - \left(\frac{\varepsilon}{\hbar\omega_c}\right)^2}}$$

$$\quad (A37)$$

or

$$F'_s(\varepsilon) = \frac{1}{\hbar\omega_c} + s\frac{\frac{2\varepsilon_R}{\hbar\omega_c}}{\sqrt{\frac{4\varepsilon\varepsilon_R}{\hbar^2\omega_c^2} + \left(\frac{2\varepsilon_R}{\hbar\omega_c}\right)^2 + \left(\frac{1}{2} - \frac{\Delta}{2\hbar\omega_c}\right)^2}}. \quad (A38)$$

As mentioned earlier, the leading term in $F'_s(\varepsilon)$ is $1/\hbar\omega_c$. By expanding the above expression, we can easily find $\mathcal{O}(\varepsilon_R/\varepsilon_F) = \mathcal{O}[(\alpha m^*\ell_c)^2/\hbar]$ corrections. The above calculation also holds for the Dresselhaus case. The general case with simultaneous and arbitrary Rashba and Dresselhaus couplings lead to the corrections $\mathcal{O}[(\alpha m^*\ell_c)^2/\hbar] + \mathcal{O}[(\beta m^*\ell_c)^2/\hbar)]$ mentioned following Eq. (12).

Appendix B: Orthogonal subspaces $\mathcal{P}$

When both Rashba and Dresselhaus are present neither $\mathcal{N}_+$ nor $\mathcal{N}_-$ are conserved, i.e. $[\mathcal{N}_\pm, \tilde{\mathcal{H}}] \neq 0$. This will result in mixing of states, e.g. the pure Rashba states will get couple to each other when a finite β is introduced, and vice versa. However, there is a conserved quantity that can be constructed from $\mathcal{N}_\pm$ by defining[51,52]

$$\mathcal{P}_\pm = \exp(i\pi(\mathcal{N}_\pm + 1/2)). \quad (B1)$$

Using the definition of $\mathcal{N}_+ = a^\dagger a + \frac{1}{2}\sigma_z$ we can show that

$$\mathcal{P}_+ = \exp\left(i\pi(a^\dagger a + \frac{1}{2}\sigma_z)\right) = \exp\left(i\pi(a^\dagger a - \frac{1}{2}\sigma_z + \sigma_z)\right)$$
$$= \mathcal{P}_- \exp(i\pi\sigma_z) = -\mathcal{P}_-, \quad (B2)$$

where we used $\exp(i\pi\sigma_z) = -1$. Since $\mathcal{P}_\pm$ have eigenvalue ± 1, we only need to consider $\mathcal{P} = \mathcal{P}_+ = -\mathcal{P}_-$. First, we look at how the operator $\mathcal{P}$ affects the operators a, and σ_+:

$$\mathcal{P}\sigma_+\mathcal{P}^\dagger = e^{i\frac{\pi}{2}\sigma_z}\sigma_+ e^{-i\frac{\pi}{2}\sigma_z} = e^{i\pi}\sigma_+ = -\sigma_+ \quad (B3)$$
$$\mathcal{P}a\mathcal{P}^\dagger = e^{i\pi a^\dagger a}a e^{-i\pi a^\dagger a} = e^{i\pi}a = -a \quad (B4)$$

The Hamiltonians in both Eqs. (9) and Eq. (70) contain diagonal terms ($a^\dagger a$ and σ_z) that commute with $\mathcal{P}$, and non-diagonal terms that involve *odd* power $a, a^\dagger$ multiplying σ_+, σ_-, so then its straightforward to show that $[\mathcal{H}, \mathcal{P}] = 0$. Note that $\mathcal{P}$ is unitary so the condition $[\mathcal{H}, \mathcal{P}] = 0$, can be rewritten as $\mathcal{P}\mathcal{H}\mathcal{P}^\dagger = \mathcal{H}$. Focusing on the spin-orbit part of Eq. (9) one obtains

$$\mathcal{P}\left(\alpha_B a^\dagger\sigma_- + \beta_B a^\dagger\sigma_+\right)\mathcal{P}^\dagger + \text{h.c.}$$
$$= (\alpha_B\mathcal{P}a^\dagger\mathcal{P}^\dagger\mathcal{P}\sigma_-\mathcal{P}^\dagger + \beta_B\mathcal{P}a^\dagger\mathcal{P}^\dagger\mathcal{P}\sigma_+\mathcal{P}^\dagger) + \text{h.c.}$$
$$= (\alpha_B(-a^\dagger)(-\sigma_-) + \beta_B(-a^\dagger)(-\sigma_+)) + \text{h.c.}$$
$$= \left(\alpha_B a^\dagger\sigma_- + \beta_B a^\dagger\sigma_+\right) + \text{h.c.}, \quad (B5)$$

which shows that $\mathcal{P}\mathcal{H}\mathcal{P}^\dagger = \mathcal{H}$, since the diagonal terms in $\mathcal{H}$ trivially commute with $\mathcal{P}$.

The practical results of having a diagonal operator $\mathcal{P}$ that commutes with $\mathcal{H}$ is that the Hamiltonian can be diagonalized using two *separate* sets of basis states:

$$\mathcal{P} = +1: \quad \{|0,\uparrow\rangle, |1,\downarrow\rangle, |2,\uparrow\rangle, |3,\downarrow\rangle, |4,\uparrow\rangle, \dots\}$$
$$\mathcal{P} = -1: \quad \{|0,\downarrow\rangle, |1,\uparrow\rangle, |2,\downarrow\rangle, |3,\uparrow\rangle, |4,\downarrow\rangle, \dots\}$$

Diagonalizing $\mathcal{H}$ in either of the $\mathcal{P} = +1$, or -1, subspaces will result in a set of states that all anticross. We can connect these sets of states to $\mathcal{N}_+$ eigenstates

$$\mathcal{P} = +1: \quad \{\overbrace{|0,\uparrow\rangle, \underbrace{|1,\downarrow\rangle}, |2,\uparrow\rangle}^{|0,+\rangle,|1,-\rangle}, \overbrace{|3,\downarrow\rangle}^{|2,+\rangle,|3,-\rangle}, |4,\uparrow\rangle, \dots\}$$
$$\mathcal{P} = -1: \quad \{|0,\downarrow\rangle, \underbrace{|1,\uparrow\rangle, |2,\downarrow\rangle}_{|1,+\rangle,|2,-\rangle}, \underbrace{|3,\uparrow\rangle, |4,\downarrow\rangle}_{|3,+\rangle,|4,-\rangle}, \dots\},$$

and similarly for the $\mathcal{N}_-$ eigenstates

$$\mathcal{P} = +1: \quad \{|0,\uparrow\rangle, \overbrace{|1,\downarrow\rangle, |2,\uparrow\rangle}^{|1,-\rangle,|2,+\rangle}, \overbrace{|3,\downarrow\rangle, |4,\uparrow\rangle}^{|3,-\rangle,|4,+\rangle}, \dots\}$$
$$\mathcal{P} = -1: \quad \{\underbrace{|0,\downarrow\rangle, |1,\uparrow\rangle}_{|0,-\rangle,|1,+\rangle}, \underbrace{|2,\downarrow\rangle, |3,\uparrow\rangle}_{|2,-\rangle,|3,+\rangle}, |4,\downarrow\rangle, \dots\}$$

Note that $\mathcal{P}$ also commutes with the cubic Dresselhaus terms as is discussed in App. C.

Appendix C: Cubic Dresselhaus

The Hamiltonian in Eq. (9) describes a 2DEG with both Rashba and *linear* Dresselhaus. For the numerical part we also include the *full* cubic Dresselhaus contribution. Starting from Eq. (6.1) in Ref. 50, and projecting

down to the lowest transverse level results in

$$\mathcal{H}_{D3} = \frac{(-\gamma\langle k_z^2\rangle)}{\hbar}\left(\left[\frac{1}{2}\Pi_+\sigma_+ -\frac{1}{8\hbar^2\langle k_z^2\rangle}\{\Pi_+^2-\Pi_-^2,\Pi_-\}\right]+\text{h.c.}\right), \quad (C1)$$

where $\Pi_\pm = \Pi_x \pm i\Pi_y$, and $\langle\Pi_z^2\rangle = \hbar^2\langle k_z^2\rangle$. Note that now the Dresselhaus spin-orbit coupling is parametrized by two parameters γ and $\langle k_z^2\rangle$, while for the linear approximation, only the single parameter $\beta = (-\gamma)\langle k_z^2\rangle$ is required. Using the definition in Eqs. (3) and (4) the full Dresselhaus Hamiltonian becomes

$$\mathcal{H}_{D3} = \frac{(-\gamma\langle k_z^2\rangle)}{\hbar}\left\{\left[\left(1-\frac{1}{2\langle k_z^2\rangle\ell_c^2}a^\dagger a\right)a^\dagger\sigma_+ +\frac{1}{2\langle k_z^2\rangle\ell_c^2}a^3\sigma_+\right]+\text{h.c.}\right\}. \quad (C2)$$

In the absence of spin-orbit interaction $a^\dagger a$ can be replaced by its eigenvalue n, which in turn is related to the ratio of the Fermi energy and $\hbar\omega_c$ (valid for $\varepsilon_F \ll \hbar\omega_c$)

$$\frac{1}{\ell_c^2}a^\dagger a \to \frac{1}{\ell_c^2}n \approx \frac{1}{\ell_c^2}\frac{\varepsilon_F}{\hbar\omega_c} = \frac{k_F^2}{2} = \pi n_{2D}. \quad (C3)$$

In the presence of spin-orbit we can still formally rewrite Eq. (C2) as

$$\mathcal{H}_{D3} = \frac{(-\gamma)\left(\langle k_z^2\rangle-\frac{\pi}{2}n_{2D}\right)}{\hbar}\left\{\left[\frac{\langle k_z^2\rangle-\frac{1}{2\ell_c^2}a^\dagger a}{\langle k_z^2\rangle-\frac{\pi}{2}n_{2D}}a^\dagger\sigma_+ +\frac{1}{2\ell_c^2}\frac{1}{\langle k_z^2\rangle-\frac{\pi}{2}n_{2D}}a^3\sigma_+\right]+\text{h.c.}\right\}. \quad (C4)$$

The prefactor $-\gamma\left(\langle k_z^2\rangle-\frac{\pi}{2}n_{2D}\right)$ is *defined* as

$$\beta = \beta_1 - \beta_3$$
$$= \left[(-\gamma)\langle k_z^2\rangle\right] - \left[(-\gamma)\frac{\pi}{2}n_{2D}\right], \quad (C5)$$

which reduces to the traditional definition of β for low density samples as considered in Sec. V.

The parity operator $\mathcal{P}$ introduced in App. B also commutes with the Hamiltonian in Eq. (C2), since the spin-orbit terms involve odd powers of $a, a^\dagger$ multiplied by either σ_+ or σ_-, and the sign introduced the unitary transformation gets cancelled.

Appendix D: The numerical procedure for finding the F-function

For fixed parameter values, the eigenenergies of the Hamiltonian Eq. (9) take discrete values. They are obtained numerically by diagonalizing the Hamiltonian matrix using a large enough set of basis states. Finding the F-function as described in Eq. (11) is equivalent to a root

finding problem for the function

$$g_s(n) = \varepsilon_{n,s}(B) - \varepsilon_F = 0. \quad (D1)$$

This requires the quantum number n to be a continuous variable. which leads to a minor modification of the Hamiltonian diagonlization procedure. The standard diagonalization proceedure is to construct a $2N_L$ matrix from N_L harmonic oscillator eigenstates, in addition to the spin degree of freedom. The Pauli matrices form 2×2 blocks that are coupled by the ladder operators a and $a^\dagger$, leading to block tri-diagonal matrix with 2×2 block matrices

$$h_{l,l} = (l-1)\begin{bmatrix} 1 & 0 \\ 0 & 1 \end{bmatrix} + \begin{bmatrix} \frac{1-\tilde{\Delta}}{2} & 0 \\ 0 & \frac{1+\tilde{\Delta}}{2} \end{bmatrix} \quad (D2)$$

$$h_{l,l+1} = \sqrt{l+1}\begin{bmatrix} 0 & 2\alpha_\beta \\ 2\beta_B & 0 \end{bmatrix}, \quad (D3)$$

where l runs from 1 to N_L (number of Landau levels used in the calculations). To obtain a continuous version of Eqs. (D2) and (D3) a variable x is added to the index l, resulting in

$$h_{l,l}(x) = (l+x-1)\begin{bmatrix} 1 & 0 \\ 0 & 1 \end{bmatrix} + \begin{bmatrix} \frac{1-\tilde{\Delta}}{2} & 0 \\ 0 & \frac{1+\tilde{\Delta}}{2} \end{bmatrix} (D4)$$

$$h_{l,l+1}(x) = \sqrt{l+x+1}\begin{bmatrix} 0 & 2\alpha_\beta \\ 2\beta_B & 0 \end{bmatrix}. \quad (D5)$$

The full block-tridiagonal matrix based on the submatrices in Eqs. (D4) and (D5) will then yield a spectrum $\varepsilon_{n+x,s}$, for $x \in [-1,1]$. To further simply the calculations the basis states can be split into $\mathcal{P} = \pm 1$ subspaces. Each $\mathcal{P}$-subspace contains ordered states $\{\epsilon_{0+x},\epsilon_{1+x},\dots\}$. For each subspace, one chooses the two adjacent eigenenergies determined by the condition $\epsilon_{n+x} < \frac{\varepsilon_F}{\hbar\omega_c} < \epsilon_{n+x+1}$. Subsequently the value of x is found by solving $g_s(n+x) = 0$.

Appendix E: Perturbation theory and "Bogoliubov-de Gennes Hamiltonian"

Here we solve the Hamiltonian Eq. (50) through a perturbative approach. As the Hamiltonian due to the spin-orbit terms are generally much smaller than the Hamiltonian corresponding to free electron gas, we rewrite Eq. (50) as

$$\frac{\tilde{\mathcal{H}}}{\hbar\omega_c} = \overbrace{a^\dagger a + \frac{1}{2} + \frac{\tilde{\Delta}}{2}\sigma_z}^{\mathcal{H}_0/\hbar\omega_c} + \overbrace{\gamma\left(a^\dagger + a\right)\sigma_x + i\delta\left(a - a^\dagger\right)\sigma_y}^{\mathcal{V}/\hbar\omega_c}$$
$$= \mathcal{H}_0/\hbar\omega_c + \mathcal{V}/\hbar\omega_c.$$

with corresponding unperturbed Hamiltonian and perturbation, $\mathcal{H}_0$ and $\mathcal{V}$, respectively. Using now the Schrieffer–Wolff transformation[66,67], defined by e^S, with the constraint $\mathcal{V} + [\mathcal{S},\mathcal{H}_0] = 0$, we obtain an effective

Hamiltonian given by $\mathcal{H}_{eff} = \mathcal{H}_0 + \frac{1}{2}[\mathcal{S},\mathcal{V}] + \mathcal{O}(\mathcal{V}^3)$. For our system we find $\mathcal{S} = \mathcal{S}_\gamma + \mathcal{S}_\delta$, with

$$\mathcal{S}_\gamma = -\frac{\gamma}{1-\tilde{\Delta}^2}\left\{a\left(\sigma_x + i\tilde{\Delta}\sigma_y\right) - a^\dagger\left(\sigma_x - i\tilde{\Delta}\sigma_y\right)\right\}, \tag{E1}$$

$$\mathcal{S}_\delta = -\frac{i\delta}{1-\tilde{\Delta}^2}\left\{a\left(\sigma_y - i\tilde{\Delta}\sigma_x\right) + a^\dagger\left(\sigma_y + i\tilde{\Delta}\sigma_x\right)\right\}, \tag{E2}$$

yielding

$$\frac{\tilde{\mathcal{H}}_{eff}}{\hbar\omega_c} = \frac{1}{2}\left(1+\tilde{\Delta}\sigma_z\right) - \Omega - \Lambda\sigma_z + (1-2\Lambda\sigma_z)\,a^\dagger a$$
$$+ \Gamma\left(aa + a^\dagger a^\dagger\right)\sigma_z, \tag{E3}$$

with

$$\Omega = \frac{(\gamma^2+\delta^2) + 2\delta\gamma\tilde{\Delta}}{1-\tilde{\Delta}^2}, \tag{E4}$$

$$\Lambda = \frac{(\gamma^2+\delta^2)\,\tilde{\Delta} + 2\delta\gamma}{1-\tilde{\Delta}^2}, \tag{E5}$$

$$\Gamma = \frac{\delta^2 - \gamma^2}{1-\tilde{\Delta}^2}\tilde{\Delta}. \tag{E6}$$

The Hamiltonian Eq. (E3) can be rewritten in the Bogoliubov-de Gennes form as

$$\frac{\tilde{\mathcal{H}}_{eff}}{\hbar\omega_c} = \frac{1}{2}(1+\tilde{\Delta}\sigma_z) - \Omega - \Lambda\sigma_z - \frac{1}{2}(1-2\Lambda\sigma_z)$$
$$+ \frac{1}{2}\begin{pmatrix} a^\dagger & a \end{pmatrix}\begin{bmatrix} 1-2\Lambda\sigma_z & 2\Gamma\sigma_z \\ 2\Gamma\sigma_z & 1-2\Lambda\sigma_z \end{bmatrix}\begin{pmatrix} a \\ a^\dagger \end{pmatrix}, \tag{E7}$$

which can be diagonalized by a 2×2 Bogoliubov-de Gennes transformation, and reads

$$\frac{\tilde{\mathcal{H}}_{eff}}{\hbar\omega_c} = \frac{1}{2}(1+\tilde{\Delta}\sigma_z) - \Omega - \Lambda\sigma_z - \frac{1}{2}(1-2\Lambda\sigma_z) + \frac{1}{2}\begin{pmatrix} \tilde{a}^\dagger & \tilde{a} \end{pmatrix}\begin{bmatrix} \sqrt{(1-2\Lambda\sigma_z)^2 - 4\Gamma^2} & 0 \\ 0 & \sqrt{(1-2\Lambda\sigma_z)^2 - 4\Gamma^2} \end{bmatrix}\begin{pmatrix} \tilde{a} \\ \tilde{a}^\dagger \end{pmatrix}, \tag{E8}$$

with the diagonal operators $\tilde{a}$ and $\tilde{a}^\dagger$. For most semiconductors, we have $\Omega, \Lambda, \Gamma \ll 1$. By neglecting the fourth order or higher spin-orbit terms, i.e., $\delta^i\gamma^j$ with $i+j \geq 4$, we obtain

$$\frac{\tilde{\mathcal{H}}_{eff}}{\hbar\omega_c} = \frac{\tilde{\Delta}}{2}\sigma_z + |1-2\Lambda\sigma_z|\left(\tilde{a}^\dagger\tilde{a} + \frac{1}{2}\right) - \Omega \tag{E9}$$

with energies

$$\frac{\varepsilon_{l,s}}{\hbar\omega_c} = \frac{s}{2}\tilde{\Delta} - \Omega + |1-2\Lambda s|\left(l + \frac{1}{2}\right). \tag{E10}$$

For $1-2\Lambda > 0$ we obtain

$$\frac{\varepsilon_{l,s}}{\hbar\omega_c} = \left(l + \frac{1}{2} + \tilde{\Delta}\frac{s}{2}\right) - 2s\Lambda\left(l + \frac{1}{2}\right) - \Omega, \tag{E11}$$

which is Eq. (53) in the main text.

Appendix F: Approximations leading to Eqs. (58) and (59)

Starting from Eq. (57) one can obtain the the F-function by inverting the energy levels to obtain l, for each value of s. The resulting equations are

$$\mathcal{F}_+ = \frac{\varepsilon}{\hbar\omega_c} - \frac{1}{2} + |\Lambda|\left(1 - \frac{\Lambda}{|\Lambda|}\tilde{\Delta}\right) + \frac{1}{4}\frac{\Lambda}{|\Lambda|}\frac{1 - \frac{\Lambda}{|\Lambda|}\tilde{\Delta}}{\left|1 - \frac{\Lambda}{|\Lambda|}\tilde{\Delta}\right|}\sqrt{\left(1 - \frac{\Lambda}{|\Lambda|}\tilde{\Delta}\right)^2 + 8\left(1 - \frac{\Lambda}{|\Lambda|}\tilde{\Delta}\right)\left[\frac{\varepsilon}{\hbar\omega_c}|\Lambda| + \frac{|\Lambda|^2}{2}\left(1 - \frac{\Lambda}{|\Lambda|}\tilde{\Delta}\right) + \frac{1}{2}\left(\Omega\frac{\Lambda}{|\Lambda|} - \Lambda\right)\right]}$$

$$- \frac{1}{4}\frac{\Lambda}{|\Lambda|}\frac{1 - \frac{\Lambda}{|\Lambda|}\tilde{\Delta}}{\left|1 - \frac{\Lambda}{|\Lambda|}\tilde{\Delta}\right|}\sqrt{\left(1 - \frac{\Lambda}{|\Lambda|}\tilde{\Delta}\right)^2 + 8\left(1 - \frac{\Lambda}{|\Lambda|}\tilde{\Delta}\right)\left[\frac{\varepsilon}{\hbar\omega_c}|\Lambda| + \frac{|\Lambda|^2}{2}\left(1 - \frac{\Lambda}{|\Lambda|}\tilde{\Delta}\right) - \frac{1}{2}\left(\Omega\frac{\Lambda}{|\Lambda|} - \Lambda\right)\right]} \tag{F1}$$

$$\mathcal{F}_- = -\frac{1}{2}\frac{\Lambda}{|\Lambda|} + \frac{1}{4}\frac{\Lambda}{|\Lambda|}\frac{1 - \frac{\Lambda}{|\Lambda|}\tilde{\Delta}}{\left|1 - \frac{\Lambda}{|\Lambda|}\tilde{\Delta}\right|}\sqrt{\left(1 - \frac{\Lambda}{|\Lambda|}\tilde{\Delta}\right)^2 + 8\left(1 - \frac{\Lambda}{|\Lambda|}\tilde{\Delta}\right)\left[\frac{\varepsilon}{\hbar\omega_c}|\Lambda| + \frac{|\Lambda|^2}{2}\left(1 - \frac{\Lambda}{|\Lambda|}\tilde{\Delta}\right) + \frac{1}{2}\left(\Omega\frac{\Lambda}{|\Lambda|} - \Lambda\right)\right]}$$

$$+ \frac{1}{4}\frac{\Lambda}{|\Lambda|}\frac{1 - \frac{\Lambda}{|\Lambda|}\tilde{\Delta}}{\left|1 - \frac{\Lambda}{|\Lambda|}\tilde{\Delta}\right|}\sqrt{\left(1 - \frac{\Lambda}{|\Lambda|}\tilde{\Delta}\right)^2 + 8\left(1 - \frac{\Lambda}{|\Lambda|}\tilde{\Delta}\right)\left[\frac{\varepsilon}{\hbar\omega_c}|\Lambda| + \frac{|\Lambda|^2}{2}\left(1 - \frac{\Lambda}{|\Lambda|}\tilde{\Delta}\right) - \frac{1}{2}\left(\Omega\frac{\Lambda}{|\Lambda|} - \Lambda\right)\right]} \tag{F2}$$

We will further simplify these equations by approximating Eqs. (F1) and (F2) up to second order in the spin-orbit parameters Λ and Ω (or fourth order in γ and δ). Accordingly, we rewrite these equations as

$$\mathcal{F}_+ = \frac{\varepsilon}{\hbar\omega_c} - \frac{1}{2} + |\Lambda|\left(1 - \frac{\Lambda}{|\Lambda|}\tilde{\Delta}\right)$$
$$+ \frac{1}{4}\frac{\Lambda}{|\Lambda|}\frac{1 - \frac{\Lambda}{|\Lambda|}\tilde{\Delta}}{\left|1 - \frac{\Lambda}{|\Lambda|}\tilde{\Delta}\right|}\left(\sqrt{A+B} - \sqrt{A-B}\right), \tag{F3}$$

$$\mathcal{F}_- = -\frac{1}{2}\frac{\Lambda}{|\Lambda|} + \frac{1}{4}\frac{\Lambda}{|\Lambda|}\frac{1 - \frac{\Lambda}{|\Lambda|}\tilde{\Delta}}{\left|1 - \frac{\Lambda}{|\Lambda|}\tilde{\Delta}\right|}\left(\sqrt{A+B} + \sqrt{A-B}\right), \tag{F4}$$

where $A = A_0 + A_1 + A_2$ and $B = B_1$, with

$$A_0 = \left(1 - \frac{\Lambda}{|\Lambda|}\tilde{\Delta}\right)^2, \tag{F5}$$

$$A_1 = 8\frac{\varepsilon}{\hbar\omega_c}|\Lambda|\left(1 - \frac{\Lambda}{|\Lambda|}\tilde{\Delta}\right), \tag{F6}$$

$$A_2 = 4|\Lambda|^2\left(1 - \frac{\Lambda}{|\Lambda|}\tilde{\Delta}\right)^2, \tag{F7}$$

$$B_1 = 4\left(1 - \frac{\Lambda}{|\Lambda|}\tilde{\Delta}\right)\left(\Omega\frac{\Lambda}{|\Lambda|} - \Lambda\right). \tag{F8}$$

Here, the nominal values of the subindices of A_i and B_j indicate their order on the spin-orbit terms Λ and Ω. Accordingly, we expand the square roots of Eqs. (F3) and (F4) and keep only terms up to second order in either Λ or Ω, yielding

$$\sqrt{A+B} + \sqrt{A-B} \approx 2\sqrt{A_0 + A_1}\left(1 + \frac{1}{2}\frac{A_2}{A_0 + A_1}\right),$$
$$= 2\sqrt{A_0 + A_1 + A_2} \tag{F9}$$

$$\sqrt{A+B} - \sqrt{A-B} \approx \frac{B_1}{\sqrt{A_0}}. \tag{F10}$$

As a consequence, we can finally write

$$\mathcal{F}_+ = \frac{\varepsilon}{\hbar\omega_c} - \frac{1}{2} + \Omega - \Lambda\tilde{\Delta} \tag{F11}$$

$$\mathcal{F}_- = -\frac{1}{2}\frac{\Lambda}{|\Lambda|} + \frac{1}{2}\frac{\Lambda}{|\Lambda|}\frac{1 - \frac{\Lambda}{|\Lambda|}\tilde{\Delta}}{\left|1 - \frac{\Lambda}{|\Lambda|}\tilde{\Delta}\right|} \times \sqrt{\left(1 - \frac{\Lambda}{|\Lambda|}\tilde{\Delta}\right)^2 + 8|\Lambda|\left(1 - \frac{\Lambda}{|\Lambda|}\tilde{\Delta}\right)\left[\frac{\varepsilon}{\hbar\omega_c} + \frac{1}{2}|\Lambda|\left(1 - \frac{\Lambda}{|\Lambda|}\tilde{\Delta}\right)\right]}, \tag{F12}$$

which are Eqs. (58) and (59), respectively.

Appendix G: Temperature dependence of the normalized differential resistivity

In this section we derive the general temperature dependence of the normalized differential magnetoresistiv-

ity in Eq. (24) for the systems studied in this work.

$$\delta\rho_{xx}(B) = 2\sum_{l=1}^{\infty} \int d\varepsilon \tilde{L}_\Gamma \left(l\frac{\Gamma}{\hbar\omega_c} \right) \left(-\frac{df_0(\varepsilon)}{d\varepsilon} \right)$$
$$\times \cos(2\pi l\mathcal{F}_-)\cos(2\pi l\mathcal{F}_+). \quad (G1)$$

At $T = 0$ K, we have $-df_0(\varepsilon)/d\varepsilon \to \delta(\varepsilon - \varepsilon_F)$, which simplifies Eq. (G1) to

$$\delta\rho_{xx}(B) = 2\sum_{l=1}^{\infty} \tilde{L}_\Gamma \left(l\frac{\Gamma}{\hbar\omega_c} \right)\cos(2\pi l\mathcal{F}_-)\cos(2\pi l\mathcal{F}_+)|_{\varepsilon = \varepsilon_F}, \quad (G2)$$

being obviously temperature independent. When the temperature is finite but small, i.e., $k_B T \ll \mu \sim \varepsilon_F$,

we have a temperature dependent $\delta\rho_{xx}(B)$. We now analyze the relevant case for low-density semiconductors, but with $\varepsilon_F \gg \varepsilon_R, \varepsilon_D$, and high number of populated Landau levels, i.e., $\varepsilon_F/\hbar\omega_c \gg 1$. With these conditions, all the different cases analyzed in this manuscript present $\mathcal{F}_\pm$-functions constant or linearly dependent on the energy, so we write here, $\mathcal{F}_\pm \propto \varepsilon + cte$, see, for example Eqs. (29), (44), (45), (58), and (59). Using $2\pi l\mathcal{F}_+ = 2\Lambda_+^l \varepsilon + \phi_+^l$, $2\pi l\mathcal{F}_- = 2\Lambda_-^l \varepsilon + \phi_-^l$, with $\phi_\pm^l$ properly defined by comparison with these equations, and assuming an energy-independent Dingle factor (only true for Lorentzian broadening.), we need to calculate integrals of the following form,

$$\int_0^\infty d\varepsilon \left(-\frac{\partial f^0}{\partial \varepsilon} \right)\cos\left(2\Lambda_+^l \varepsilon + \phi_+^l\right)\cos\left(2\Lambda_-^l \varepsilon + \phi_-^l\right) = \int_{-\frac{\mu}{2k_BT}}^\infty dx \frac{\cos\left(4\Lambda_+^l k_B Tx + 2\Lambda_+^l \mu + \phi_+^l\right)\cos\left(4\Lambda_-^l k_B Tx + 2\Lambda_-^l \mu + \phi_-^l\right)}{2\sinh^2 x}, \quad (G3)$$

where we have introduced the dimensioness quantity $x = \frac{\varepsilon - \mu}{2k_B T}$. For $\mu \gg k_B T$, we obtain

$$\int_0^\infty d\varepsilon \left(-\frac{\partial f^0}{\partial \varepsilon} \right)\cos\left(2\Lambda_+^l \varepsilon + \phi_+^l\right)\cos\left(2\Lambda_-^l \varepsilon + \phi_-^l\right) = \pi k_B T \left\{ \frac{\left(\Lambda_+^l - \Lambda_-^l\right)\cos\left[2\mu\left(\Lambda_+^l - \Lambda_-^l\right) + \phi_+^l - \phi_-^l\right]}{\sinh\left[2\pi k_B T\left(\Lambda_+^l - \Lambda_-^l\right)\right]} \right. \quad (G4)$$

$$\left. + \frac{\left(\Lambda_+^l + \Lambda_-^l\right)\cos\left[2\mu\left(\Lambda_+^l + \Lambda_-^l\right) + \phi_+^l + \phi_-^l\right]}{\sinh\left[2\pi k_B T\left(\Lambda_+^l + \Lambda_-^l\right)\right]} \right\}. \quad (G5)$$

using

$$\int_{-\infty}^\infty dx \frac{\cos(2\lambda_1 + a_1)\cos(2\lambda_2 + a_2)}{\cosh x^2}$$
$$= \frac{\pi(\lambda_1 - \lambda_2)\cos(a_1 - a_2)}{\sinh\pi(\lambda_1 - \lambda_2)} + \frac{\pi(\lambda_1 + \lambda_2)\cos(a_1 + a_2)}{\sinh\pi(\lambda_1 + \lambda_2)}$$

For the cases treated in this work, $\Lambda_+^l \gg \Lambda_-^l$ holds, and we obtain

$$\int_0^\infty d\varepsilon \left(-\frac{\partial f^0}{\partial \varepsilon} \right)\cos\left(2\Lambda_+^l \varepsilon + \phi_+^l\right)\cos\left(2\Lambda_-^l \varepsilon + \phi_-^l\right)$$
$$\approx \mathcal{A}_l(T)\cos\left(2\mu\Lambda_+^l + \phi_+^l\right)\cos\left(2\mu\Lambda_-^l + \phi_-^l\right),$$

with

$$\mathcal{A}_l(T) = \frac{2\pi k_B T \Lambda_+^l}{\sinh\left(2\pi k_B T \Lambda_+^l\right)}, \quad (G6)$$

for the temperature dependent coefficient for the SdH oscillation. For all the cases investigated in this work, we have $\Lambda_+ = \pi l/\hbar\omega_c$, yielding Eq. (25) in the main text,

$$\mathcal{A}_l(T) = \frac{2\pi^2 l k_B T/\hbar\omega_c}{\sinh\left(2\pi^2 l k_B T/\hbar\omega_c\right)}. \quad (G7)$$

[1] M. I. D'Yakonov and V. Perel, Soviet Journal of Experimental and Theoretical Physics Letters **13**, 467 (1971).

[2] M. I. Dyakonov and V. Perel, Physics Letters A **35**, 459

(1971).

[3] J. E. Hirsch, Phys. Rev. Lett. **83**, 1834 (1999).

[4] C. E. Landisman and B. W. Connors, Science **310**, 1809 (2005), https://www.science.org/doi/pdf/10.1126/science.1114655.

[5] J. Schliemann, J. C. Egues, and D. Loss, Phys. Rev. Lett. **90**, 146801 (2003).

[6] B. A. Bernevig, J. Orenstein, and S.-C. Zhang, Phys. Rev. Lett. **97**, 236601 (2006).

[7] J. Fu, P. H. Penteado, M. O. Hachiya, D. Loss, and J. C. Egues, Phys. Rev. Lett. **117**, 226401 (2016).

[8] C. L. Kane and E. J. Mele, Phys. Rev. Lett. **95**, 226801 (2005).

[9] B. A. Bernevig and S.-C. Zhang, Phys. Rev. Lett. **96**, 106802 (2006).

[10] B. A. Bernevig, T. L. Hughes, and S.-C. Zhang, Science **314**, 1757 (2006), https://www.science.org/doi/pdf/10.1126/science.1133734.

[11] A. Y. Kitaev, Physics-Uspekhi **44**, 131 (2001).

[12] L. Fu and C. L. Kane, Phys. Rev. B **79**, 161408 (2009).

[13] D. R. Candido, M. E. Flatté, and J. C. Egues, Phys. Rev. Lett. **121**, 256804 (2018).

[14] P. B. Pal, American Journal of Physics **79**, 485 (2011), https://doi.org/10.1119/1.3549729.

[15] A. Gilbertsson, M. Fearn, J. Jefferson, B. Murdin, P. Buckle, and L. Cohen, Phys. Rev. B **77**, 165335 (2008).

[16] L. Shubnikov and W. De Haas, J. de Haas, Leiden Commun. 207a, 207c **207**, 210a (1930).

[17] L. Shubnikov and W. de Haas, in *Proc. Netherlands Roy. Acad. Sci*, Vol. 33 (1930) p. 363.

[18] T. Smoleński, O. Cotlet, A. Popert, P. Back, Y. Shimazaki, P. Knüppel, N. Dietler, T. Taniguchi, K. Watanabe, M. Kroner, and A. Imamoglu, Phys. Rev. Lett. **123**, 097403 (2019).

[19] A. Kormányos, P. Rakyta, and G. Burkard, New Journal of Physics **17**, 103006 (2015).

[20] X. Cui, G.-H. Lee, Y. D. Kim, G. Arefe, P. Y. Huang, C.-H. Lee, D. A. Chenet, X. Zhang, L. Wang, F. Ye, *et al.*, Nature nanotechnology **10**, 534 (2015).

[21] S. Xu, Z. Wu, H. Lu, Y. Han, G. Long, X. Chen, T. Han, W. Ye, Y. Wu, J. Lin, *et al.*, 2D Materials **3**, 021007 (2016).

[22] X. Cui, E.-M. Shih, L. A. Jauregui, S. H. Chae, Y. D. Kim, B. Li, D. Seo, K. Pistunova, J. Yin, J.-H. Park, *et al.*, Nano letters **17**, 4781 (2017).

[23] D. Rhodes, S. H. Chae, R. Ribeiro-Palau, and J. Hone, Nature materials **18**, 541 (2019).

[24] M. Masseroni, T. Qu, T. Taniguchi, K. Watanabe, T. Ihn, and K. Ensslin, Phys. Rev. Res. **5**, 013113 (2023).

[25] S. Slizovskiy, P. Tomić, R. K. Kumar, A. Garcia-Ruiz, G. Zheng, E. Portolés, L. A. Ponomarenko, A. K. Geim, K. Watanabe, T. Taniguchi, *et al.*, arXiv preprint arXiv:2303.06403 (2023).

[26] G. J. Ferreira, D. R. Candido, F. G. G. Hernandez, G. M. Gusev, E. B. Olshanetsky, N. N. Mikhailov, and S. A. Dvoretsky, Scientific Reports **12** (2022), 10.1038/s41598-022-06431-0.

[27] Y. Cao, V. Fatemi, S. Fang, K. Watanabe, T. Taniguchi, E. Kaxiras, and P. Jarillo-Herrero, Nature **556**, 43 (2018).

[28] Y. Cao, V. Fatemi, A. Demir, S. Fang, S. L. Tomarken, J. Y. Luo, J. D. Sanchez-Yamagishi, K. Watanabe, T. Taniguchi, E. Kaxiras, *et al.*, Nature **556**, 80 (2018).

[29] J. Hu, Z. Tang, J. Liu, X. Liu, Y. Zhu, D. Graf, K. Myhro, S. Tran, C. N. Lau, J. Wei, *et al.*, Physical Review Letters **117**, 016602 (2016).

[30] H. Murakawa, M. S. Bahramy, M. Tokunaga, Y. Kohama, C. Bell, Y. Kaneko, N. Nagaosa, H. Y. Hwang, and Y. Tokura, Science **342**, 1490 (2013), https://www.science.org/doi/pdf/10.1126/science.1242247.

[31] B. Datta, P. C. Adak, L. kun Shi, K. Watanabe, T. Taniguchi, J. C. W. Song, and M. M. Deshmukh, Science Advances **5**, eaax6550 (2019), https://www.science.org/doi/pdf/10.1126/sciadv.aax6550.

[32] A. Alexandradinata, C. Wang, W. Duan, and L. Glazman, Physical Review X **8**, 011027 (2018).

[33] T. Ihn, *Semiconductor Nanostructures* (Oxford University Press, 2010).

[34] B. Das, D. Miller, S. Datta, R. Reifenberg, W. Hong, P. Bhattacharya, J. Singh, and M. Jaffe, Phys. Rev. B **39**, 1411 (1989).

[35] J. Nitta, T. Akazaki, H. Takayanagi, and T. Enoki, Phys. Rev. Lett. **78**, 1335 (1997).

[36] G. Engels, J. Lange, T. Schäpers, and H. Lüth, Phys. Rev. B **55**, R1958 (1997).

[37] T. Schäpers, G. Engels, J. Lange, T. Klocke, M. Hollfelder, and H. LÃŒth, Journal of Applied Physics **83**, 4324 (1998), https://pubs.aip.org/aip/jap/article-pdf/83/8/4324/10592945/4324_1_online.pdf.

[38] M. Akabori, T. Sunouchi, T. Kakegawa, T. Sato, T. Suzuki, and Y. Yamada, Physica E **34**, 413 (2006).

[39] M. Akabori, V. Guzenko, T. Sato, T. Schäpers, T. Suzuki, and S. Yamada, Phys. Rev. B **77**, 205320 (2008).

[40] W. Yang and K. Chang, Phys. Rev. B **73**, 045303 (2006).

[41] A. J. A. Beukman, F. K. de Vries, J. van Veen, R. Skolasinski, W. Wimmer, F. Qu, D. T. de Vries, B.-M. Nguyen, W. Yi, A. A. Kiselev, M. Sokolich, M. J. Manfra, F. Nichele, C. M. Marcus, and L. P. Kouwenhoven, Phys. Rev. B **96**, 241401 (2017).

[42] R. Winkler, S. Papadakis, E. De Poortere, and M. Shayegan, Physical review letters **84**, 713 (2000).

[43] M. Raikh and T. Shahbazyan, Phys. Rev. B **49**, 5531 (1994).

[44] N. Averkiev, M. Glazov, and S. Tarasenko, Solid State Commun. **133**, 543 (2005).

[45] E. Cimpoiasu, B. Dunphy, S. Mack, J. Christodoulides, B. Lunsford-Poe, and B. Bennett, Journal of App. Phys. **126**, 075704 (2019).

[46] F. Dettwiler, J. Fu, S. Mack, P. J. Weigele, J. C. Egues, D. D. Awschalom, and D. M. Zumbühl, Phys. Rev. X **7**, 031010 (2017).

[47] M. Brack and R. Bhaduri, *Semiclassical physics* (Addison-Wesley Publishing, 1997).

[48] Y. Bychkov and E. Rashba, J. Phys. C **17**, 6039 (1984).

[49] G. Dresselhaus, Phys. Rev. **100**, 580 (1955).

[50] R. Winkler, *Spin-Orbit Coupling Effects in Two-Dimensional Electron and Hole Systems* (Springer Verlag, 2003).

[51] D. Braak, Phys. Rev. Lett. **107**, 100401 (2011).

[52] J. Casanova, G. Romero, I. Lizuain, J. J. García-Ripoll, and E. Solano, Physical Review Letters **105**, 263603 (2010).

[53] J. Schliemann, J. C. Egues, and D. Loss, Phys. Rev. B **67**, 085302 (2003).

[54] M. Zarea and S. Ulloa, Phys. Rev. B **72**, 085342 (2005).

[55] X. Wang and P. Vasilopoulos, Phys. Rev. B **72**, 085344 (2005).

[56] D. Zhang, J. Phys. A: Math. Gen. **39**, L477 (2006).

[57] S. Erlingsson, J. Egues, and D. Loss, Phys. Rev. B **82**, 155456 (2010).

[58] S. Tarasenko, Physics of Solid State **44**, 1769 (2002).

[59] B. Laikhtman and B. Altshuler, Annals of Physics **232**, 332 (1994).

[60] Z. Lei, C. A. Lehner, K. Rubi, E. Cheah, M. Karalic, C. Mittag, L. Alt, J. Scharnetzky, P. Märki, U. Zeitler, W. Wegscheider, T. Ihn, and K. Ensslin, Phys. Rev. Research **2**, 033213 (2020).

[61] InAs has the value of $\tilde{\Delta} \approx 0.24$, but one would have a symmetric structure to minimize the spin-orbit contribution.

[62] S. Tarasenko and N. Averkiev, JETP Lett. **75**, 552 (2002).

[63] Here we emphasize that depending on the values of Λ and Ω, the argument of square root of Eq. (57) becomes nega-

tive, thus yielding imaginary energies. This happens when $x \gg 1$, which violates the assumption of writing Eq. (57).

[64] A. Gilbertsson, W. Branford, L. B. M.F̃earn, T. Ashley, and L. Cohen, Phys. Rev. B **79**, 235333 (2009).

[65] J. Fu, P. H. Penteado, D. R. Candido, G. J. Ferreira, D. P. Pires, E. Bernardes, and J. C. Egues, Phys. Rev. B **101**, 134416 (2020).

[66] J. R. Schrieffer and P. A. Wolff, Phys. Rev. **149**, 491 (1966).

[67] D. L. Sergey Bravyi, David DiVincenzo, Annals of Physics **326**, 2793 (2011).

Chapter 3

Numerical Approach

Efficient method to calculate energy spectra for analysing magneto-oscillations

Hamed Gramizadeh,[1] Denis R. Candido,[2] Andrei Manolescu,[3] J. Carlos Egues,[4, 5] and Sigurdur I. Erlingsson[3]

[1]*Department of Engineering, Reykjavik University, Menntavegi 1, IS-102 Reykjavik, Iceland*
[2]*Department of Physics and Astronomy, University of Iowa, Iowa City, Iowa 52242, USA*
[3]*Department of Engineering, School of Technology,*
Reykjavik University, Menntavegi 1, IS-102 Reykjavik, Iceland
[4]*Instituto de Física de São Carlos, Universidade de São Paulo, 13560-970 São Carlos, SP, Brazil*
[5]*Department of Physics, University of Basel, CH-4056, Basel, Switzerland*
(Dated: May 19, 2023)

Magneto-oscillations in two-dimensional systems with spin-orbit interaction are typically characterized by fast Shubnikov-de Haas (SdH) oscillations and slower spin-orbit-related beatings. The characterization of the full SdH oscillatory behavior in systems with both spin-orbit interaction and Zeeman coupling requires a time consuming diagonalization of large matrices for many magnetic field values. By using the Poisson summation formula we can explicitly separate the density of states into, fast and slow oscillations, which determine the corresponding fast and slow parts of the magneto-oscillations. We introduce an efficient scheme of partial diagonalization of our Hamiltonian, where only states close to the Fermi energy are needed to obtain the SdH oscillations, thus reducing the required computational time. This allows an efficient method for fitting numerically the SdH data, using the inherent separation of the fast and slow oscillations. We compare systems with *only* Rashba spin-orbit interaction (SOI) and *both* Rashba and Dresselhaus SOI with, and without, an in-plane magnetic field. The energy spectra are characterized in terms of symmetries, which have direct consequences visible in the magneto-oscillations. To highlight the benefits of our methodology, we use it to extract the spin-orbit parameters by fitting realistic transport data.

I. Introduction

Shubnikov-de Haas (SdH) oscillations [1, 2] have been an important tool to characterize charge densities, and scattering times in 2D semiconductor [3]. In addition, the SdH oscillations have been used to extract the Rashba and Dresselhaus spin-orbit interactions (SOI)[4]. Earlier theoretical description showed that the SOI leads to changes in the oscillation beating pattern [5], and further analysis of the same group incorporated the known exact result[6] to improve the analysis of the Rashba and Zeeman coupling [7]. As is pointed out in Ref. [8], the study and interpretation of oscillations in the magnetoresistance relies on some assumptions , as for example, what the dominant source of SOI is. A method that has often been used to estimate the strength of the Rashba coupling was introduced in Ref. [9–11], which uses the density of states (DOS) at *zero* magnetic field to relate the DOS to the Rashba SOI strenght α. However, this method has drawbacks since it can not account for Zeeman (via the g-factor g^*) or Dresselhaus spin-orbit coupling [12, 13]. There have been some attempts to analyze the SdH oscillations in terms of α, β, and g^* , but they have mostly involved qualitative comparison with the energy spectrum of pure Rashba and pure Dresselhaus [13, 14].

Magnetoresistance oscillations were considered by Tarasenko and co-authors [15, 16] for the special case of $\alpha = \beta$ and no Zeeman coupling. They showed that the beatings vanished for this case, since the corresponding spectrum consists of equally spaced Landau levels. Furthermore, the effects of Zeeman splitting and tilted magnetic field (in the absence of spin-orbit coupling)

were considered in Ref. [17]. In Ref. 18, full numerical calculations of magneto-oscillations were performed for relatively high magnetic fields and low electron densities, which is far away from the regime of recent experimental works.[19] In Ref. [19, 20] numerical calculations of magnetoresistivity-oscillations were performed, but a general analysis of the oscillations, relating the frequency and position of beating pattern directly to α and β, was not presented. Such connections are very important for experimental works as they allow the extraction of system parameters. In a recent experimental work, SdH oscillations were considered in InAs 2DEGs, where the Rashba SOI was tuned, but there were unresolved issues concerning the cubic Dresselhaus SOI [19]. Furthermore, the effects of the tilted magnetic field were theoretically considered in the context of the cyclotron and electric-dipole spin resonances in the presence of both Rashba and Dresselhaus SOI [20]. For tilting angles at which the Zeeman splitting and cyclotron energy were equal, the effects of the SOI could be made more pronounced. This has been used in more recent experiments studying magnetization [21] and magneto-oscillations [22], although the analysis suffers from the same issues discussed in Ref. [13].

In this paper we introduce a new efficient method to obtain the relevant energy spectrum for magneto transport, in the presence of both Rashba and Dresselhaus SOIs and Zeeman coupling. Our method is based on the diagonalization of a partial/truncated Hamiltonian, and allows a faster calculation, and clearer interpretation of SdH magneto-oscillations. In Sec. II we introduce the system properties and the partial Hamiltonian. In Sec. III we present the density of states using the Poisson

summation formula and highlight the fast and slow, oscillations. Finally, we apply our method to accurately fit realistic magneto-oscillation data, highlighting the speed and convenience of our method.

II. Hamiltonian and numerical diagonalization

Our focus will be on two dimensional electron gas (2DEG) in the presence of a magnetic field $\boldsymbol{B} = (B_\parallel \cos(\phi), B_\parallel \sin(\phi), B_\perp)$, where $B_\perp$ is the component of the magnetic field perpendicular to the 2DEG. In addition, we consider both Rashba[6] and Dresselhaus[12] spin-orbit couplings. The resulting Hamiltonian is

$$
\begin{aligned}
H_{2D} &= \frac{1}{2m^*}\left(\pi_x^2 + \pi_y^2\right) + \frac{g^*\mu_B}{2}B_\perp \sigma_z \\
&+ \frac{g^*\mu_B B_\parallel}{2}\left(\sigma_x \cos(\phi) + \sin(\phi)\sigma_y\right) \\
&+ \frac{\alpha}{\hbar}(\pi_y \sigma_x - \pi_x \sigma_y) + \frac{\beta}{\hbar}(\pi_x \sigma_x - \pi_y \sigma_y), \quad (1)
\end{aligned}
$$

where the $\hbar$ is reduced Planck's constant, m^* is the effective electron mass, g^* is the effective g-factor, and μ_B is the Bohr magneton, and and σ_x, σ_y, σ_z denote the usual Pauli matrices. The angle θ describes the tilting of the magnetic field away from the perpendicular direction, and we assume that $B \equiv B_\perp$ is fixed for all tilting angles, which is done to ease the comparison between different tilting angles, with absolute value of the applied magnetic field $B/\cos(\theta)$. The strength of the Rashba and Dresselhaus SOI are determined by the coefficients α and β, respectively. The momenta are given by $\pi_x = p_x - eBy/2$, and $\pi_y = p_y + eBx/2$, where $e > 0$ is the electrical charge. Note that the gauge is chosen such that $B_\parallel$ drops out from the momenta once the 3D problem is projected onto the lowest transverse level. Next, we introduce the ladder operators

$$
a = \frac{\ell_c}{\sqrt{2}\hbar}\left(\pi_x - i\pi_y\right), \quad \text{and} \quad a^\dagger = \frac{\ell_c}{\sqrt{2}\hbar}\left(\pi_x + i\pi_y\right),
\tag{2}
$$

where $\ell_c = \sqrt{\frac{\hbar}{eB}}$ is the magnetic length. The ladder operators obey the commutation relation $[a, a^\dagger] = 1$, as a consequence of the canonical commutation relations $[x, p_x] = i\hbar$ and $[y, p_y] = i\hbar$. The Hamiltonian then reduces to

$$
\begin{aligned}
\frac{H_{2D}}{\hbar\omega_c} &= a^\dagger a + \frac{1}{2} + \frac{\tilde{\Delta}}{2}\left(\sigma_z + \frac{\tan(\theta)}{2}\left(\sigma_+ e^{i\phi} + \sigma_- e^{-i\phi}\right)\right) \\
&+ \frac{\beta}{\sqrt{2}\hbar\omega_c \ell_c}(a^\dagger \sigma_+ + a\sigma_-) - \frac{i\alpha}{\sqrt{2}\hbar\omega_c \ell_c}(a^\dagger \sigma_- - a\sigma_+),
\end{aligned}
\tag{3}
$$

where the Zeeman term $\tilde{\Delta} = \frac{g^*\mu_B B}{\hbar\omega_c} = \frac{g^*m^*}{2}$ inherited its sign from the g^*-factor, and $\omega_c = eB/m^*$ is the cyclotron frequency, $\sigma_\pm = \sigma_x \pm i\sigma_y$. The standard way of obtaining the spectrum of the Hamiltonian Eq. (3) is
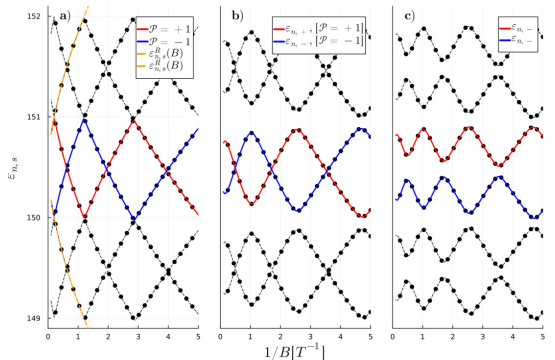

FIG. 1. Comparison of full diagonalization [black points] and partial Hamiltonian [red and blue curves], for a) $\alpha = 7.5\,\mathrm{meV\,nm}$, $\beta = 0$, b) $\alpha = 7.5\,\mathrm{meV\,nm}$, $\beta = 3.0\,\mathrm{meV\,nm}$, and c) $\alpha = 7.5\,\mathrm{meV\,nm}$, $\beta = 3.0\,\mathrm{meV\,nm}$, and $\theta = \pi/3$. Other parameters are $m^* = 0.04$, $g^* = -12$ and $n_{2D} = 0.0176\,\mathrm{nm}^{-2}$ for InAs based systems.[19]

by creating a matrix of dimension $2N \times 2N$, where N is the number of eigenstates of $a^\dagger a$ (i.e. $a^\dagger a|m\rangle = m|m\rangle$, $m = 0, 1, \ldots, N-1$), in addition to accounting for the spin-degree (i.e $\sigma_z|\sigma\rangle = \sigma|\sigma\rangle$, $\sigma = \pm 1$). The choice of N depends on the number of eigenstates that are required for a given problem. In the case of magnetotransport calculations for realistic systems parameters, the required eigenstates are counted in the hundreds, and to calculate those states accurately, the size of N should be around four times larger [23], resulting in $N \sim 10^3$. Although diagonalizing a single such matrix does not represent a computational challenge, the diagonalization has to be repeated for multiple values of magnetic field (measured in the thousands), and α, β, etc. Accounting for all this, calculating a set of magnetoresistance curves can lead to computational time around multiple hours [24].

The method we introduce here is designed to efficiently calculate the eigenenergies for a given n, which labels the Landau levels. Before outlining the methods, we first discuss general properties of the Hamiltonian Eq. (3). If we have $\beta = \theta = 0$, we can obtain exact eigenvalues (see App. A)

$$
\varepsilon_{n,+} = n + 1 - \sqrt{\frac{(1-\tilde{\Delta})^2}{4} + 4\frac{\varepsilon_R}{\hbar\omega_c}(n+1)}, \quad (4)
$$

$$
\varepsilon_{n,-} = n + \sqrt{\frac{(1-\tilde{\Delta})^2}{4} + 4\frac{\varepsilon_R}{\hbar\omega_c}n}, \quad (5)
$$

where $\varepsilon_R = \frac{m^*\alpha^2}{2\hbar^2}$. These eigenvalue are plotted in Fig. 1a) for $n = 150$ (dashed orange curve). When the same system is diagonalized numerically, the energy spectra take a sawtooth shape since the numerical diagonalization orders the eigenvalues according to their size and crossings turn into anticrossings (black dotted lines).

There is an underlying parity symmetry for $\theta = 0$, first introduced in Refs. [25, 26] for $\alpha = \beta$, and later extended for systems with Rashba and Dresselhaus coupling in Ref. [27]. This parity allows the spectrum to be split into two separate subspaces that can be diagonalized separately, see App. B 1. When this is done, we obtain states with different parities crossing each other, as they belong to different parity subspaces (blue and red curves). However, they anticross with other states that belong to the *same* parity space.

In Fig. 1b) a non-zero value of $\beta = 3.0\,\text{meV nm}$ is added, which opens up overall gaps in the spectrum, but leaves some crossing unaffected. The spectrum now consists of pairs of states for each value of n and $s = \pm 1$ which cross, but anticross with adjacent states above and below. Finally, in Fig. 1c) an in-plane component of the
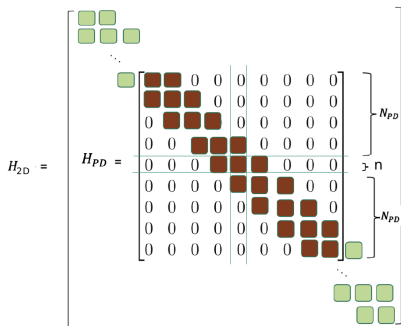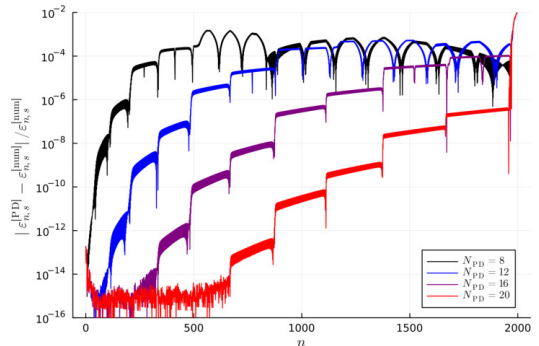

FIG. 3. Relative deviation between eigenstates obtained using full numerical diagonalization with $N = 1000$, $\varepsilon_{n,s}^{[\text{num}]}$ and the eigenstates with the partial diagonalization, $\varepsilon_{n,s}^{[\text{PD}]}$, as a function of N_{PD} for magnetic field $B = 0.15\,\text{T}$. Parameter values are $\alpha = 7.5\,\text{meV nm}$, $\beta = 3.0\,\text{meV nm}$, and $\theta = 0$. Other parameters are $m^* = 0.04$, $g^* = -12$ and $n_{2\text{D}} = 0.0176\,\text{nm}^{-2}$ for InAs based. systems[19]

FIG. 2. The structure of H_{PD} illustrated relative to the full matrix $H_{2\text{D}}$. For a given value of n the partial matrix H_{PD} is constructed around matrix element $[H_{2\text{D}}]_{n,n}$.

magnetic field is added with $\theta = \pi/3$. For this case, the parity is no longer a good quantum number, i.e. the parity operator does not commute with H_{2D}, and extra anticrossings opens up between the $|n, +\rangle$ and $|n, -\rangle$ states corresponding to eigenenergies $\varepsilon_{n,+}$ and $\varepsilon_{n,+}$, respectively.

A. Numerical methods

Now, we turn to describing the numerical diagonalization procedure. As can be seen in Fig. 1b) and c) the eigenstates are always pushed up or down by their couplings to adjacent states. This results in each state following a unique curve which can be tracked, as a function of $1/B$, for all n. Based on this we introduce a partial diagonalization outlined in Fig. 2, where $n = 0, 1, 2 \ldots$ is the Landau level index of interest. The matrix representation of Eq. (3) can be written as a block-tridiagonal

matrix with diagonal 2×2 blocks

$$[H_{2\text{D}}]_{m,m} = \begin{bmatrix} m + \frac{1}{2} + \frac{\tilde{\Delta}}{2} & \frac{\tilde{\Delta}}{2}\tan(\theta)e^{i\phi} \\ \frac{\tilde{\Delta}}{2}\tan(\theta)e^{-i\phi} & m + \frac{1}{2} - \frac{\tilde{\Delta}}{2} \end{bmatrix}, \quad (6)$$

where σ_0 is the Pauli identity matrix, and off-diagonal 2×2 block is given by

$$[H_{2\text{D}}]_{m,m+1} = \sqrt{m+1}\frac{1}{\sqrt{2}\hbar\omega_c\ell_c}\begin{bmatrix} 0 & 2\beta \\ -2i\alpha & 0 \end{bmatrix}. \quad (7)$$

With these we construct the partial matrix H_{PD} centered on block n with N_{PD} blocks above and below. The resulting matrix has dimension $2(2N_{\text{PD}}+1) \times 2(2N_{\text{PD}}+1)$, see App. B 2.

If the parity is a good quantum number, i.e. $\theta = 0$, then each block in H_{PD} is halved (i.e. becomes 1×1) when each parity subspace is considered, see App. B 1 for details. For states with $n \leq N_{\text{PD}}$, then the lower part of the partial matrix is decreased accordingly, and for $n = 0$ only N_{NP} states above n are needed. With this, the entire spectrum can be calculated for each value of n. To test the accuracy of this procedure we calculate the relative deviation between the full numerical diagonalization, $\varepsilon_{n,s}^{[\text{num}]}$ for $N = 1000$ and the eigenstates obtained with the partial diagonalization, $\varepsilon_{n,s}^{[\text{PD}]}$, at $B = 0.15\,\text{T}$ for $\alpha = 7.5\,\text{meV nm}$, $\beta = 3.0\,\text{meV nm}$, and $\theta = 0$. Figure 3 shows our results for $N_{\text{PD}} = 8$, 12, 16 and 20. Already for $N_{\text{PD}} = 16$ the relevant eigenenergies (first quarter of eigenvalues) have a relative deviation less than 10^{-10}, and for $N_{\text{PD}} = 20$ the machine precision is reached for all relevant eigenvalues.

As we will see in the next section, allowing n to take *non-integer* values can be useful in calculating the density of states and transport properties. As is discussed in

App. B 1 this can be implemented via the partial diagonalization, i.e. one can calculate eigenenergies $\varepsilon_{n+\Delta x,s}$, where $\Delta x \in [-0.5, 0.5]$ is a real number. The interval is set by the condition that $\varepsilon_{n+\Delta x,s} = \varepsilon_{n+1-\Delta x,s}$, i.e. $\Delta x = 0.5$ corresponds to a crossing with next state above, and similarly $\Delta x = -0.5$ corresponds to a crossing with the next state below.

III. Density of States and F-function

The eigenenergies of the Hamiltonian Eq. (1) results in a discrete spectrum, the well known Landau levels [3]. The resulting DOS is given by

$$D(E_F, B) = \frac{1}{2\pi\ell_c^2} \sum_{n=0}^{\infty} \sum_s L_\Gamma(E_F - \hbar\omega_c\varepsilon_{ns}(B)), \quad (8)$$

where $1/2\pi\ell_c^2$ accounts for the Landau level degeneracy (per spin), and $L_\Gamma(x)$ describes broadening due impurity scattering [3]. Here it is assumed that all levels are broadened by a phenomenological parameter Γ, e.g., $\delta(\cdot) \to L_\Gamma(\cdot)$, for Gaussian broadening with $L_\Gamma(x) = e^{-\frac{x^2}{2\Gamma^2}}/\sqrt{2\pi\Gamma^2}$. Our goal is to rewrite the DOS in a way that highlights the fast and slow oscillations, which are not directly evident in Eq. (8). This is achieved using by the Poisson summation formula [3, 4, 17, 28] which results in

$$\delta D(B) \equiv \frac{D(E_F, B) - D_0}{D_0} \quad (9)$$

$$\simeq 2\sum_{l=1}^{\infty} \tilde{L}\left(l\frac{\Gamma}{\hbar\omega_c}\right) \cos(l2\pi\mathcal{F}_+)\cos(l2\pi\mathcal{F}_-), \quad (10)$$

where $D_0 = \frac{\hbar^2}{\pi m^*}$ is the zero-field DOS, $\tilde{L}_\Gamma$ is the cosine transform of the broadening function, and the functions $\mathcal{F}_\pm \equiv \frac{1}{2}(F_+ \pm F_-)$ represent the fast $(+)$ and slow $(-)$ parts of the SdH oscillations, respectively. Details of this derivation are found in App. C. The functions $F_s = F_s(E_F, B)$, with $s = \pm 1$, are defined by the relation

$$\varepsilon_{n,s}(B) = \frac{E_F}{\hbar\omega_c} \Leftrightarrow n = F_s(E_F, B), \quad (11)$$

so determining F_s becomes a root finding problem. In Fig. 4a) we plot a zoom-in of $\varepsilon_{n,s}(B)$ along with $E_F/\hbar\omega_c$ [gray solid line]. Accepting *non-integer* values of n allows the energy levels to cross $E_F/\hbar\omega_c$ for fixed values of $1/B$ and E_F. The dominant behavior of $\varepsilon_{n,s}(B)$ with respect to n is linear (see App. A) as is visible in Fig. 4b). The energy levels cross $E_F/\hbar\omega_c$ at values n_+ and n_-, for $\varepsilon_{n,+}(B)$ and $\varepsilon_{n,-}(B)$, respectively, which are the values of the corresponding F_s-functions : $n_s = F_s(E_F, B)$.

As seen in Fig. 1b), gaps open in the spectrum when both α and β are non-zero. In Fig. 5a) a zoom-in of $\varepsilon_{n,s}(B)$ is shown along with $E_F/\hbar\omega_c$ [gray solid line] for $\alpha = 7.5\,\text{meV nm}$ and $\beta = 3.0\,\text{meV nm}$. The dashed curves are the corresponding pure Rashba eigenenergies.
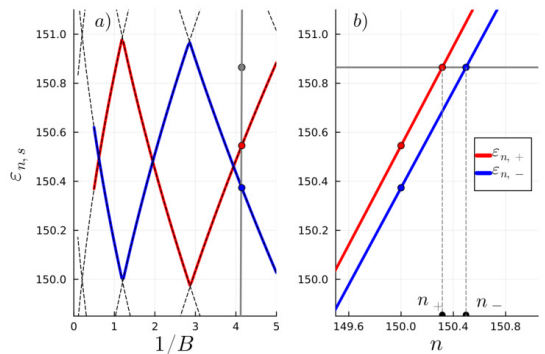

FIG. 4. a) Energy level $n = 150$ using the PD algorithm, along with adjacent states [dashed black line] for $\alpha = 7.5\,\text{meV nm}$ and $\beta = 0.0$. The solid gray line shows $E_F/\hbar\omega_c$, and its value at $1/B = 4.145$ [gray circle]. b) The energy levels $\varepsilon_{n,s}(B)$ as a function of n showing the intersection with $E_F/\hbar\omega_c$ at $1/B = 4.145$. Other parameters are $m^* = 0.04$, $g^* = -12$ and $n_{2D} = 0.0176\,\text{nm}^{-2}$ for InAs based systems.[19]
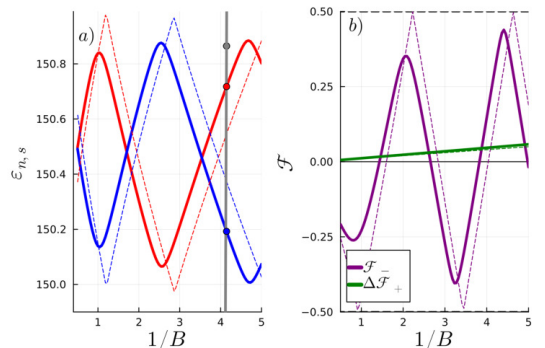
FIG. 5. a) Energy level $n = 150$ using the PD algorithm for $\alpha = 7.5\,\text{meV nm}$ and $\beta = 3.0\,\text{meV nm}$. The dashed curves correspond to $\alpha = 7.5\,\text{meV nm}$ and $\beta = 0$. The solid gray line shows $E_F/\hbar\omega_c$, and its value at $1/B = 4.145$ [gray circle]. b) The $\mathcal{F}$-function for $\alpha = 7.5\,\text{meV nm}$ and $\beta = 3.0\,\text{meV nm}$ [solid lines], and pure Rashba, $\beta = 0$ [dashed line]. Other parameters are $m^* = 0.04$, $g^* = -12$ and $n_{2D} = 0.0176\,\text{nm}^{-2}$ for InAs based systems.[19]

Note the sawtooth shape of the dashed curves since all states cross in this case. The corresponding $\mathcal{F}$-functions are shown in Fig. 5b). The anticrossings in the spectrum are visible as a rounding of the sawtooth shape, and level crossings correspond to $\mathcal{F}_- = 0$.

It is instructive to look at the $\mathcal{F}_\pm$-function in the case of pure Rashba SOI,

$$\mathcal{F}_+ = \frac{E_F}{\hbar\omega_c} + \frac{2\varepsilon_R}{\hbar\omega_c} - \frac{1}{2} = \frac{h}{2e}n_{2D}\frac{1}{B} - \frac{1}{2} + \frac{2\varepsilon_R}{\hbar\omega_c}, \quad (12)$$

$$\mathcal{F}_- = -\frac{1}{2} + \sqrt{\frac{(1-\tilde{\Delta})^2}{4} + \frac{\varepsilon_R E_F}{(\hbar\omega_c)^2}} \approx \frac{m^*\alpha k_F}{e\hbar}\frac{1}{B} \quad (13)$$

where $k_F = \sqrt{2\pi n_{2\mathrm{D}}}$, and the approximate sign in Eq. (13) refers to the *low* field limit. Since the SdH oscillation frequency in Eq. (12) is dominated by the term proportional to $n_{2\mathrm{D}}$, we define the spin-orbit related contribution to the fast oscillations as

$$\Delta\mathcal{F}_+ \equiv \mathcal{F}_+ - \left(\frac{h}{2e}n_{2D}\frac{1}{B} - \frac{1}{2}\right). \quad (14)$$

This allows us to plot on the same graph the slow spin-orbit related oscillations described by $\mathcal{F}_-$ and the spin-orbit related modification of the fast oscillation $\Delta\mathcal{F}_+$. Note that the sawtooth shape in Fig. 5b) for the case of pure Rashba SOI [purple dashed curve] have a fixed slope $\pm\frac{m^*\alpha k_F}{e\hbar}$. This is equivalent to the result in Eq. (13), which is linear in $1/B$, since $\cos(2l\pi\mathcal{F}_-) = \cos(-2l\pi\mathcal{F}_-)$, i.e. the sign of the $\mathcal{F}_-$-slope is irrelevant.

FIG. 6. a) Energy level $n = 150$ using the PD algorithm for $\alpha = 7.5\,\mathrm{meV\,nm}$, $\beta = 3.0\,\mathrm{meV\,nm}$, and $\theta = \pi/3$. The dashed curves correspond to $\alpha = 7.5\,\mathrm{meV\,nm}$ and $\beta = 0$. The solid gray line shows $E_F/\hbar\omega_c$, and its value at $1/B = 4.145$ [gray circle]. b) The $\mathcal{F}$-function for $\alpha = 7.5\,\mathrm{meV\,nm}$ and $\beta = 3.0\,\mathrm{meV\,nm}$ [solid lines], and pure Rashba, $\beta = 0$ [dashed line]. Other parameters are $m^* = 0.04$, $g^* = -12$ and $n_{2\mathrm{D}} = 0.0176\,\mathrm{nm}^{-2}$ for InAs based systems.[19]
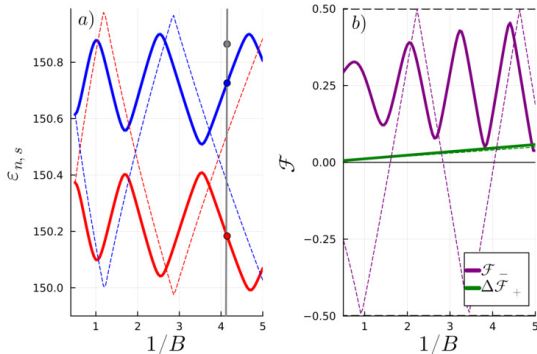
Finally, we consider the influence of an in-plane component of the magnetic field, i.e. $\theta \neq 0$. In this case the parity symmetry no longer holds and *all* states anticross as seen in Fig. 6a). This results in no states simultaneously crossing E_F, due to the level repulsion. Note that $\mathcal{F}_- = 0$ corresponds to both pseudo-spin species simultaneously crossing E_F at a given B-field. These new anticrossings have a direct effect on the $\mathcal{F}_-$-function here, which never reaches zero, as opposed to Fig. 5b) where $\mathcal{F}_-$ takes both positive and negative values. The $\mathcal{F}_-$ thus contains information on how close to (or far from) each other states with opposite s cross E_F. This property is useful when interpreting so-called *coincidence*
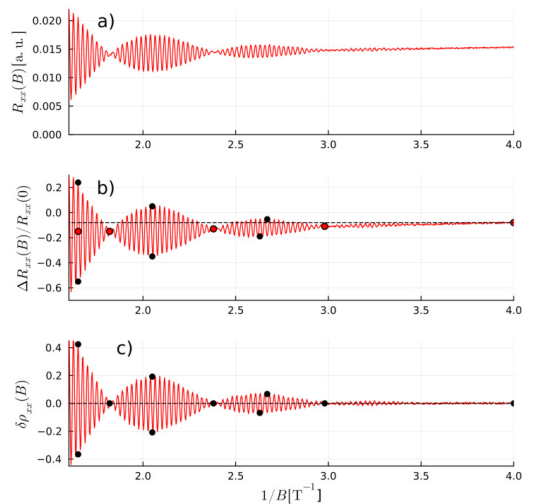

FIG. 7. a) Magnetoresistance data generated using Eq. (8) with $\Gamma = 0.45\,\mathrm{meV}$, $n_{2\mathrm{D}} = 0.019\,\mathrm{nm}^{-2}$, $\alpha = 7.20\,\mathrm{meV\,nm}$ and $\beta = 2.40\,\mathrm{meV\,nm}$. Slight background slope and random noise is to mimic realistic measurements. b) Normalized magneto-oscillations showing slope due to background. Extrema and zeros are indicated by black and red dots, respectively. c) Proper normalized magneto-oscillations after subtracting background [see Sec. IV for details]. Other parameters are $m^* = 0.04$, $g^* = -12$. [19]

measurements [29] that have been used to map out level crossings in SdH oscillations in 2DEGs in tilted magnetic fields.[30, 31]

IV. Fitting magnetotransport data

The oscillation frequencies introduced in the previous section allows for a convenient separation of tasks when analyzing the magneto-oscillations. In 2D systems, the longitudinal resistance is proportional to the DOS [3], so the previous analysis applies directly to their magneto-oscillations. The rapid oscillations, i.e. SdH oscillation frequency $f^{\mathrm{SdH}} = \frac{h}{2e}n_{2\mathrm{D}}$ can be easily extracted by calculating the frequency spectrum via FFT, thus yielding the 2DEG density $n_{2\mathrm{D}}$ [10, 19]. The remaining parameters (α, β and Γ) can be found by fitting the *slow* spin-orbit related oscillations. We outline below this procedure for fitting realistic magnetoresistance data.

Our starting point is Eq. (8), which we use to generate realistic magnetoresistance data [19]. We use parameters $\Gamma = 0.45\,\mathrm{meV}$, $n_{2\mathrm{D}} = 0.019\,\mathrm{nm}^{-2}$, $\alpha = 7.20\,\mathrm{meV\,nm}$ and $\beta = 2.40\,\mathrm{meV\,nm}$, and add a slight background and noise components to better mimic realistic data. The resulting $R_{xx}(B)$ is shown in Fig. 7a) where a slight upward slope is barely discernible. From the R_{xx} data, the normalized

magneto-oscillation is calculated

$$\Delta R_{xx} = \frac{R_{xx}(B) - R_{xx;0}}{R_{xx;0}}, \qquad (15)$$

where $R_{xx;0}$ is defined as the resistance at the magnetic field where the oscillations have been fully suppressed, in this case for $B \leq 0.25\,\text{T}$. This is plotted in Fig. 7b), where the extremas have been marked with black dots, and central points (zeros) are marked with red dots. The background signal showing a slight upward trend is now more visible. The data is brought to the proper normalized magneto-oscillation form, shown in Fig. 7c), by subtracting the background using a simple linear interpolation between the middle points [red points in Fig. 7b). At this point, the data can be directly fitted to the *slow* oscillating terms in Eq. (10) using only a small number of points [black dots]. Due to background compensation we introduce an extra parameter R_0, so the resulting *slow* envelope function used for fitting is

$$\delta\rho_{xx}(B) = 2R_0 \tilde{L}_\Gamma \left(\frac{\Gamma}{\hbar\omega_c} \right) \cos(2\pi \mathcal{F}_-(B; \alpha, \beta)). \quad (16)$$
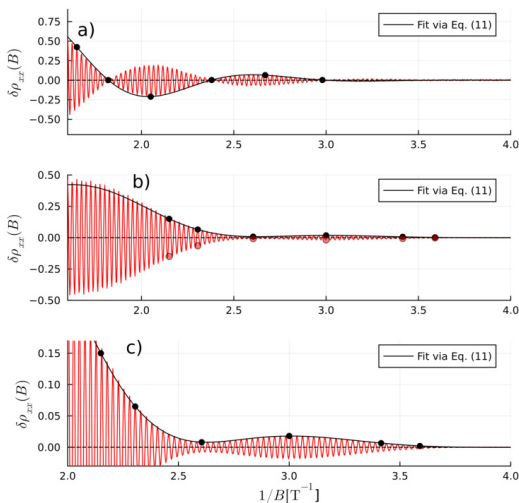
Fitting the data in Fig. 7c) to Eq. (16) results in

FIG. 8. a) The normalized magneto-oscillations along with fitted curve through 6 data points [black dots]. Resulting fitted parameters are $\alpha = (7.24 \pm 0.06)\,\text{meV nm}$ and $\beta = (2.5 \pm 0.3)\,\text{meV nm}$. b) Normalized magneto-oscillations generated using Eq. (8) with $\Gamma = 0.45\,\text{meV}$, $\alpha = 3.30\,\text{meV nm}$ and $\beta = 5.60\,\text{meV nm}$ [see main text]. c) Zoom in on reference points and fitted curve which yields fit values $\alpha = (3.33 \pm 0.03)\,\text{meV nm}$ and $\beta = (5.63 \pm 0.02)\,\text{meV nm}$.

a *slow* envelope shown in Fig. 8a). The results of the fitting yields parameter values $R_0 = 1.2 \pm 0.2$, $B_q = 0.71 \pm 0.03\,\text{T}$, $\alpha = (7.24 \pm 0.06)\,\text{meV nm}$ and

$\beta = (2.5 \pm 0.3)\,\text{meV nm}$. The fitting only takes a few tens of seconds, and a few attempts for finding a good starting point for the fitting parameters. Note that the time to generate the full data took a couple of hours (on the same computer). Attempting to fit real transport data using Eq. (8), which requires calculating the whole spectrum $\varepsilon_{n,s}(B)$ for all B-values to capture both fast *and* slow oscillations, would thus be prohibitively time consuming. Our method circumvents this problem by extracting the important slow spin-orbit-related oscillations via $\mathcal{F}_-(B)$, which are easily fitted using only 5-10 magnetic field points.

Finally, we point out that for cases where Rashba and Dresselhaus SOI parameters are close to each other in value, the slow part of the magnetoscillations does not cross zero, i.e. there are no beating nodes [27]. This can be seen in magneto-oscillation data in Fig. 8b) generated using $\alpha = 3.30\,\text{meV nm}$ and $\beta = 5.60\,\text{meV nm}$. The background can be subtracted using center points between the red and black dots. In Fig. 8c) a zoom-in of the reference points and fitted curve is shown. The fit values are $\alpha = (3.33 \pm 0.03)\,\text{meV nm}$ and $\beta = (5.63 \pm 0.02)\,\text{meV nm}$, which is a very good agreement with the parameter values used to generate the original data. Note that in both cases of Figs. 8a) and 8b), the reference points fulfill $\delta\rho_{xx} < 0.4$, which ensures that the higher harmonics can be neglected, due to the exponential suppression [27].

V. Conclusion

In this paper we presented a new method to efficiently calculate the relevant energy spectrum for SdH magneto-oscillation analysis. We showed that the numerical procedure along with the Poisson summation formula allow for an efficient calculation and a better understanding of the fast and slow magneto-oscillations. The spin-orbit parameters α and β, and the Landau level broadening Γ, can be uniquely extracted from $\mathcal{F}_-$, which oscillates slowly. To illustrate our method we applied it to realistic magneto-transport data and find that fitting the slow oscillations yields very quick and accurate fit results. The slow oscillations in $\mathcal{F}_-$ can also shed light on so-called coincidence measurements on tilted magnetic fields. Our method does not rely on finding beating nodes so it can be used fit data in case of α and β being comparable in size.

VI. Acknowledgment

A. $\varepsilon_{n,s}$ and F_s in the case of pure Rashba

The Hamiltonian in Eq. (3) with $\beta = \theta = 0$ results in the pure Rashba Hamiltonian

$$H_R = \left(a^\dagger a + \frac{1}{2}\right) + \frac{\tilde{\Delta}}{2}\sigma_z + \frac{\alpha}{\sqrt{2}\hbar\omega_c\ell_c}(a^\dagger\sigma_- + a\sigma_-). \quad \text{(A1)}$$

This can be written in 2×2 subspaces $\{|n,\uparrow\rangle, |n+1,\downarrow\rangle\}$, $n = 0, 1, \ldots,$[27] which results in the matrix

$$H_{R;2\times2} = \begin{bmatrix} n + \frac{(1+\tilde{\Delta})}{2} & \frac{2\alpha}{\sqrt{2}\hbar\omega_c\ell_c}(n+1) \\ \frac{2\alpha}{\sqrt{2}\hbar\omega_c\ell_c}(n+1) & n+1+\frac{(1-\tilde{\Delta})}{2} \end{bmatrix}$$

$$= (n+1) + \begin{bmatrix} \frac{(1-\tilde{\Delta})}{2} & \frac{\sqrt{2}\alpha}{\hbar\omega_c\ell_c}(n+1) \\ \frac{\sqrt{2}\alpha}{\hbar\omega_c\ell_c}(n+1) & -\frac{(1-\tilde{\Delta})}{2} \end{bmatrix} \quad \text{(A2)}$$

with eigenvalues

$$\varepsilon_{n,+} = (n+1) - \sqrt{\frac{(1-\tilde{\Delta})^2}{4} + \frac{2m^*\alpha^2}{\hbar\omega_c\hbar^2}(n+1)} \quad \text{(A3)}$$

$$\varepsilon_{n+1,-} = (n+1) + \sqrt{\frac{(1-\tilde{\Delta})^2}{4} + \frac{2m^*\alpha^2}{\hbar\omega_c\hbar^2}(n+1)} \quad \text{(A4)}$$

The above equations reduce to Eqs. (4) and (5) using $\varepsilon_R = \frac{m^*\alpha}{2\hbar^2}$. The labelling of the eigenstates is chosen such that in the limit $\alpha \to 0$ the eigenstates evolve into the correct eigenstates in the *absence* of SOI: $\varepsilon_{n,+} \to \varepsilon_{n,\uparrow}^0$ and $\varepsilon_{n+1,-} \to \varepsilon_{n+1,\downarrow}^0$.

The definition of the DOS in Eq. (8) contains a sum over $n = 0, 1, 2, \ldots$ which can be formally written as an integral over the *continuous* variable x via the Poisson summation formula (also known as trace formula [28]) in Eq. (C1). Since the eigenenergies $\varepsilon_{n,s}$ are a well defined function of n, the index n can be replaced by a continuous variable $x \in [0, \infty)$. The derivative of the eigenenergies with respect to x can then be calculated

$$\frac{\partial\varepsilon_{x,+}}{\partial x} = 1 - \frac{\frac{2\varepsilon_R}{\hbar\omega_c}}{\sqrt{\frac{(1-\tilde{\Delta})^2}{4} + \frac{4\varepsilon_R}{\hbar\omega_c}(x+1)}}, \quad \text{(A5)}$$

$$\approx 1 - \sqrt{\frac{\varepsilon_R}{E_F}} \approx 1, \quad \text{(A6)}$$

where we used $x + 1 \approx \frac{E_F}{\hbar\omega_c}$. The same argument applies to $\varepsilon_{x,-}$, i.e. $\frac{\partial\varepsilon_{x,-}}{\partial x} \approx 1$. In the case of non-zero β and/or θ in Eq. (3) will lead to anticrossings, which tend to *flatten* the square root behavior of the energy levels, see Fig. 1b) and c), thus making the approximation in Eq. (A6) even better.

B. Partial Hamiltonians and parity

Here we describe the form of the partial Hamiltonian in the case of parity symmetry [27], and in the absence of that symmetry.

1. Matrix elements and parity symmetry

As was outlined in Ref. 27 the full basis $|m, \sigma\rangle$ can be split in two according to the eigenvalues of the parity operator

$$\hat{\mathcal{P}} = \exp(i\pi(a^\dagger a + \frac{1}{2}(\sigma_z - 1))), \quad \text{(B1)}$$

which are $\mathcal{P} = \pm 1$. The basis states of the resulting parity subspace are then

$$\mathcal{P} = +1 : \quad \{|0,\uparrow\rangle, |1,\downarrow\rangle, |2,\uparrow\rangle, |3,\downarrow\rangle, |4,\uparrow\rangle, \ldots\} \text{(B2)}$$
$$\mathcal{P} = -1 : \quad \{|0,\downarrow\rangle, |1,\uparrow\rangle, |2,\downarrow\rangle, |3,\uparrow\rangle, |4,\downarrow\rangle, \ldots\} \text{(B3)}$$

The Hamiltonian matrix for each $\mathcal{P} = \pm 1$ subspace become a tridiagonal matrix with diagonal elements

$$\left[H_{2D}^{(+1)}\right]_{k,k} = k + \frac{1}{2} + \frac{\tilde{\Delta}}{2}(-1)^k \quad \text{(B4)}$$

$$\left[H_{2D}^{(-1)}\right]_{k,k} = k + \frac{1}{2} - \frac{\tilde{\Delta}}{2}(-1)^k, \quad \text{(B5)}$$

where $k = 0, 1, 2, \ldots$ labels the basis states in subspace $\mathcal{P} = \pm 1$. The alternating sign of the Zeeman term reflects the alternating $\uparrow$ and $\downarrow$ in the basis states in Eq. (B2) and (B3). The off-diagonal matrix elements are given by

$$\left[H_{2D}^{(+1)}\right]_{k,k+1} = \sqrt{k+1}\left(\frac{i\alpha}{\sqrt{2}\hbar\omega_c\ell_c}(1+(-1)^k)\right.$$
$$\left. + \frac{\beta}{\sqrt{2}\hbar\omega_c\ell_c}(1-(-1)^k)\right), \quad \text{(B6)}$$

$$\left[H_{2D}^{(-1)}\right]_{k,k+1} = \sqrt{k+1}\left(\frac{i\alpha}{\sqrt{2}\hbar\omega_c\ell_c}(1-(-1)^k)\right.$$
$$\left. + \frac{\beta}{\sqrt{2}\hbar\omega_c\ell_c}(1+(-1)^k)\right). \quad \text{(B7)}$$

The $(1 \pm (-1)^k)$ takes alternating values 0 and 2, which switches between the α and β couplings due to the alternating spin arrangement in Eqs. (B2) and (B3). Compare this to Eq. (7) in the *absence* of parity symmetry where each 2×2 block contains both α and β.

The partial Hamiltonian for $\mathcal{P} = +1$ centered on the n-th state is constructed from Eqs. (B4) and (B6)

$$\left[H_{PD}^{(+1)}(n)\right]_{m,m} = \left(n + (m - N_{PD} - 1) + \frac{1}{2}\right)$$
$$+ \frac{\tilde{\Delta}}{2}(-1)^{(\bar{n}+m-N_{PD}-1)}, \quad \text{(B8)}$$

$$\left[H_{PD}^{(+1)}(n)\right]_{m,m+1} = \sqrt{(n+m-N_{PD}-1)+1} \times$$
$$\left(\frac{i\alpha}{\sqrt{2}\hbar\omega_c\ell_c}(1+(-1)^{(\bar{n}+m-N_{PD}-1)})\right.$$
$$\left. + \frac{\beta}{\sqrt{2}\hbar\omega_c\ell_c}(1-(-1)^{(\bar{n}+m-N_{PD}-1)})\right) \quad \text{(B9)}$$

where $\bar{n} = \text{round}(n)$ and $m \in [1, 2N_{PD} + 1]$. The eigenenergy $\varepsilon_{n,s}^{(+1)}$ is obtained as the $(N_{PD}+1)$-th eigenvalue of

$H_{\rm PD}^{(+1)}(n)$. In a similar fashion the partial Hamiltonian for $\mathcal{P} = -1$ centered on the n-th state has matrix elements

$$\left[H_{\rm PD}^{(-1)}(n)\right]_{m,m} = \left(n + (m - N_{\rm PD} - 1) + \frac{1}{2}\right)$$
$$+ \frac{\tilde{\Delta}}{2}(-1)^{(\bar{n}+m-N_{\rm PD}-1)}, \quad \text{(B10)}$$

$$\left[H_{\rm PD}^{(-1)}(n)\right]_{m,m+1} = \sqrt{(n + m - N_{\rm PD} - 1) + 1} \times$$
$$\left(\frac{i\alpha}{\sqrt{2}\hbar\omega_c\ell_c}(1 - (-1)^{(\bar{n}+m-N_{\rm PD}-1)})\right.$$
$$\left. + \frac{\beta}{\sqrt{2}\hbar\omega_c\ell_c}(1 + (-1)^{(\bar{n}+m-N_{\rm PD}-1)})\right), \quad \text{(B11)}$$

and the eigenenergy $\varepsilon_{n,s}^{(-1)}$, is obtained as the $(N_{\rm PD}+1)$-th eigenvalue of $H_{\rm PD}^{(+1)}(n)$.

2. Matrix elements *without* parity symmetry

In the absence of parity symmetry, i.e. for $\theta \neq 0$, the matrix elements in Eqs. (6) and (7) are used to construct the partial matrix centered on the n-th state

$$\left[H_{\rm PD}(n)\right]_{m,m} = \left((n + m - N_{\rm PD} - 1) + \frac{1}{2}\right)\begin{bmatrix} 1 & 0 \\ 0 & 1 \end{bmatrix}$$
$$+ \begin{bmatrix} \frac{\tilde{\Delta}}{2} & \frac{\tilde{\Delta}}{2}\tan(\theta)e^{i\phi} \\ \frac{\tilde{\Delta}}{2}\tan(\theta)e^{-i\phi} & -\frac{\tilde{\Delta}}{2} \end{bmatrix} \text{(B12)}$$

$$\left[H_{\rm PD}(n)\right]_{m,m+1} = \sqrt{(n + m - N_{\rm PD} - 1) + 1} \times$$
$$\frac{1}{\sqrt{2}\hbar\omega_c\ell_c}\begin{bmatrix} 0 & 2\beta \\ -2i\alpha & 0 \end{bmatrix}, \quad \text{(B13)}$$

where $m \in [1, 2N_{\rm PD} + 1]$. The eigenenergy pair $\varepsilon_{n,+}$ and $\varepsilon_{n,+}$ are obtained as eigenvalues of $H_{\rm PD}(n)$ number $(2N_{\rm PD} + 1)$ and $(2N_{\rm PD} + 2)$.

C. Poisson's summation formula

Here we will apply the Poisson summation formula

$$\sum_{n=0}^{\infty} f(n) = \int_0^{\infty} dx f(x) + 2\sum_{l=1}^{\infty}\int_0^{\infty} dx f(x)\cos(l2\pi x), \quad \text{(C1)}$$

to the sum over the broadened Landau levels in Eq. (8). Starting with one spin species s

$$\sum_{n=0}^{\infty} L_\Gamma(E_F - \hbar\omega_c\varepsilon_{n,s}(B)) \quad \text{(C2)}$$
$$= \int_0^{\infty} dx L_\Gamma(E_F - \hbar\omega_c\varepsilon_{x,s}(B))$$
$$+ \sum_{l=1}^{\infty}\int_0^{\infty} dx L_\Gamma(E_F - \hbar\omega_c\varepsilon_{x,s}(B))\cos(l2\pi x). \text{(C3)}$$

Next, we introduce a change of variables

$$u = E_F - \hbar\omega_c\varepsilon_{x,s}(B), \quad \text{(C4)}$$
$$\frac{du}{dx} = -\hbar\omega_c\frac{\partial\varepsilon_{x,s}}{\partial x}. \quad \text{(C5)}$$

The derivative $\frac{\partial\varepsilon_{x,s}}{\partial x} = 1 + \mathcal{O}(\sqrt{\varepsilon_R/E_F})$ when evaluated at $\varepsilon_{x,s} \approx E_F/\hbar\omega_c$

$$\sum_{n=0}^{\infty} L_\Gamma(E_F - \hbar\omega_c\varepsilon_{n,s}(B)) \quad \text{(C6)}$$
$$= \frac{1}{\hbar\omega_c}\left(\int_{-\infty}^{\infty} du L_\Gamma(u)\right.$$
$$\left. + 2\sum_{l=1}^{\infty}\int_{-\infty}^{\infty} du L_\Gamma(u)\cos\left(l2\pi F_s(E_F - u, B)\right)\right)\text{(C7)}$$

In order to keep the equations as concise as possible, we will now drop the B argument in both F_s and $\varepsilon_{x,s}$. The integrand in Eq. (C7) has width $\sim \Gamma$, and since $E_F \gg \Gamma$, we can use 1st order Taylor expansion of the F_s function in terms of u

$$F_s(E_F - u) = F_s(E_F) - F'(E_F)u + \mathcal{O}(u^2) \quad \text{(C8)}$$
$$\approx F_s(E_F) - \frac{1}{\hbar\omega_c}u, \quad \text{(C9)}$$

where we have used $\frac{dF_s(E_F)}{dE_F} = \frac{1}{\hbar\omega_c}$, which is a consequence of $\frac{\partial\varepsilon_{n,s}}{\partial n} = 1$. This can be shown using that $n = F_s(E_F)$ is the inverse function of $E_F = \hbar\omega_c\varepsilon_{n,s}$, i.e. $n = F_s(\hbar\omega_c\varepsilon_{n,s})$. Taking the derivative of this relation with respect to n results in

$$1 = \frac{dF_s(E_F)}{dE_F}\hbar\omega_c\frac{\partial\varepsilon_{n,s}}{\partial n} \approx \frac{dF_s(E_F)}{dE_F}\hbar\omega_c, \quad \text{(C10)}$$

which yields the relation below Eq. (C9). We can thus write Eq. (C7) as

$$\sum_{n=0}^{\infty} L_\Gamma(E_F - \hbar\omega_c\varepsilon_{n,s}) \quad \text{(C11)}$$
$$= \frac{1}{\hbar\omega_c}\left(\int_{-\infty}^{\infty} du L_\Gamma(u)\right.$$
$$\left. + 2\sum_{l=1}^{\infty}\cos(l2\pi F_s(E_F))\int_{-\infty}^{\infty} du L_\Gamma(u)\cos\left(l2\pi\frac{u}{\hbar\omega_c}\right)\right)$$
$$= \frac{1}{\hbar\omega_c}\left(1 + 2\sum_{l=1}^{\infty}\cos(l2\pi F_s(E_F, B))\tilde{L}_\Gamma\left(l\frac{\Gamma}{\hbar\omega_c}\right)\right), \quad \text{(C12)}$$

where the symmetric broadening will makes the sine-term appearing in the Taylor expansion vanish. The cosine transform is defined as

$$\tilde{L}_\Gamma\left(l\frac{\Gamma}{\hbar\omega_c}\right) = \int_{-\infty}^{\infty} du L_\Gamma(u)\cos\left(l2\pi\frac{u}{\hbar\omega_c}\right), \quad \text{(C13)}$$

which, for Gaussian broadening, leads to

$$\tilde{L}_\Gamma \left(l \frac{\Gamma}{\hbar\omega_c} \right) = \exp\left(-\left[\sqrt{2}\pi\, l\, \frac{\Gamma}{\hbar\omega_c} \right]^2 \right) = e^{-l^2 \frac{B_q^2}{B^2}}, \quad \text{(C14)}$$

where we $B_q = \sqrt{2}\pi \frac{m^*\Gamma}{\hbar e}$. Finally, applying this to Eq. (8) and using the trigonometric relation

$$\cos(l2\pi F_+) + \cos(l2\pi F_+) \quad \text{(C15)}$$

$$= 2\cos\left(l2\pi \frac{F_+ + F_-}{2} \right) \cos\left(l2\pi \frac{F_+ - F_-}{2} \right) \text{(C16)}$$

and $\frac{1}{2\pi\ell_c^2} \frac{1}{\hbar\omega_c} = \frac{\hbar^2}{2\pi m^*}$ results in Eq. (10).

[1] L. Shubnikov and W. de Haas, 207a, b, c, 210a (1930).
[2] L. Shubnikov and W. de Haas, in *Proc. Netherlands Roy. Acad. Sci*, Vol. 33 (1930) p. 363.
[3] T. Ihn, *Semiconductor Nanostructures* (Oxford University Press, 2010).
[4] R. Winkler, *Spin-Orbit Coupling Effects in Two-Dimensional Electron and Hole Systems* (Springer Verlag, 2003).
[5] B. Das, D. Miller, S. Datta, R. Reifenberger, W. Hong, P. Bhattacharya, J. Singh, and M. Jaffe, Physical Review B **39**, 1411 (1989).
[6] Y. A. Bychkov and E. I. Rashba, Journal of physics C: Solid state physics **17**, 6039 (1984).
[7] B. Das, S. Datta, and R. Reifenberg, Phys. Rev. B **41**, 8278 (1990).
[8] B. Das, S. Datta, and R. Reifenberger, Physical Review B **41**, 8278 (1990).
[9] J. Nitta, H. Akazaki, H. Takayanagi, and T. Enoki, Phys. Rev. Lett. **78**, 1335 (1997).
[10] G. Engels, J. Lange, T. Schäpers, and H. Lüth, Physical Review B **55**, R1958 (1997).
[11] T. Schäpers, G. Engels, J. Lange, T. Klocke, M. Hollfelder, and H. Lüth, Journal of Applied Physics **83**, 4324 (1998), https://pubs.aip.org/aip/jap/article-pdf/83/8/4324/10592945/4324_1_online.pdf.
[12] G. Dresselhaus, Physical Review **100**, 580 (1955).
[13] A. Gilbertson, M. Fearn, J. Jefferson, B. Murdin, P. D. Buckle, and L. Cohen, Physical Review B **77**, 165335 (2008).
[14] M. Akabori, T. Sunouchi, T. Kakegawa, T. Sato, T.-k. Suzuki, and S. Yamada, Physica E: Low-dimensional Systems and Nanostructures **34**, 413 (2006).
[15] N. Averkiev, M. Glazov, and S. Tarasenko, Solid State Commun. **133**, 543 (2005).
[16] S. Tarasenko and N. Averkiev, JETP Lett. **75**, 552 (2002).
[17] S. Tarasenko, Physics of Solid State **44**, 1769 (2002).
[18] W. Yang and K. Chang, Phys. Rev. B **73**, 045303 (2006).
[19] A. J. A. Beukman, F. K. de Vries, J. van Veen, R. Skolasinski, M. Wimmer, F. Qu, D. T. de Vries, B.-M. Nguyen, W. Yi, A. A. Kiselev, M. Sokolich, M. J. Manfra, F. Nichele, C. M. Marcus, and L. P. Kouwenhoven, Phys. Rev. B **96**, 241401 (2017).
[20] V. I. Fal'ko, Physical Review B **46**, 4320 (1992).
[21] F. Herzog, H. Hardtdegen, T. Schäpers, D. Grundler, and M. Wilde, New Journal of Physics **19**, 103012 (2017).
[22] M. A. Wilde and D. Grundler, New Journal of Physics **15**, 115013 (2013).
[23] G. Golub and C. F. van Loan, *Matrix Computations*, 4th ed. (The Johns Hopkins University Press, 2013).
[24] Here we benchmark using a powerful laptop.
[25] J. Casanova, G. Romero, I. Lizuain, J. J. García-Ripoll, and E. Solano, Physical Review Letters **105**, 263603 (2010).
[26] D. Braak, Phys. Rev. Lett. **107**, 100401 (2011).
[27] D. R. Candido, S. I. Erlingsson, H. Gramizadeh, J. V. I. Costa, P. J. Weigele, D. M. Zumbühl, and J. C. Egues, "Quantum oscillations in 2d electron gases with spin-orbit and zeeman interactions," (2023), arXiv:2304.14327 [cond-mat.mes-hall].
[28] M. Brack and R. Bhaduri, *Semiclassical physics* (Addison-Wesley Publishing, 1997).
[29] F. F. Fang and P. J. Stiles, Phys. Rev. **174**, 823 (1968).
[30] S. Brosig, K. Ensslin, A. G. Jansen, C. Nguyen, B. Brar, M. Thomas, and H. Kroemer, Phys. Rev. B **61**, 13045 (2000).
[31] A. T. Hatke, M. A. Zudov, L. N. Pfeiffer, and K. W. West, Phys. Rev. B **85**, 241305 (2012).

Chapter 4

Appendix

4.1 Parity and Hamiltonian elements for pure Rashba and Dresselhaus

$$[H_R, N^+] = [a^\dagger \sigma_- + a\sigma_+, a^\dagger a + \frac{\sigma_z}{2}]$$

$$= [a^\dagger \sigma_-, a^\dagger a] + [a^\dagger \sigma_-, \frac{\sigma_z}{2}] + [a\sigma_+, a^\dagger a] + [a\sigma_+, \frac{\sigma_z}{2}]$$

$$[H_R, N^+] = a^\dagger[\sigma_-, a^\dagger]a + (a^\dagger)^2[\sigma_-, a] + a^\dagger[a^\dagger, a]\sigma_- + a^\dagger[\sigma_-, \frac{\sigma_z}{2}] + [a^\dagger, \frac{\sigma_z}{2}]\sigma_- + a[\sigma_+, a^\dagger]a +$$

$$+ [a, a^\dagger]\sigma_+ a + a^\dagger a[\sigma_+, a] + a[\sigma_+, \frac{\sigma_z}{2}] + [a, \frac{\sigma_z}{2}]\sigma_+$$

$$= 0$$

$$(4.1)$$

In our calculations, the parity operator and the Rashba and Dresselhaus Hamiltonian terms commute, which is a valid assumption in systems with a well-defined parity symmetry.

$$
\begin{aligned}
[P, \hat{\gamma} a^\dagger \sigma_\pm] &= (P\hat{\gamma} a^\dagger \sigma_\pm - \hat{\gamma} a^\dagger \sigma_\pm P) \\
&= P(\hat{\gamma} a^\dagger \sigma_\pm - P^{-1}\hat{\gamma} a^\dagger \sigma_\pm P) \\
&= P(\hat{\gamma} a^\dagger \sigma_\pm - P^{-1}\hat{\gamma} a^\dagger P P^{-1} \sigma_\pm P) \\
&= P(\hat{\gamma} a^\dagger \sigma_\pm - \hat{\gamma} P^{-1} a^\dagger P P^{-1} \sigma_\pm P)
\end{aligned}
$$

where we used that $[P, \hat{\gamma}] = 0$. The similarity transforms are

$$
\begin{aligned}
P^{-1}a^{\dagger}P &= e^{i\pi a^{\dagger}a}a^{\dagger}e^{i\pi a^{\dagger}a} \\
&= a^{\dagger} + \frac{(i\pi)}{1!}[a^{\dagger}a, a^{\dagger}] + \frac{(i\pi)^2}{2!}[a^{\dagger}a, [a^{\dagger}a, a^{\dagger}]] + ... \\
&= a^{\dagger}\left(1 + \frac{i\pi}{1!}\pi + \frac{(i\pi)^2}{2!} + ...\right) \\
&= a^{\dagger}e^{i\pi} = a^{\dagger}\cos(\pi) = a^{\dagger}(-1) \\
P^{-1}\sigma_{\pm}P &= e^{+i\frac{\pi}{2}\sigma_z}\sigma_{\pm}e^{+i\frac{\pi}{2}\sigma_z} \\
&= \sigma_{\pm} + \frac{(i\pi)}{2 1!}[\sigma_z, \sigma_{\pm}] + \frac{(i\pi)^2}{2^2 2!}[\sigma_z, [\sigma_z, \sigma_{\pm}]] + ... \\
&= \sigma_{\pm} + \frac{(i\pi)}{2 1!}(\pm 2\sigma_{\pm}) + \frac{(i\pi)^2}{2^2 2!}(\pm 2)^2\sigma_{\pm} + ... \\
&= \sigma_{\pm}\left(1 + \frac{(\pm i\pi)}{1!} + \frac{(\pm i\pi)^2}{2!} + ...\right) \\
&= \sigma_{\pm}e^{\pm i\pi} = \sigma_{\pm}\cos(\pm\pi) = (-1)\sigma_{\pm}
\end{aligned}
$$

$$
\begin{aligned}
[P, \hat{\gamma}a^{\dagger}\sigma_{\pm}] &= P(\hat{\gamma}a^{\dagger}\sigma_{\pm} - \hat{\gamma}P^{-1}a^{\dagger}PP^{-1}\sigma_{\pm}P) \\
&= P(\hat{\gamma}a^{\dagger}\sigma_{\pm} - \hat{\gamma}(-1)a^{\dagger}P(-1)\sigma_{\pm}) \\
&= P(\hat{\gamma}a^{\dagger}\sigma_{\pm} - (-1)^2\hat{\gamma}a^{\dagger}\sigma_{\pm}) = 0
\end{aligned}
\tag{4.2}
$$

4.2 Eigenstates by different Landau levels

an eigenstate is a state of a quantum system that is an eigenvector of a particular operator here the Hamiltonian well-known operator which gives the energy of the system. The corresponding eigenvalue is the energy of the system in that state. Eigenstates are important because they represent the possible states of a system that can be observed or measured. For example, in a system with two modes (such as the vibrations of a molecule), each mode can be described by its own set of eigenstates. These eigenstates are orthogonal to each other, meaning that they are independent of one another. This is important because it means that the state of one mode does not affect the state of the other mode. The eigenstates of a system can also be used to describe the probability of finding the system in a particular state. For example, if a system is in an eigenstate with a high probability, it is more likely to be found in that state when measured.

Overall, eigenstates play a key role in understanding and predicting the behavior of quantum systems. Since the eigenvalues are obtained analytically in pure Rashba

case,in order to better see exactly what is happening between the states specially the crossing points, one needs to have a relationship between the different eigenstates, which is the closest states and points for two different.$|\psi_\pm\rangle$.

$$\begin{pmatrix} \frac{1}{2}(1-\widetilde{\Delta}) & 2a_R\sqrt{n} \\ 2a_R\sqrt{n} & -\frac{1}{2}(1-\widetilde{\Delta}) \end{pmatrix}\begin{pmatrix} A \\ B \end{pmatrix} =$$

$$= \sqrt{\frac{1}{2}(1-\widetilde{\Delta})^2 + (2a_R\sqrt{n})^2}\begin{pmatrix} A \\ B \end{pmatrix}$$

$$\begin{pmatrix} \frac{1}{2}(1-\widetilde{\Delta}) & 2a_R\sqrt{n} \\ 2a_R\sqrt{n} & -\frac{1}{2}(1-\widetilde{\Delta}) \end{pmatrix} = \sqrt{\frac{1}{4}(1-\widetilde{\Delta})^2 + (2a_R\sqrt{n})^2}\begin{pmatrix} \cos(\theta_n) & \sin(\theta_n) \\ \sin(\theta_n) & -\cos(\theta_n) \end{pmatrix}$$

so we can define these $\cos(\theta_n)$ and $\sin(\theta_n)$:

$$\cos(\theta_n) = \frac{\frac{1}{2}(1-\widetilde{\Delta})}{\sqrt{\frac{1}{2}(1-\widetilde{\Delta})^2 + (2a_R\sqrt{n})^2}} \tag{4.3}$$

$$\sin(\theta_n) = \frac{2a_R\sqrt{n}}{\sqrt{\frac{1}{2}(1-\widetilde{\Delta})^2 + (2a_R\sqrt{n})^2}} \tag{4.4}$$

so we have $\theta_n = \cos^{-1}(\frac{\frac{1}{2}(1-\widetilde{\Delta})}{\sqrt{\frac{1}{2}(1-\widetilde{\Delta})^2+(2a_R\sqrt{n})^2}})$ in one hand which present as auto normalization of states.

 now we are going to obtain the eigenstates for general case eigenvalue is equal to +1 and -1:

$$\begin{pmatrix} \cos(\theta_n) & \sin(\theta_n) \\ \sin(\theta_n) & -\cos(\theta_n) \end{pmatrix}\begin{pmatrix} A \\ B \end{pmatrix} = +1\begin{pmatrix} A \\ B \end{pmatrix}$$

now we have the tools for obtaining the A and B and the defenition of eigenstates with knowing these basics.

$$|A|^2 + |B|^2 = 1$$
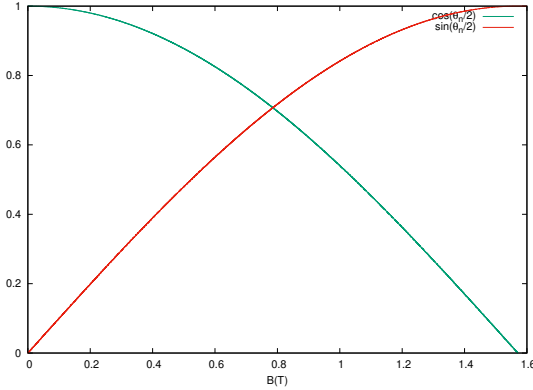$$A\cos(\theta_n) + B\sin(\theta_n) = A$$

Figure 4.1: the cosine and sine parts which describe the situation of the states and projecting on the basis states

so the A and B will satisfy both relations with $\cos(\theta)$ and $\sin(\theta)$ in eigenvalue equal +1:

$$A = \cos(\theta)$$
$$B = \sin(\theta)$$
$$\cos(\theta)\cos(\theta_n) + \sin(\theta)\sin(\theta_n) = \cos(\theta)$$
$$\cos(\theta - \theta_n) = \cos(\theta)$$
$$\theta = \frac{\theta_n}{2}$$

Therefore for eigenvalue equal 1 the eigenvector is:

$$\begin{pmatrix} \cos(\frac{\theta_n}{2}) \\ \sin(\frac{\theta_n}{2}) \end{pmatrix} \Rightarrow \cos(\frac{\theta_n}{2})|n, \downarrow\rangle + \sin(\frac{\theta_n}{2})|n - 1, \uparrow\rangle \tag{4.5}$$

for eigenvalue equal -1 as well it could be written as :

$$\begin{pmatrix} -\sin(\frac{\theta_n}{2}) \\ \cos(\frac{\theta_n}{2}) \end{pmatrix} \Rightarrow -\sin(\frac{\theta_n}{2})|n, \downarrow\rangle + \cos(\frac{\theta_n}{2})|n - 1, \uparrow\rangle \tag{4.6}$$

By this means now we can apply the Hamiltonian operator on these states and we are able to explain in what points they have the same amount with crossing point which

is taken by definition of the cos and sin in eigenstates.

$$H_R(\cos(\frac{\theta_n}{2})|n,\downarrow\rangle + \sin(\frac{\theta_n}{2})|n-1,\uparrow\rangle) = \varepsilon_+((\cos(\frac{\theta_n}{2})|n,\downarrow\rangle + \sin(\frac{\theta_n}{2})|n-1,\uparrow\rangle)$$

$$H_R(-\sin(\frac{\theta_{m+1}}{2})|m+1,\downarrow\rangle + \cos(\frac{\theta_{m+1}}{2})|m,\uparrow\rangle) = \varepsilon_-(-\sin(\frac{\theta_{m+1}}{2})|m+1,\downarrow\rangle + \cos(\frac{\theta_{m+1}}{2})|m,\uparrow\rangle)$$

and matrix elements comes as :

$$\langle\psi_{n\downarrow}|H_R|\psi_{m\uparrow}\rangle = 0$$
$$\langle\psi_{n\downarrow}|H_R|\psi_{m\downarrow}\rangle = \varepsilon_{n\downarrow}$$
$$\langle\psi_{m\uparrow}|H_R|\psi_{m\uparrow}\rangle = \varepsilon_{m\uparrow}$$
$$\langle\psi_{n\downarrow}|H_R|\psi_{m\uparrow}\rangle = 0$$

4.2.1   Magnetic points at the intersecting energy spectrum

In this study, we considered two states that cross each other in the absence of an in-plane magnetic field. However, when an in-plane magnetic field was applied, a gap opened up between the two states, indicating that they are coupled. To understand the nature of this coupling and the points of connection between the two states, we labeled the states differently and rewrote one state in terms of the difference between the other state and the magnetic field.[48] This allowed us to gain insight into the behavior of the system and the role of the magnetic field in mediating the coupling between the two states. Overall, our analysis provides a deeper understanding of the coupling between these two states and the effects of an in-plane magnetic field on their behavior.

$$\begin{cases} m = n + \Delta n \\ \delta = \varepsilon_{m,\uparrow} - \varepsilon_{n,\downarrow} \end{cases}$$

$$\tag{4.7}$$

In order to find the points of connection of the two energy spectra and in which magnetic field two different energy spectra intersect, we can take the energy of these two equations to obtain the magnitude of the magnetic field in terms of other parameters such as differential state numbers. And we can have a quantum number like that.

After obtaining the wave function of this system in two basis.[25], [32], [33]

$$\delta = \varepsilon_{n+\Delta n,\uparrow} - \varepsilon_{n,\downarrow}$$

$$n + \Delta n + 1 - \sqrt{\frac{1}{4}(1 - \widetilde{\Delta})^2 + 4a_R^2(n + \Delta n + 1)} - n - \sqrt{\frac{1}{4}(1 - \widetilde{\Delta})^2 + 4a_R^2 n} = 0$$

$$(4.8)$$

The $\widetilde{\Delta} = \frac{mgB_z}{\hbar\omega_c}$ if we take the limilts $B \to \infty$ the energy of the system would be the same as simple word kill the spin-orbit interaction and as a fixed magnetic field for Zeeman case $a_R \to 0$ also we take that $|B_z|$ T and we have a dependent of magnetic field for ω_c that make us able to find all the crossing points in the spectrum of Energies for each Landau levels. as we defined all the magnetic fields are B_z in Rashba constant and in Zeeman term and we are here trying to show in what magnetic field we have crossing points. for doing the algebraic part it would be helpful to do the Taylor expansion as we consider n and $n + \Delta n + 1$ a standard trick for simplifying as it comes in below:

$$n = n + \left(\frac{1 + \Delta n}{2}\right) - \left(\frac{1 + \Delta n}{2}\right) \tag{4.9}$$

$$n + 1 + \Delta n = n + \left(\frac{1 + \Delta n}{2}\right) + \left(\frac{1 + \Delta n}{2}\right) \tag{4.10}$$

now we have considered the difference between these two energies values:

$$n + (1 + \Delta n)/2 + (1 + \Delta n)/2 - \sqrt{\frac{1}{4}(1 - \widetilde{\Delta})^2 + 4a_R^2(n + (1 + \Delta n)/2 + (1 + \Delta n)/2)}$$

$$-n + (1+\Delta n)/2 - (1+\Delta n)/2 - \sqrt{\frac{1}{4}(1 - \widetilde{\Delta})^2 + 4a_R^2(n + (1 + \Delta n)/2 - (1 + \Delta n)/2)} = 0$$

$$(4.11)$$

and using Taylor expansion around this new version of n and $n + (\Delta n + 1)/2$:

$$f(x) = f(a) + f'(a)(x - a) + \frac{f''(a)}{2!}(x - a)^2 + \frac{f'''(a)}{3!}(x - a)^3 + \dots \tag{4.12}$$

using the general definition of the Taylor approximation, we have the difference of these two energies as a contribution of the opposite signs that cause to kill the linear

terms and second, third and other terms are negligible comparing the others.

$$f(x+a)+f(x-a) = (f(-a)+f(a))+x(f'(-a)+f'(a))+1/2x^2(f''(-a)+f''(a))+$$
$$1/6x^3(f'''(-a) + f'''(a)) + O(x^4) \quad (4.13)$$

here in this equation we have the $x=n + (\frac{\Delta n+1}{2})$ and $a=(\frac{\Delta n+1}{2})$. by this substitution and contribution of opposite signs of the linear terms kill each other and the second terms and the further dependence of the x killing each other and just $f(a)+f'(-a)$ survive from the algebra and we have a simple equation contains a_R which has included the B_z the only dependency of magnetic field.

$$(1 - \widetilde{\Delta}) + (\frac{4a_R^2(n + (\frac{\Delta n+1}{2}))}{1 - \widetilde{\Delta}}) = 0 \quad (4.14)$$

the only term of B is B_z in the term of the $\hbar\omega_c\ell_c$ which is :

$$\hbar\omega_c\ell_c = \frac{3}{m}\sqrt{B_z} \quad (4.15)$$

that leads us to this final magnetic field of B_z:

$$B_z = \frac{0.22m^2\alpha^2(n + \frac{(1+\Delta n)}{2})}{(\Delta - 1)^2} \quad (4.16)$$

we know that Δn compared to n is small because it has indicated the number of differences of the states like first or 2nd or ... above or underneath states. where m and g for example InAs fix parameters are g=-12 and m=0.04. and in all the figures there is fixed B_z for showing the Zeeman effect. also all the crossing points has this $\delta = 0$ in case of the in-plane magnetic field.

4.3 Density of States

The description of the density of states in a magnetic field is suitable for further calculations at low magnetic fields, where many landau levels are occupied ($E_F \gg \hbar\omega_c$).

$$D_{2D}(E, B) = \sum_{x=0}^{\infty} L(E_F - \varepsilon_{\bar{x}s}(B))$$

$$\sum_{n=0}^{\infty} L(E_F - \varepsilon_{\bar{x}s}(B)) = \int_{-\frac{1}{2}}^{+\infty} L(E_f - \varepsilon_{xs}(B))d\bar{x}+$$

$$2\sum_{s=1}^{+\infty} \int_{-\frac{1}{2}}^{+\infty} L(E_F - \varepsilon_{\bar{x}s}(B))\cos(2\pi(\bar{x})s)dx$$

$$\int_{-\frac{1}{2}}^{+\infty} L(E_F - \varepsilon_{\bar{x}s}(B))d\bar{x} + 2\sum_{s=1}^{+\infty} \int_{-\frac{1}{2}}^{+\infty} L(E_F - \varepsilon_{\bar{x}s}(B))\cos(2\pi(\bar{x})s)dx$$

$$g(\bar{x}) = L(E_F - \varepsilon_{\bar{x}s}(B))$$

$$D_{2D}(E,B) = \int_{\frac{1}{2}}^{\infty} g(\bar{x})d\bar{x} + 2\sum_{s=1}^{\infty} \int_{\frac{1}{2}}^{\infty} g(\bar{x})\cos(2\pi s\bar{x})d\bar{x}$$

where we used the relations at the same time.

actually we have to part first is the simple integral and the other is the integral with crossing a cos part for that we are trying to get result in seperate way for both parts

$$u = -E_F + \varepsilon_{x\downarrow(B)}$$
$$du = (\frac{\partial \varepsilon_{xs}}{\partial x})dx \simeq dx$$

because of the number of occupied Landua levels as you can see in equation (**??**) we have $= \frac{\partial \varepsilon_{xs}}{\partial x} \simeq 1 \pm \dfrac{(\frac{\alpha}{\hbar\omega_c l_c})^2}{2\sqrt{(\frac{\alpha}{\hbar\omega_c l_c})^2 n}}$ which is very small and with good approximation is 1

$$u + E_F = \varepsilon_{x\downarrow}(B)$$
$$F_{\downarrow}(E_F + u) = x$$
$$\frac{\partial \varepsilon_{xs}}{\partial x} \simeq 1$$

which it comes from first order Taylor's expansion of F function:

$$F_\downarrow(E_F + u) = F_\downarrow(E_F) + \frac{\partial F_\downarrow}{\partial E_F}u \tag{4.17}$$

$$F_\uparrow(E_F + u) = F_\uparrow(E_F) + \frac{\partial F_\uparrow}{\partial E_F}u \tag{4.18}$$

we have this conceded part that E_F is a very big number in order the landau level occupied by electrons in the nth level and it is $E_F \gg \frac{\hbar}{\tau_q}$

$$\sum_{\bar{x}=0}^{\infty} L(E_F - \varepsilon_{\bar{x}s}(B)) = \int_{-\infty}^{+\infty} L(E_F - \varepsilon_{\bar{x}s}(B))d\bar{x} +$$

$$2\sum_{s=1}^{+\infty} \int_{-\infty}^{+\infty} L(E_F - \varepsilon_{\bar{x}s}(B))\cos(2\pi(\bar{x})s)dx +$$

$$\int_{-\infty}^{+\infty} L(E_F - \varepsilon_{\bar{x}s}(B))d\bar{x} +$$

$$2\sum_{s=1}^{+\infty} \int_{-\infty}^{+\infty} L(E_F - \varepsilon_{\bar{x}s}(B))\cos(2\pi(\bar{x})s)dx$$

in this case the term of the $\frac{\Delta D}{D}$ or finding the cosine part is the key of finding the total Density of States so we can rewrite one part as well as the other one which is the same almost and then conducive to the Oscillations.

$$\int_{-\frac{1}{2}}^{+\infty} L(E_F - \varepsilon_{x\downarrow}(B))dx$$

$$= \int_{\infty}^{\infty} duL(u) = 1 \int_{-E_F+\varepsilon_{x\downarrow}}^{+\infty} L(u)\frac{1}{\frac{\partial \varepsilon_{x\downarrow}}{\partial x}}du \approx \int_{-E_F+\varepsilon_{x\downarrow}}^{+\infty} L(u)du$$

$$\frac{\Delta D}{D} = \int_{-\infty}^{+\infty} L(u)\cos(2\pi s(F_\uparrow(E_F), B) + u))du +$$

$$\int_{-\infty}^{+\infty} L(u)\cos(2\pi s(F_\downarrow(E_F, B) + u))du$$

$$D_{2D}(E,B) = \int_{-\infty}^{+\infty} L(u)du +$$

$$2\sum_{s=1}^{+\infty} \int_{-\infty}^{+\infty} L(u)\cos(2\pi s(F_\uparrow(E_F),B)+u))du + \int_{-\infty}^{+\infty} L(u)du$$

$$+ 2\sum_{s=1}^{+\infty} \int_{-\infty}^{+\infty} L(u)\cos(2\pi s(F_\downarrow(E_F),B)+u))du$$

It is therefore justified to consider only the first term with $s = 1$ and harmonic variation of the density of states at constant energy, for small magnetic fields where $1 \gg \omega_c\tau$. At the Fermi energy, the density of states varies periodically as $\frac{1}{B}$.

$$\frac{\Delta D}{D} = \cos(2\pi s F_\downarrow) \int_{-\infty}^{+\infty} L(u)\cos(2\pi s u)du + \qquad (4.19)$$

$$\cos(2\pi s F_\uparrow) \int_{-\infty}^{+\infty} L(u)\cos(2\pi s u)du \qquad (4.20)$$

$$D_{2D}(E,B) = 2D_0 + 2D_0\widetilde{L}(u)((\cos(2\pi s F_\uparrow) + \cos(2\pi s F_\downarrow))$$

$$D_{2D}(E,B) = 2D_0 + 4D_0\widetilde{L}(u)\cos(2\pi s(\frac{F_\uparrow + F_\downarrow}{2}))\cos(2\pi s(\frac{F_\uparrow - F_\downarrow}{2})) \qquad (4.21)$$

References

[1] L. Bockhorn, P. Barthold, D. Schuh, W. Wegscheider, and R. J. Haug, "Magne-toresistance in a high-mobility two-dimensional electron gas," *Physical Review B*, vol. 83, no. 11, p. 113 301, 2011.

[2] Y. Wang, G. Qiu, R. Wang, *et al.*, "Field-effect transistors made from solution-grown two-dimensional tellurene," *Nature Electronics*, vol. 1, no. 4, pp. 228–236, 2018.

[3] G. Engels, J. Lange, T. Schäpers, and H. Lüth, "Experimental and theoretical approach to spin splitting in modulation-doped in x ga 1- x as/inp quantum wells for b 0," *Physical Review B*, vol. 55, no. 4, R1958, 1997.

[4] X. Wang and P. Vasilopoulos, "Band structure and magnetotransport of a two-dimensional electron gas in the presence of spin-orbit interaction," *Physical Review B*, vol. 72, no. 8, p. 085 344, 2005.

[5] S. Tarasenko and N. Averkina, "Interference of spin splitting in magneto-oscillation phenomena in two-dimensional systems," *Pis' ma v Zhurnal Ehksperimental'noj i Teoreticheskoj Fiziki*, vol. 75, no. 11-12, pp. 669–672, 2002.

[6] A. Rowe, J. Nehls, R. Stradling, and R. Ferguson, "Origin of beat patterns in the quantum magnetoresistance of gated inas/gasb and inas/alsb quantum wells," *Physical Review B*, vol. 63, no. 20, p. 201 307, 2001.

[7] T. Ihn, *Semiconductor Nanostructures: Quantum states and electronic transport*. Oxford University Press, 2010.

[8] M. A. Eriksson, M. Friesen, S. N. Coppersmith, *et al.*, "Spin-based quantum dot quantum computing in silicon," *Quantum Information Processing*, vol. 3, pp. 133–146, 2004.

[9] S. Goswami, K. Slinker, M. Friesen, *et al.*, "Controllable valley splitting in sili-con quantum devices," *Nature Physics*, vol. 3, no. 1, pp. 41–45, 2007.

[10] J. Shi, J. Zhang, L. Yang, M. Qu, D.-C. Qi, and K. H. Zhang, "Wide bandgap oxide semiconductors: From materials physics to optoelectronic devices," *Advanced Materials*, vol. 33, no. 50, p. 2 006 230, 2021.

78

[11] S. D. Sarma, S. Adam, E. Hwang, and E. Rossi, "Electronic transport in two-dimensional graphene," *Reviews of modern physics*, vol. 83, no. 2, p. 407, 2011.

[12] S. E. Hernández, M. Akabori, K. Sladek, *et al.*, "Spin-orbit coupling and phase coherence in inas nanowires," *Physical Review B*, vol. 82, no. 23, p. 235 303, 2010.

[13] M. Kepenekian and J. Even, "Rashba and dresselhaus couplings in halide perovskites: Accomplishments and opportunities for spintronics and spin–orbitronics," *The Journal of Physical Chemistry Letters*, vol. 8, no. 14, pp. 3362–3370, 2017.

[14] A. Fert, "Nobel lecture: Origin, development, and future of spintronics," *Reviews of modern physics*, vol. 80, no. 4, p. 1517, 2008.

[15] D. Waldeck, R. Naaman, and Y. Paltiel, "The spin selectivity effect in chiral materials," *APL materials*, vol. 9, no. 4, p. 040 902, 2021.

[16] P. Zeeman and M. Bôcher, "Zeeman effect," *Nature*, vol. 55, no. 347, p. 3, 1897.

[17] M. Yang, R. Wagner, B. Shanabrook, J. Waterman, and W. Moore, "Spin-resolved cyclotron resonance in inas quantum wells: A study of the energy-dependent g factor," *Physical Review B*, vol. 47, no. 11, p. 6807, 1993.

[18] Y. A. Nefyodov, A. Shchepetilnikov, I. Kukushkin, W. Dietsche, and S. Schmult, "G-factor anisotropy in a gaas/al x ga 1- x as quantum well probed by electron spin resonance," *Physical Review B*, vol. 83, no. 4, p. 041 307, 2011.

[19] E. I. Rashba, "Spin-orbit coupling in condensed matter physics," *Sov Phys Solid State*, vol. 2, p. 1109, 1960.

[20] S. Tölle, M. Dzierzawa, U. Eckern, and C. Gorini, "Spin hall magnetoresistance and spin nernst magnetothermopower: Role of the inverse spin galvanic effect," *arXiv preprint arXiv:1708.03165*, 2017.

[21] Y. A. Bychkov and É. I. Rashba, "Properties of a 2d electron gas with lifted spectral degeneracy," *JETP lett*, vol. 39, no. 2, p. 78, 1984.

[22] C. Bell, M. Bahramy, H. Murakawa, *et al.*, "Shubnikov–de haas oscillations in the bulk rashba semiconductor bitei," *Physical Review B*, vol. 87, no. 8, p. 081 109, 2013.

[23] D. Marchenko, A. Varykhalov, M. Scholz, *et al.*, "Giant rashba splitting in graphene due to hybridization with gold," *Nature communications*, vol. 3, no. 1, p. 1232, 2012.

[24] B. Thaller, *Advanced visual quantum mechanics*. Springer Science & Business Media, 2005.

[25] S. I. Erlingsson, J. C. Egues, and D. Loss, "Energy spectra for quantum wires and two-dimensional electron gases in magnetic fields with rashba and dresselhaus spin-orbit interactions," *Physical Review B*, vol. 82, no. 15, p. 155 456, 2010.

[26] J. A. Maytorena, C. López-Bastidas, and F. Mireles, "Spin and charge optical conductivities in spin-orbit coupled systems," *Physical Review B*, vol. 74, no. 23, p. 235 313, 2006.

[27] M. Yama, M. Tatsuno, T. Kato, and M. Matsuo, "Spin pumping of two-dimensional electron gas with rashba and dresselhaus spin-orbit interactions," *Physical Review B*, vol. 104, no. 5, p. 054 410, 2021.

[28] M. Trushin, K. Výborný, P. Moraczewski, A. A. Kovalev, J. Schliemann, and T. Jungwirth, "Anisotropic magnetoresistance of spin-orbit coupled carriers scattered from polarized magnetic impurities," *Physical Review B*, vol. 80, no. 13, p. 134 405, 2009.

[29] S. Bandyopadhyay and M. Cahay, "Electron spin for classical information processing: A brief survey of spin-based logic devices, gates and circuits," *Nanotechnology*, vol. 20, no. 41, p. 412 001, 2009.

[30] S. Prabhakar, J. E. Raynolds, and R. Melnik, "Manipulation of the landé g factor in inas quantum dots through the application of anisotropic gate potentials: Exact diagonalization, numerical, and perturbation methods," *Physical Review B*, vol. 84, no. 15, p. 155 208, 2011.

[31] S. Debald and B. Kramer, "Rashba effect and magnetic field in semiconductor quantum wires," *Physical Review B*, vol. 71, no. 11, p. 115 322, 2005.

[32] V. I. Fal'ko, "Cyclotron and electric-dipole spin resonances in a two-dimensional electron gas in the vicinity of the crossing of spin-split landau levels," *Physical Review B*, vol. 46, no. 7, p. 4320, 1992.

[33] A. J. Beukman, F. K. De Vries, J. Van Veen, *et al.*, "Spin-orbit interaction in a dual gated inas/gasb quantum well," *Physical Review B*, vol. 96, no. 24, p. 241 401, 2017.

[34] R. Winkler, S. Papadakis, E. De Poortere, and M. Shayegan, *Spin-Orbit Coupling in Two-Dimensional Electron and Hole Systems*. Springer, 2003, vol. 41.

[35] M. A. Wilde and D. Grundler, "Alternative method for the quantitative determination of rashba-and dresselhaus spin-orbit interaction using the magnetization," *New Journal of Physics*, vol. 15, no. 11, p. 115 013, 2013.

[36] W. Zhu, H. Yuan, Q. Shi, J. Hou, and X. Wang, "Shape of the landau subbands in disordered graphene," *Physical Review B*, vol. 83, no. 15, p. 153 408, 2011.

[37] S. Brosig, K. Ensslin, A. Jansen, *et al.*, "Inas-alsb quantum wells in tilted magnetic fields," *Physical Review B*, vol. 61, no. 19, p. 13 045, 2000.

[38] S. K. Maiti, M. Dey, S. Sil, A. Chakrabarti, and S. Karmakar, "Magneto-transport in a mesoscopic ring with rashba and dresselhaus spin-orbit interactions," *Europhysics Letters*, vol. 95, no. 5, p. 57 008, 2011.

[39] P. Kleinert and V. Bryksin, "Current-induced spin accumulation in lateral superlattices with rashba and dresselhaus spin–orbit interaction," *Superlattices and Microstructures*, vol. 39, no. 5, pp. 421–428, 2006.

[40] P. Krstajić, M. Pagano, and P. Vasilopoulos, "Transport properties of low-dimensional semiconductor structures in the presence of spin–orbit interaction," *Physica E: Low-dimensional Systems and Nanostructures*, vol. 43, no. 4, pp. 893–900, 2011.

[41] J. W. Cooley and J. W. Tukey, "An algorithm for the machine calculation of complex fourier series," *Mathematics of computation*, vol. 19, no. 90, pp. 297–301, 1965.

[42] T. Schäpers, G. Engels, J. Lange, T. Klocke, M. Hollfelder, and H. Lüth, "Effect of the heterointerface on the spin splitting in modulation doped in x ga 1- x as/inp quantum wells for b 0," *Journal of Applied Physics*, vol. 83, no. 8, pp. 4324–4333, 1998.

[43] Z. Zhu, Q.-f. Sun, B. Chen, and X. Xie, "Numerical simulations of a ballistic spin interferometer with rashba spin-orbital interaction," *Physical Review B*, vol. 74, no. 8, p. 085 327, 2006.

[44] Y. Fang, F. Tang, Y. Ruan, *et al.*, "Magnetic-field-induced nontrivial electronic state in the kondo-lattice semimetal cesb," *Physical Review B*, vol. 101, no. 9, p. 094 424, 2020.

[45] F. Al-Badour, M. Sunar, and L. Cheded, "Vibration analysis of rotating machinery using time–frequency analysis and wavelet techniques," *Mechanical Systems and Signal Processing*, vol. 25, no. 6, pp. 2083–2101, 2011.

[46] M. Haidar, A. A. Awad, M. Dvornik, R. Khymyn, A. Houshang, and J. Åkerman, "A single layer spin-orbit torque nano-oscillator," *Nature communications*, vol. 10, no. 1, p. 2362, 2019.

[47] C. Perroni, D. Bercioux, V. M. Ramaglia, and V. Cataudella, "Rashba quantum wire: Exact solution and ballistic transport," *Journal of Physics: Condensed Matter*, vol. 19, no. 18, p. 186 227, 2007.

[48] Y. Y. Tkach, "Determination of the rashba and dresselhaus spin–orbit interaction parameters and g-factor from the critical points of the spectrum in a 2d electron gas in an in-plane magnetic field," *physica status solidi (b)*, vol. 258, no. 5, p. 2 000 553, 2021.

[49] L. Du, I. Knez, G. Sullivan, and R.-R. Du, "Robust helical edge transport in gated inas/gasb bilayers," *Physical review letters*, vol. 114, no. 9, p. 096 802, 2015.

[50] B. Ashkinadze, E. Cohen, V. Rudenkov, P. Christianen, J. Maan, and L. Pfeiffer, "Transition from two-dimensional electron-hole to geminate-exciton photoluminescence in ga as/ al x ga 1- x as heterostructures under a high in-plane magnetic field," *Physical Review B*, vol. 76, no. 7, p. 075 344, 2007.